

The Paton WELDING JOURNAL

July
2009
7

English translation of the monthly «Avtomaticheskaya Svarka» (Automatic Welding) journal published in Russian since 1948

Founders: E.O. Paton Electric Welding Institute of the NAS of Ukraine
International Association «Welding»

Publisher: International Association «Welding»

Editor-in-Chief B.E.Paton

Editorial board:

Yu.S.Borisov	V.F.Khorunov
A.Ya.Ishchenko	I.V.Krivtsun
B.V.Khitrovskaya	L.M.Lobanov
V.I.Kirlian	A.A.Mazur
S.I.Kuchuk	Yatsenko
Yu.N.Lankin	I.K.Pokhodnya
V.N.Lipodaev	V.D.Poznyakov
V.I.Makhnenko	K.A.Yushchenko
O.K.Nazarenko	A.T.Zelnichenko
I.A.Ryabtsev	

International editorial council:

N.P.Alyoshin	(Russia)
U.Diltey	(Germany)
Guan Qiao	(China)
D. von Hofe	(Germany)
V.I.Lysak	(Russia)
N.I.Nikiforov	(Russia)
B.E.Paton	(Ukraine)
Ya.Pilarczyk	(Poland)
P.Seyffarth	(Germany)
G.A.Turichin	(Russia)
Zhang Yanmin	(China)
A.S.Zubchenko	(Russia)

Promotion group:

V.N.Lipodaev, V.I.Lokteva
A.T.Zelnichenko (exec. director)

Translators:

A.A.Fomin, O.S.Kurochko,
I.N.Kutianova, T.K.Vasilenko
PE «Melnik A.M.»

Editor

N.A.Dmitrieva

Electron galley:

I.S.Batasheva, T.Yu.Snegiryova

Address:

E.O. Paton Electric Welding Institute,
International Association «Welding»,
11, Bozhenko str., 03680, Kyiv, Ukraine

Tel.: (38044) 287 67 57

Fax: (38044) 528 04 86

E-mail: journal@paton.kiev.ua

http://www.nas.gov.ua/pwj

State Registration Certificate
KV 4790 of 09.01.2001

Subscriptions:

\$324, 12 issues per year,
postage and packaging included.
Back issues available.

All rights reserved.

This publication and each of the articles
contained herein are protected by copyright.
Permission to reproduce material contained in
this journal must be obtained in writing from
the Publisher.

Copies of individual articles may be obtained
from the Publisher.

CONTENTS

Paton B.E. 25 years of welding in open space 2

SCIENTIFIC AND TECHNICAL

*Kuchuk-Yatsenko S.I., Zychor I.V., Velikoivanenko E.A. and
Rozyinka G.F.* Calculation of thermal-deformation conditions of
formation of friction welded joints on heat-resistant alloy
EI698VD 7

Skulsky V.Yu. Peculiarities of kinetics of delayed fracture of
welded joints of hardening steels 12

*Markashova L.I., Grigorenko G.M., Poznyakov V.D.,
Berdnikova E.N. and Alekseenko T.A.* Influence of thermal
cycles of welding and external loading on structural-phase
variations and properties of joints of 17Kh2M steel 18

Razmyshlyayev A.D. and Mironova M.V. Calculation of
parameters of longitudinal magnetic field providing removal of
drop from electrode tip in arc surfacing 26

INDUSTRIAL

*Paton B.E., Shelyagin V.D., Akhonin S.V., Topolsky V.F.,
Khaskin V.Yu., Petrichenko I.K., Bernatsky A.V., Mishchenko
R.N. and Siora A.V.* Laser welding of titanium alloys 30

Uratani Yo., Takano G., Nayama M. and Shimokusu Yo.
Application of electron beam welding in the nuclear industry
(Review) 35

*Yushchenko K.A., Bulat A.V., Levchenko O.G., Bezushko O.N.,
Samoilenko V.I., Dovgal D.I. and Kakhovsky N.Yu.* Effect of
composition of base metal and electrode covering on hygienic
properties of welding fumes 44

Golovko V.V. and Goncharov I.A. Method for evaluation of
fracture resistance of welding flux granules 49

BRIEF INFORMATION

*Lazorenko Ya.P., Kolyada V.O., Shapovalov E.V., Lutsenko
N.F. and Skuba T.G.* Effectiveness of application of algorithms
for identification of weld reinforcement in digital images 51

25 YEARS OF WELDING IN OPEN SPACE

Prof. **B.E. PATON**

On July 25, 1984 Svetlana Savitskaya and Vladimir Dzhanibekov, USSR pilot-cosmonauts, conducted world's first experiments on welding, cutting, brazing and coating in open space. Successful performance of unique experiments in space environment demonstrated the possibility of effective activity of cosmonauts when performing complex operations on welding and related technologies on board the manned orbital complex in open space, and is indicative of a high perfection of welding hardware, created during many years of intensive work of a large team of scientists and engineers of the E.O. Paton Electric Welding Institute in close cooperation with Yu.A. Gagarin Cosmonaut Training Center. Sergej Pavlovich Korolyov, founder of practical cosmonautics, outstanding designer of Soviet space systems, already at the start of 1960s foresaw the need to perform in space the operations, involving welding, and provided all kinds of support for research on welding and cutting in space. In 1964 S.P. Korolyov set the task of development of a program of welding experiments in space and plan of joint work of OKB-1 (now Rocket-Space Corporation «Energiya») and the E.O. Paton Electric Welding Institute of AS of the Ukr. SSR. Thus, the Institute started fulfilling a research program, the final aim of which was development of equipment and technologies for joining materials in space by welding. On October 16, 1969 during the flight of «Soyuz-6» spaceship pilot-cosmonauts G. Shonin and V. Kubasov performed welding and cutting of metals



Savitskaya Svetlana Evgenievna — Russian pilot-cosmonaut, two times Hero of the Soviet Union

Born on August 8, 1948 in Moscow, graduated from the Moscow Aviation Institute and Central Flight-Engineering School of DOSAAF of the USSR. In 1980 joined the cosmonaut unit. S.E. Savitskaya made her first space flight in 1982. On July 25, 1984 she took the world's first space walk, staying for 3 h 45 min outside the spaceship. During the time she together with V.A. Dzhanibekov performed experiments on welding and related technologies. In 1986 she defended the thesis of Candidate of Sciences. Up to 1989 S.E. Savitskaya worked as Deputy Department Head of SPA «Energiya». In 1992–1995 she was Assistant Professor of the Moscow State Aviation Institute. Starting from 1995 she has been the Deputy of RF State Duma.



Dzhanibekov Vladimir Aleksandrovich — Russian pilot-cosmonaut, two times Hero of the Soviet Union

Born on May 13, 1942, in Iskandar settlement, Taskent district, Uzbekistan. In 1965 graduated from Eisk Higher Aviation School of Pilots and served as pilot-instructor in the USSR Air Force. Starting from 1970 he has been member of the cosmonaut unit. Performed 5 space flights, including international missions, as spaceship commander. Performed his first space flight in 1981. In 1984 during the fourth flight conducted an experiment on welding in open space together with flight-engineer S.E. Savitskaya. From 1985 up to 1988 he was the cosmonaut unit leader, and from 1988 — Head of Theoretical and Research Training Department of Yu.A. Gagarin Cosmonaut Training Center. In 1997 he was transferred into the reserve.

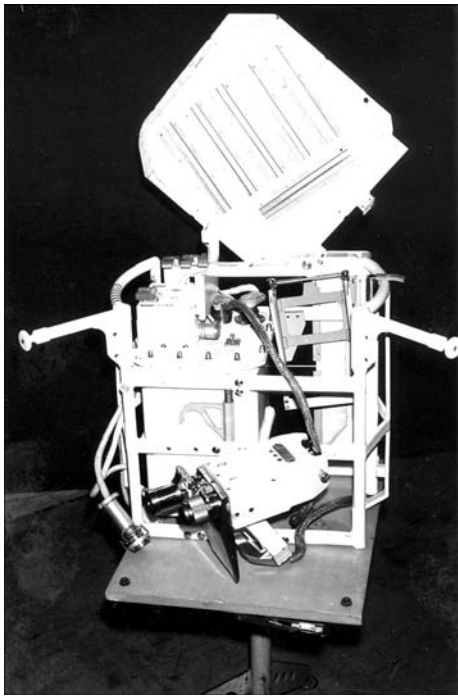


Figure 1. Versatile handtool

in space in an all-purpose automated «Vulkan» unit for the first time in the world. This experiment, which was the start of the space technology era, showed that the electron beam is the most promising energy source for performing the operations on welding and related technologies in open space. Later on strong support in performance of space experiments on welding and related technologies was provided by V.P. Glushko, Chief Designer of rocket-space systems, who has directed RSC «Energiya» for a long time.

Programs of space exploration, performed currently and planned for the future, envisage construction of large-sized space facilities in space and on the Moon. Naturally, long-time operation of such facilities requires systematic preventive maintenance, as well as repair-restoration and mounting operations both inside and outside the sealed compartments. In our opinion, welding is one of the most promising technologies for these purposes. During operation in open space, the most unexpected situations can develop, which require application of welding and related technologies, and quite often the cosmonaut will have to determine the kind and scope of operations directly in site. The cosmonauts will have to work in different sections of the space vehicle and deal with various structural materials.

It is exactly for these purposes that the E.O. Paton Electric Welding Institute developed a versatile electron beam handtool (VHT) (Figure 1). In connection with the unique nature of the experiment a large series of ground-based testing in a manned space simulation test chamber, at short-term zero-gravity in a flying laboratory and at zero buoyancy was performed in order to conduct it in open space (Figure 2).

VHT testing in open space was performed on board of «Salyut-7» orbital station. After depressurizing of the transfer module and hatch opening V. Dzhanibekov took VHT to the outer surface of the station and mounted it on the anchoring platform hand-rails. S. Savitskaya, being in the transfer module, helped the commander in transporting the VHT. Then the cosmonauts changed places. Fastening herself to the anchoring platform, S. Savitskaya started performing the experiment. She cut a titanium sample, and then performed welding, brazing and coating, successively changing the samples. During this time V. Dzhanibekov conducted TV reporting and filming of individual moments of flight engineer activities. After completion of the first stage of the work, the cosmonauts again changed places, and V. Dzhanibekov performed all the operations on the rest of the samples. Great assistance and support to the direct performers, who were outside the spaceship, was provided by cosmonaut-researcher I. Volk. After completion of the experiment, VHT was taken back to the station. The experiment in open space lasted for 3 h 35 min.

Samples of stainless steel and titanium alloy 0.5–1.0 mm thick were used to perform technological experiments on welding, cutting and brazing, and aluminium samples were used for silver coating deposition using VHT in open space. Welded samples processed in space and brought back to Earth (Figure 3), were comprehensively studied. Results of the conducted studies show that the structure and properties of welded joints



Figure 2. S.E. Savitskaya and V.A. Dzhanibekov, USSR pilot-cosmonauts, during preflight testing of the welding tool

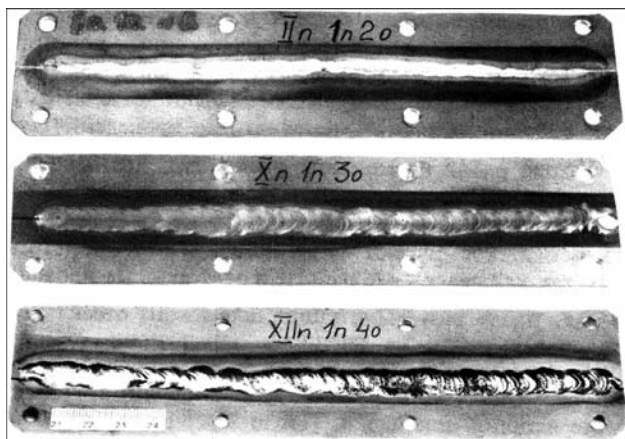


Figure 3. Samples of butt joints made in space using VHT hardware

produced manually by the electron beam in open space and on Earth are close. The available slight differences, not affecting the quality of welded joints of «space» samples, can, apparently, be attributed to the features of the space environment and heat sink conditions.

Before returning to Earth the cosmonauts removed from the boards the samples, which were later transferred to the E.O. Paton Electric Welding Institute for investigations. Cosmonauts S. Savitskaya and V. Dzhanibekov showed genuine heroism, taking the role of pioneers in these basic space experiments (Figure 4). They


literally broke the ice of mistrust of the skeptics, who were doubting the very possibility of applying welding technologies in space. Their feat has become part of the history of development of welding science and technology for ever.

Tens of thousands of people — designers, technologists, workers-assemblers of hardware, test engineers and cosmonauts — promoted performance of this unique experiment by their really self-sacrificing work. Unfortunately, the small scope of a journal paper does not allow mentioning the contribution of each participant to development and testing of VHT — the electron beam gun, control and power systems, as well as the cosmonaut's workplace, without which it would have been impossible to implement the process of welding in open space. However, I cannot but mention two staff members of the E.O. Paton Electric Welding Institute, who made a tremendous contribution to VHT development. These are V.F. Lapchinsky and A.A. Zagrebelny. Both VHT development and conducting the experiments by heroes-cosmonauts was made possible largely due to their tremendous efforts.

Alongside the test engineers, members of the main and standby crews: V. Dzhanibekov, S. Savitskaya, V. Vasyutin and E. Ivanova took an active part in experiment performance. Having



Figure 4. B.E. Paton, V.A. Dzhanibekov, S.E. Savitskaya after completion of the flight experiment



been familiarized with the experiment purpose and hardware, they followed the test engineers' work, participated in discussion and analysis of its results, and after than they started training, during which they mastered the techniques and skills of manual welding, having learned to control the behaviour of the molten metal pool. The main attention during experiment performance was given to checking the hardware serviceability and operator actions during performance of welding and other operations in open space.

The experiment showed that compact versatile tools of VHT type will allow the cosmonauts conducting repair or mounting operations on the outer surface of the space vehicle, while ensuring the required quality of welded joints. When VHT was developed, special attention was given to safety of the performed operations. This issue was particularly thoroughly studied during performance of numerous tests, as violation of safety rules at operation with the electron beam might lead to irreparable consequences, related to the crew lives and station functioning. Performance of multifaceted activities allowed solving the task of ensuring the safety of the crew and vehicle due to special design solutions for the tool proper and organization of the cosmonaut's workplace. In particular, 5 kV accelerating voltage was used in order to eliminate the impact of X-ray radiation on welding operator at operation of the electron beam gun. Small-sized high-voltage block directly built into the handtool allowed eliminating the high-voltage cable, which is an increased hazard source. A short-focus electron beam gun was used in the handtool, to increase the level of cosmonaut-operator safety and protect the space vehicle skin from being accidentally hit by the beam. In addition, during performance of the experiment the hardware was mounted in such a way on the station outer surface that the gun were aimed away from the station board towards the open space during welding operation performance. A great contribution into organizing, preparation and performance of the experiment on manual electron beam welding was made by the staff of SPA «Energiya» led by V.P. Nikitsky, Laboratory Head.

In 1986 the program of VHT testing was carried on. Cosmonauts V. Solovyov and L. Kizim used the tool to perform manual electron beam welding and brazing of components and fragments of advanced truss structures on the station outer surface, thus allowing another significant step forward to be made from conducting experiments on samples to welding elements and components of the real structures.

Activities conducted on board the station using VHT revealed the need for the tool modification, and, primarily, increase of its output power.

A new generation of the versatile handtool — «Universal» hardware — was developed to solve these problems (Figure 5). In this hardware the output power was considerably increased (more than 2 times). «Universal» complex passed comprehensive ground-based testing and was recommended for application as part of the future orbital stations, in particular, as a standard system for the «Mir» orbital station.

In view of the achievements of the E.O. Paton Electric Welding Institute in the field of welding in space, at the start of 1990s the USA National Space Agency (NASA) suggested conducting a joint experiment on welding and related technologies on board the space shuttle «Columbia». The International Space Welding Experiment was scheduled for the end of 1997. However, it did not take place, in connection with a number of serious malfunctions on board the space vehicle. This experiment was also prepared for performance in the «Mir» station. After qualification testing, «Universal» hardware was taken on board the station, but, unfortunately, the experiment was not conducted, because of station liquidation. We believe that performance of the scheduled experiments will be useful for future development of space technologies.

Over the recent years the E.O. Paton Electric Welding Institute has been developing a new generation of equipment for performance of welding and related technologies in open space. In order to cover the entire range of thicknesses of various materials applied for development of space flying vehicles, including manned orbital stations, it is necessary to increase the power of welding

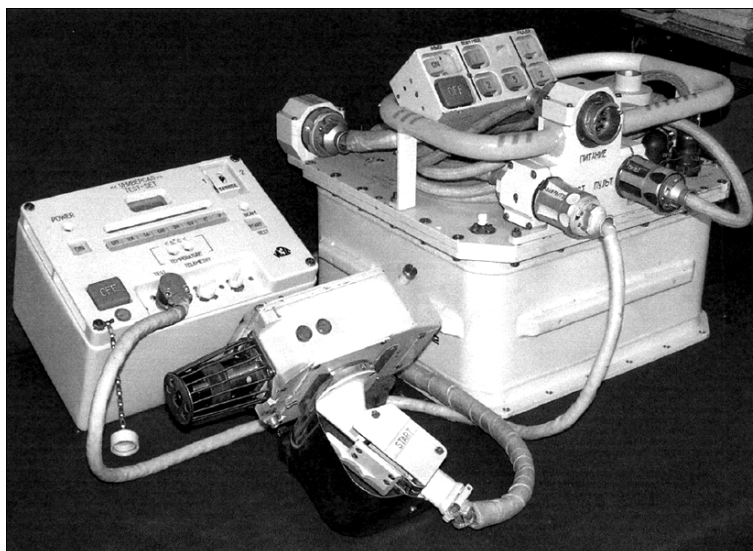


Figure 5. «Universal» hardware for manual electron beam welding

hardware, develop a new specialized power source, and new design of the electron beam gun. Equipment is developed so that the hardware could allow performing not only manual, but also mechanized operations using robotics and other automated devices. Intensive development of modern equipment and technology really widens the technological capabilities of welding operations performance in the space environment. In particular, it appears to be highly promising to apply the modern fiber lasers, which have a rather high efficiency. In this case, it is possible to transport the beam to the tool for welding performance along an optical light guide for many meters.

Space vehicles and stations, as well as infrastructure of lunar outposts designed for long-term operation in space, should be fitted with welding hardware systems, allowing performance of mounting and repair operations in construction and operation of facilities, and the vehicle and mission crews should master the basic welding technologies and should have practical skills of performance of the above operations.

We are convinced that welding and related technologies will have a significant role in space exploration in the future. Electron beam technologies, tested in open space, can be applied in different physical experiments, and then also in manufacturing of unique semi-conductor materials. This will allow going over from experiments with the electron beam in orbital stations to construction of lunar outposts and implementation of various productions on the Moon already in the first half of the XXI century.



CALCULATION OF THERMAL-DEFORMATION CONDITIONS OF FORMATION OF FRICTION WELDED JOINTS ON HEAT-RESISTANT ALLOY EI698VD

S.I. KUCHUK-YATSENKO, I.V. ZYAKHOR, E.A. VELIKOIVANENKO and G.F. ROZYNKA

E.O. Paton Electric Welding Institute, NASU, Kiev, Ukraine

Thermal-deformation conditions of formation of friction welded joints on heat-resistant nickel alloy EI698VD were estimated. The possibility of reaching the melting point of the heat-resistant alloy within the contact zone at a stage of heating was proved, and behaviour of the melt at all stages of the process was studied. Methods for optimisation of the technology of friction welding of heat-resistant nickel alloys, and methods for minimisation of width of the phase transformation zone in welded joints were suggested.

Keywords: heat-resistant nickel alloys, friction welding, welding process parameters, welded joint, strengthening γ -phase, mathematical model, melting temperature, contact zone

Strain-hardening nickel-base alloys with a strengthening γ -phase content of 10–60 vol.% are used to manufacture components of gas turbine engines (GTE) [1–3]. In particular, Russia and Ukraine use to advantage alloys EI698VD (KhN73MBTYu) and EK79, as well as alloy EP741NP produced by the granule metallurgy method. Friction welding (FW) holds much promise for the manufacture of welded assemblies of GTE operating under high temperature and loading conditions.

It is a known fact that for the sound joints to be formed in FW, it is necessary to generate a certain deformation, which would provide displacement of oxides and adsorbed films outside the sections of workpieces [4]. The deformation temperature range (DTR) of an alloy depends upon its chemical composition, and is limited by solvus temperature $T_{d\gamma}$ (complete dissolution of the strengthening γ -phase), on the one hand, and solidus temperature T_{melt} (beginning of melting), on the other hand. DTR becomes narrower with increase in volume content of the γ -phase, i.e. the temperature of the beginning of melting decreases, and the temperature of complete dissolution of the γ -phase increases (Table 1). DTR recommended by industrial standards is even narrower [5].

The possibility of ensuring the required deformation (upsetting) for quality welding depends upon such FW process parameters as rotation speed v_r ($v_r =$

πdn , where d is the diameter of workpieces, and n is the rotation frequency), pressure P and time t (Figure 1).

As a rule, the optimal values of these parameters are determined by comparing mechanical properties of welded joints made by using different process parameters. To evaluate phase changes in metal (degree of degradation of the strengthening γ -phase) within the welded joint zone, it is necessary to know the data on temperature-time conditions of formation of joints on specific alloys. As direct measurements of the temperature of metal within the contact zone in FW are difficult [6], it is of a research and practical interest to evaluate thermal-deformation conditions of formation of joints on heat-resistant alloys by calculations.

The purpose of this study was to calculate thermal cycles of FW of heat-resistant nickel alloy EI698VD depending upon the welding process parameters, estimate the effect of the thermal-deformation cycle of FW on phase composition of the joining zone metal, and develop recommendation for optimisation of the FW technology.

The thermal cycles were calculated by using the developed mathematical model of the heating process in FW. The model is based on the equation of thermal conductivity and characteristics of consumption of power of the FW process by a material.

Temperature field $T(r, z, \tau)$ at arbitrary moment t is found from the known temperature field equal to

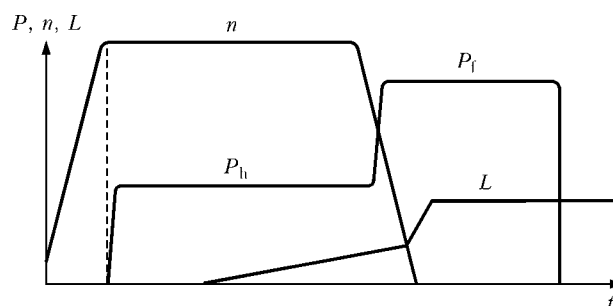


Figure 1. Typical cyclogram of FW process: L — upsetting in welding; P_h , P_f — pressure in heating and forging, respectively

Table 1. Phase characteristics and DTR of heat-resistant alloys

Alloy	Content of γ -phase, vol. %	Critical points, °C		Recommended deformation temperature, °C
		$T_{d\gamma}$	T_{melt}	
EI698VD	20	1020	1320	1000–1180
EK79	35	1100	1280	1100–1130
EP741NP	60	1185	1270	1185–1200

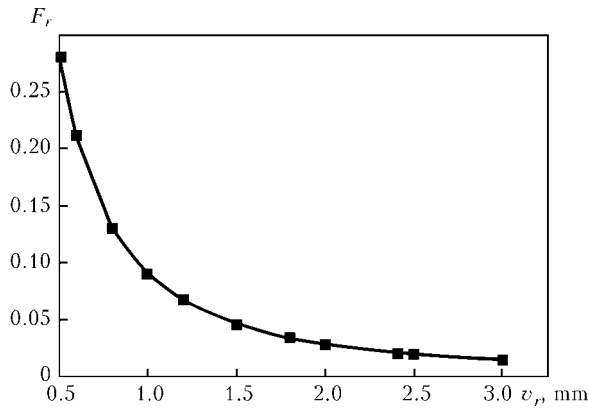


Figure 2. Friction coefficient F_r versus rotation speed v_r ($F_r = A/v_r^k$, where $A = 0.09$, and $k = 1.65$)

$T(r, z, t - \Delta t) = T^*$ at moment $t - \Delta t$, where Δt is the step of time tracing of variations in the temperature field, starting from initial state $t = 0$. Temperature $T = T(r, z, t)$ is determined at each tracing step by the variational method as a result of minimising the following functional:

$$E_h = -\frac{1}{2} \iint_S \times \left[r\lambda \left(\frac{\partial T}{\partial r} \right)^2 + r\lambda \left(\frac{\partial T}{\partial z} \right)^2 + rc\gamma \frac{T^2}{\Delta t} - 2rT \left(\frac{T_e}{\Delta t} c\gamma + W \right) \right] \times \times drdz + \frac{1}{2} \int_{\Gamma} r\alpha_h (T - 2T_e) T d\Gamma, \quad (1)$$

where $\lambda = \lambda(T)$ is the coefficient of thermal conductivity of the material; $c\gamma = c\gamma(T)$ is the volumetric heat capacity; $W = W(r, z, t)$ is the power of the source of heat released due to friction; S is the studied cross section area of a workpiece in plane (r, z) ; Γ is the contour limiting the surface with area S , at which the boundary condition of heat exchange with the environment is set, following the Newton's law, having the coefficient of heat exchange α_h ; and T_e is the temperature of the environment.

Minimisation of functional (1) with respect to $T(r, z, t)$ yields the two-dimensional equation of thermal conductivity in the cylindrical system of coordinates r, z :

$$\frac{\partial}{\partial r} \left(\lambda r \frac{\partial T}{\partial r} \right) + r \frac{\partial}{\partial z} \left(\lambda \frac{\partial T}{\partial z} \right) + Wr = rc\gamma \frac{\partial T}{\partial t} - 2\alpha_h (T_e - T). \quad (2)$$

The initial temperature was assumed to be equal to 20 °C, and boundary conditions corresponded to conditions of heat exchange with the environment:

$$\lambda \frac{\partial T}{\partial r} = -\alpha_h (T_e - T); \quad \lambda \frac{\partial T}{\partial z} = -\alpha_h (T_e - T). \quad (3)$$

Power of the heat source, $W(r, z, t)$, was determined by using the formula from study [7]:

$$W = P v_r F_r, \quad (4)$$

where P is the pressure in heating, MPa; and F_r is the friction coefficient at the surfaces being welded.

The value of F_r in FW of alloy EI698VD was determined by the procedure described in [8]. Variations in friction coefficient F_r depending upon rotation speed v_r are shown in Figure 2.

It was assumed in the calculations that heat is released over the entire friction surface, that heat release stops with formation of liquid phase within the contact zone, and liquid metal is displaced to flash.

The temperature problem was solved by the finite element method. Functional (1) corresponds to the quadratic form, which is a sum of all elements of the area under consideration:

$$E_h = -\frac{1}{2} \sum_m \sum_n \times \left\{ (r\lambda)_{m,n} \left[\left(\frac{T_{m,n} - T_{m-1,n}}{\Delta r_{m,n-1}} \right)^2 + \left(\frac{T_{m,n} - T_{m,n-1}}{\Delta z_{n,n-1}} \right)^2 \right] - 2W_{m,n} T_{m,n} r_{m,n} \Delta r_{m,n-1} \Delta z_{n,n-1} \right\} \quad (5)$$

Minimisation of quadratic formula (5) with respect to the values of temperature $T_{m,n}$ at the right upper node of a finite element yields the system of linear algebraic equations:

$$\begin{aligned} & T_{m+1,n} \lambda_{m+1,n} r_{m+1} \frac{\Delta z_{n+1,n}}{\Delta r_{m+1,m}} + \\ & + T_{m,n+1} \lambda_{n,n+1} r_m \frac{\Delta r_{m,m+1}}{\Delta z_{n+1,n}} + \\ & + T_{m-1,n} \lambda_{m,n} r_m \frac{\Delta z_{n,n-1}}{\Delta r_{m,m-1}} + \\ & + T_{m,n-1} \lambda_{m,n} r_m \frac{\Delta r_{m,m-1}}{\Delta z_{n,n-1}} - \\ & - T_{m,n} \left[r_m \lambda_{m,n} \frac{\Delta z_{n,n-1}}{\Delta r_{m,m-1}} + r_{m+1} \lambda_{m+1,n} \frac{\Delta z_{n+1,n}}{\Delta r_{m+1,n}} + \right. \\ & + r_m \lambda_{m,n+1} \frac{\Delta r_{m,m+1}}{\Delta z_{n+1,n}} + \frac{c\gamma_{m,n}}{\Delta t} r_m \times \\ & \times \Delta r_{m,m-1} \Delta z_{n,n-1} \left. + \left(W_{m,n} + \frac{c\gamma_{m,n}}{\Delta t} T_{m,n}^{(k-1)} \right) r_m \Delta r_{m,m-1} \Delta z_{n,n-1} \right] = 0 \\ & (m = 1, 2, \dots, M; \quad n = 1, 2, \dots, N), \end{aligned} \quad (6)$$

where M and N are the quantities of finite elements on radius r and rotation axis z , respectively.

For a complete statement of the problem, the following boundary conditions should be added to the system of equations (6):

$$\lambda \frac{T_{m,n} - T_{m-1,n}}{\Delta r_{m,m-1}} = -\alpha_h (T_e - T_{m,n}), \quad (6a)$$

$$\lambda \frac{T_{m,n} - T_{m,n-1}}{\Delta z_{n,n-1}} = -\alpha_h (T_e - T_{m,n}). \quad (6b)$$

The system of equations (6) through (6b) was solved by the Gaussian method. The thermal cycles were calculated for FW of the 16 mm diameter solid

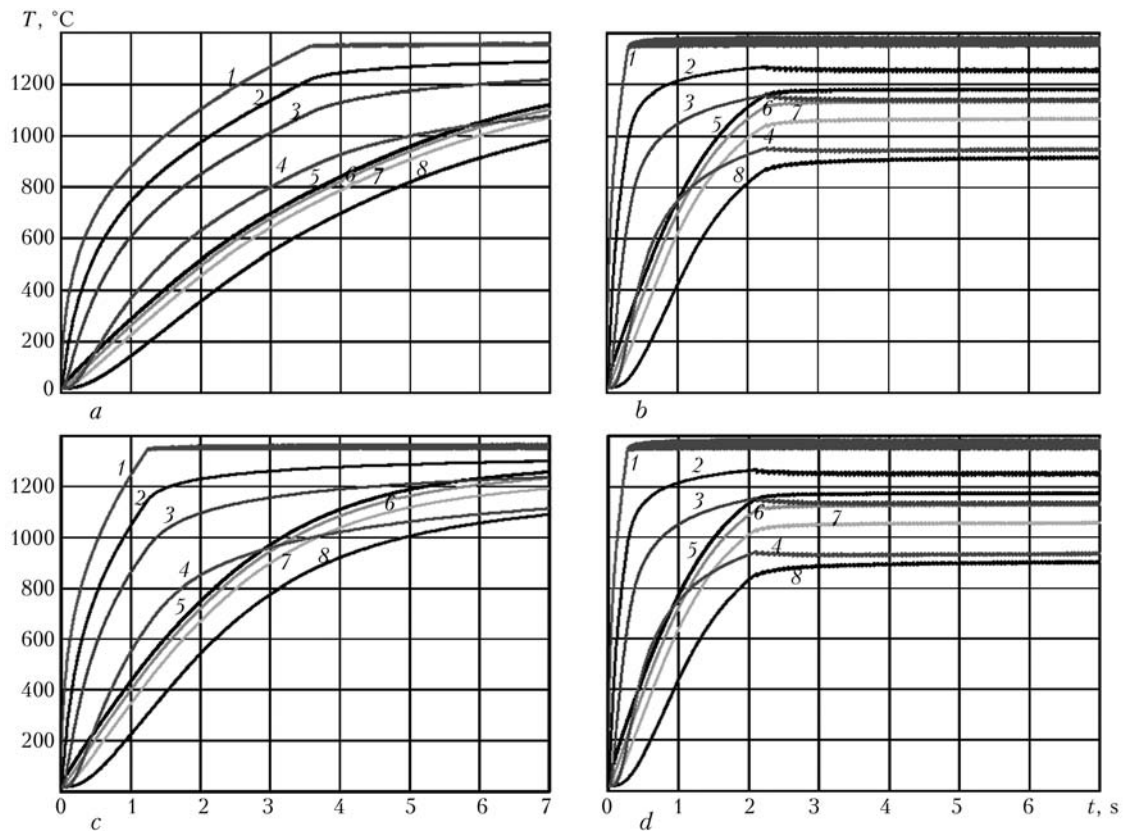


Figure 3. Variations in temperature of 16 mm diameter solid pieces of alloy EI698VD in FW at different distances from contact surface z (axial direction) and centre of section r (radial direction) at $v_r = 2$ (a, b) and 1 (c, d) m/s, $P = 100$ (a), 200 (c) and 600 (b, d) MPa: 1 – $z = 0$, $r = 8$ mm; 2 – $z = 0.5$ mm, $r = 8$ mm; 3 – $z = 1$ mm, $r = 8$ mm; 4 – $z = 2$ mm, $r = 8$ mm; 5 – $z = 0$, $r = 0$; 6 – $z = 0.5$ mm, $r = 0$; 7 – $z = 1$ mm, $r = 0$; 8 – $z = 2$ mm, $r = 0$

pieces of alloy EI698VD, allowing for its thermal-physical properties (Table 2). Rotation speed at the selected rotation frequencies was $v_r = 0.5, 1.0$ and 2.0 m/s, and pressure was varied from 100 to 600 MPa.

Figure 3 shows the calculated distribution of temperature in the pieces for certain combinations of process parameters.

As shown by the calculation of distribution of temperature $T(x, t)$, the temperature of the beginning of melting of alloy EI698VD is reached within a short period of time after the beginning of welding. At $P =$

$= 200\text{--}600$ MPa, this time is $0.5\text{--}1.5$ s. Further on the temperature in the contact plane stops growing, and heating of the pieces occurs in the axial direction. At a substantial temperature gradient within the contact zone, no displacement of metal from the joint occurs in the axial and radial directions at the initial stage of the FW process. It can be seen from oscillograms of variations in upsetting at different process parameters that the beginning of shortening of the pieces takes place approximately 2 s after the beginning of the FW process (Figure 4).

The measurement of friction moment M in FW of alloy EI698VD by the procedure described in [9] evidences that the value of M remains at a high level (Figure 5). In this connection, it can be assumed that the melt forms in separate regions of the contact surface, which later on are subjected to intensive deformation, then move in the radial direction and are displaced from the joint to flash.

The beginning of upsetting of pieces is caused by reaching a certain temperature gradient within the

Table 2. Thermal-physical properties of alloy EI698VD

$T, ^\circ\text{C}$	$c \cdot 10^3, \text{J}/(\text{m}^3 \cdot ^\circ\text{C})$	$\lambda, \text{W}/(\text{m} \cdot ^\circ\text{C})$
50	3.76	11.7
100	3.80	11.7
200	3.88	13.4
300	4.00	14.6
400	4.15	15.9
500	4.33	17.6
600	4.54	19.7
700	4.96	21.3
800	5.50	23.0
900	5.50	24.7
1000	5.42	24.7
1100	5.38	24.7
1200	5.38	24.7

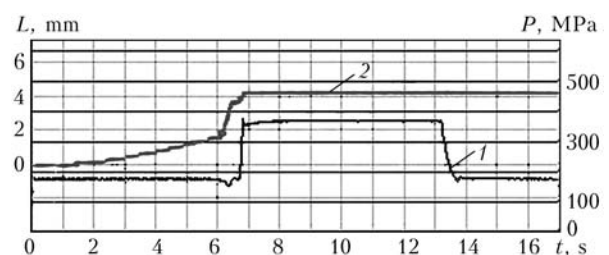


Figure 4. Oscillogram of variations in pressure P (1) and displacement (upsetting) L (2) in FW of alloy EI698VD

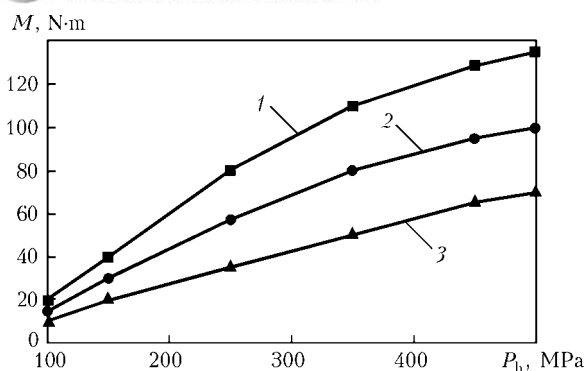


Figure 5. Friction moment M versus pressure P_h at a steady stage of heating in FW of alloy EI698VD at $v_r = 0.5$ (1), 1.0 (2) and 2.0 (3) m/s

contact zone in the axial, z , and radial, r , directions. Analysis of the curves in Figure 3 shows that for the beginning of deformation in macrovolumes of the pieces it is necessary to heat them above solvus temperature $T_{d\gamma}$ to a depth of $z = 1-2$ mm in the peripheral part of sections of the pieces, and $z \approx 0.5-1.0$ mm — in their central part. The higher values of pressure correspond to the lower values of z in the above ranges.

The intensity of energy release in the heating process depends upon the rotation speed and pressure. Thus, as the pressure increases and rotation speed decreases within the investigated ranges of values, heat release within the contact zone grows. This is probably related to a non-linear dependence of friction coefficient F_r upon rotation speed v_r (see Figure 1). The maximal temperature in the joint does not grow, i.e. the intensification of heating with increase in pressure and decrease in rotation speed is compensated for by increase of the upsetting speed (Figure 6), which is accompanied by displacement of the heated metal from the contact zone. The results obtained are in good agreement with the data of studies [10, 11] on increase of the power of heat release and width of the viscoplastic flow of metal with increase in pressure and decrease in rotation speed in FW of steel.

The distribution of temperature along the generating line after interruption of heating at different values of P and $v_r = 0.5, 1.0$ and 2.0 m/s is shown in Figure 7. It can be seen from this Figure that the temperature gradient along the length of the pieces grows with decrease in v_r and increase in P .

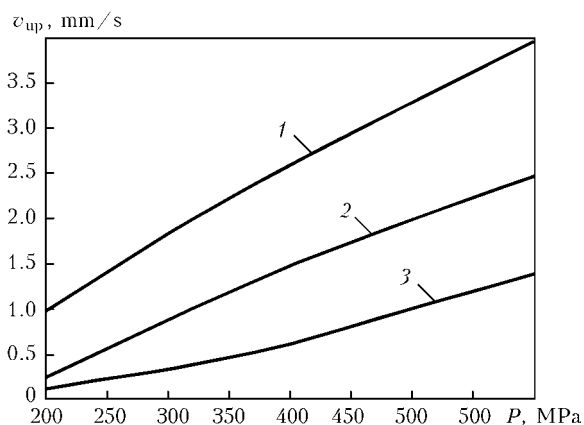


Figure 6. Calculated dependence of upsetting speed v_{up} upon pressure P in FW of alloy EI698VD: 1-3 — see Figure 6

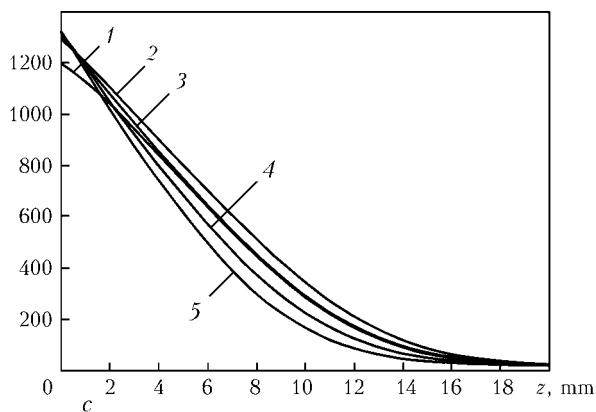
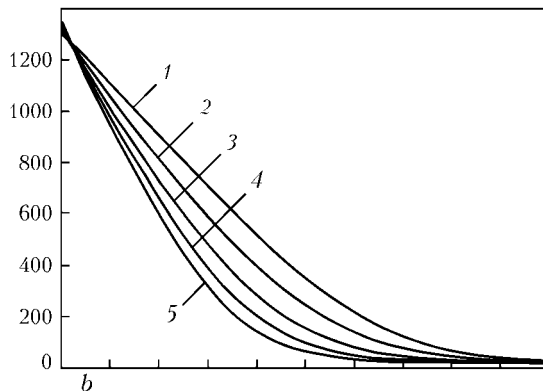
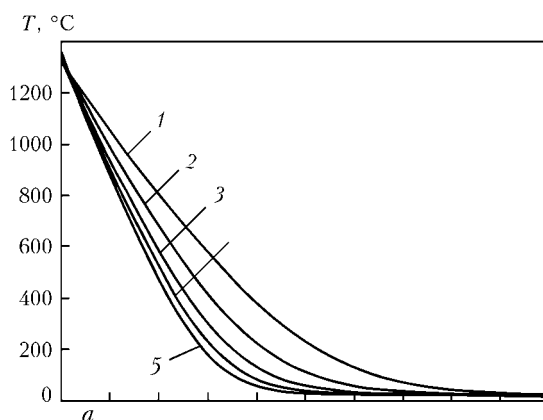


Figure 7. Temperature fields in joining zone on alloy EI698VD after FW at $v_r = 0.5$ (a), 1.0 (b) and 2.0 (c) m/s: 1 — $P = 200$; 2 — 300; 3 — 400; 4 — 500; 5 — 600 MPa

The calculation results show that, as the melting temperature is achieved in the contact zone, at any values of the FW process parameters one might expect dissolution of the strengthening γ -phase in the zone of a welded joint. Here the width of the phase transformation zone is determined by the temperature field, namely by width of the zone of metal heating to a temperature above $T_{d\gamma}$. As seen from Figure 7, the width of this zone decreases with decrease in the rotation speed and increase in pressure.

This conclusion is confirmed by the data of durometric examinations of welded joints on alloy EI698VD produced by changing the FW process parameters over wide ranges. The character of distribution of microhardness of metal within the joining zone (the alloy before welding was in a heat-hardened state) is similar at different FW process parameters, the difference being in width of the weakening zone and in minimal values of microhardness of the HAZ

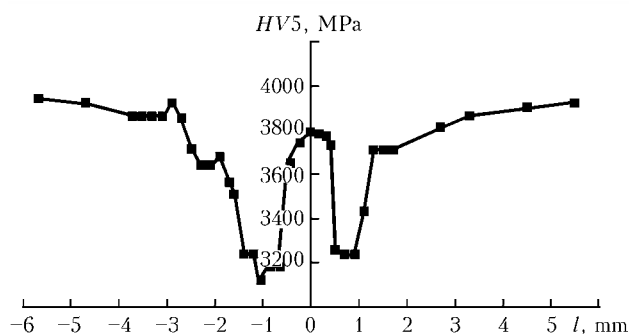


Figure 8. Distribution of microhardness HV in joining zone on alloy EI698VD: l — distance from the joining line

metal in a welded joint (Figure 8). The width of HAZ with decreased microhardness almost coincides with that of the heating zone (above $1020\text{ }^{\circ}\text{C}$ ($T_{d\gamma}$)) determined by calculations at different values of the FW process parameters, which is indicative of the adequacy of the mathematical model. Increase in microhardness of metal in plane of a joint is related to substantial grain refining (Figure 9), this being caused by the process of dynamic recrystallisation of metal of this zone [12].

The error in the calculated values of width of the weakening zone, compared with the data of durometric examinations of welded joints, grow at high values of the rotation speed. For example, at $v_r = 2\text{ m/s}$ ($P = 200\text{--}600\text{ MPa}$), this error is from 7 to 18 %. Most probably, this is associated with the fact that it is impossible to immediately stop rotation. Thus, the time of deceleration of rotation with this speed changed to zero by using the laboratory welding unit ST-120 was 0.2 s. Upsetting of the pieces during this period continued at an increasing speed, width of the HAZ decreased, and the final macro- and microstructure of the joining zone formed at lower values of the rotation speed. It is likely that width of the zone of structural and phase transformations and strength of the welded joints can be effectively influenced by changing the time of the rotation deceleration stage.

Analysis of microstructure of the resulting welded joints revealed no regions of the melt within the sections of the pieces welded. The dynamically recrystallised fine-grained structure of the joining zone evidences that there is no risk of hot cracking in FW of the heat-resistant alloy under investigation.

Analysis of the results obtained allowed suggesting the ways of optimising the FW technology for heat-resistant nickel alloys. To minimise width of the zone of unfavourable phase transformations (dissolution of the strengthening γ -phase) in the joining zone, it is necessary to make the rotation speed low and pressure — high.

The final stage of the FW process, i.e. deceleration of rotation, has a substantial impact on formation of structure of the joining zone. As its time in the process of application of pressure increases, the speed of deformation (upsetting) increases, and width of the zone of structural and phase transformations decreases.

Technologically, the possibility of controlling the final stage of formation of joints can be realised in inertia FW by setting a certain moment of inertia of a flywheel [4, 7], and in FW with regulated decel-

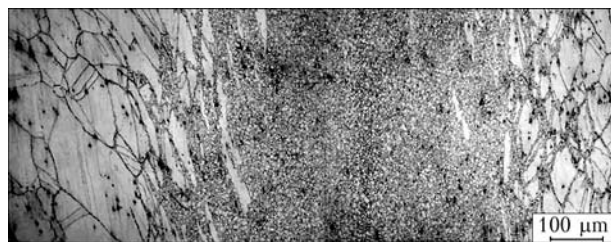


Figure 9. Microstructure of metal of joining zone on alloy EI698VD

eration — through forced deceleration of rotation following the preset program [13, 14].

CONCLUSIONS

1. Analysis of the calculation data obtained by using the developed mathematical model of heating in FW showed that the solidus temperature of alloy EI698VD is achieved within the contact zone. Formation of the melt is of a local character: the melt forms in separate regions of the contact surface, is subjected to intensive deformation, moves in the radial direction and is displaced from the joint to flash.

2. The absence of the cast structure of metal in the joining zone within the section welded is indicative of the absence of the risk of hot cracking in FW of alloy EI698VD.

3. At any values of the FW process parameters, one might expect dissolution of the strengthening γ -phase in plane of the joint. To minimise width of the zone of phase transformations, it is necessary to have a comparatively low rotation speed and high pressure.

4. In FW, the rotation deceleration stage is of a decisive importance for formation of structure of the joining zone metal. Increase in the time of this stage is accompanied by increase in the deformation speed and decrease in width of the zone of structural and phase transformations.

- (2007) Critical technologies for manufacture of the 5th generation of gas turbine engines. *Oborudovanie i Instrument dlya Professionalov*, 95(6), 66–71.
- Bondarev, B.I., Fatkullin, O.Kh., Eryomenko, V.N. et al. (1999) Development of heat-resistant nickel alloys for gas turbine discs. *Tekhnologiya Lyog. Splavov*, 3, 49–53.
- Fatkullin, O.Kh., Garibov, G.S., Nekrasov, V.A. et al. (1999) Development of advanced technologies for heat-resistant nickel alloys. *Ibid.*, 53–61.
- Lebedev, V.K., Chernenko, I.A., Vill, V.I. et al. (1987) *Friction welding: Refer. Book*. Leningrad: Mashinostroyeniye.
- Maslenkov, S.B., Maslenkova, E.A. (1991) *Steels and alloys for high temperatures: Refer. Book*. Book 1. Moscow: Metallurgiya.
- Wichelhaus, G. (1974) Messen der Stossflaechentemperatur beim Reibschweißen. *Schweißen und Schneiden*, 3, 97–100.
- Lebedev, V.K., Chernenko, I.A. (1992) Friction welding. In: *Welding and Surfacing Rev.*, Vol. 2, Pt 4. Harwood A.P., 59–168.
- Lebedev, V.K., Vil, V.I., Chernenko, I.A. (1981) About calculation of energy parameters of the process of friction welding of metals. *Avtomatich. Svarka*, 3, 2–4.
- Lebedev, V.K., Litvin, L.V., Dyshlenko, A.T. et al. (1986) Determination of friction moment in inertia welding from value of angular acceleration. *Ibid.*, 8, 31–33.
- Lebedev, V.K., Mirgorod, Yu.A., Vakulenko, S.A. (1987) Mathematical modeling of thermal processes and viscous flow of metal in friction welding. *Ibid.*, 1, 3–6.
- Lebedev, V.K., Chernenko, I.A. (1984) Power distribution in a joint during friction welding. *Ibid.*, 12, 23–25.
- Adam, P. (1981) Welding of high-strength alloys for gas turbines. In: *Heat-resistant alloys for gas turbines*. Ed. by R.E. Shalin. Moscow: Metallurgiya.
- Kuchuk-Yatsenko, S.I., Zaykhor, I.V. *Method of friction welding and machine for its application*. Pat. 546460 Ukraine. Int. Cl. B 23 K 20/12. Publ. 15.11.2004.
- Zaykhor, I.V. (2001) Modern equipment for friction welding. *The Paton Welding J.*, 7, 48–52.



PECULIARITIES OF KINETICS OF DELAYED FRACTURE OF WELDED JOINTS OF HARDENING STEELS

V.Yu. SKULSKY

E.O. Paton Electric Welding Institute, NASU, Kiev, Ukraine

The factors determining the rate of delayed fracture propagation at hydrogen embrittlement of welded joints of martensite steel at temperatures higher and lower than the revealed minimum of crack resistance (80–100 °C) and joints of bainite steel are considered. In addition to the known concepts it is shown that kinetics of delayed fracture can be determined by the character of distribution in the volume of metal of microplastic deformations, the propagation of which depends on the thermally-activated microstructural changes and rate of formation of local critical density of dislocations and hydrogen. In a general case the dependence of fracture duration on temperature is described using C-like curves.

Keywords: arc welding, hardening steels, welded joints, hardening, martensite, low-temperature decay, bainite, local deformation, delayed fracture, cold cracks

The formation of cold cracks [1, 2] in welded joints of hardening steels takes place at temperatures providing activation of dislocations movement and diffusive mobility of hydrogen in combination with energetic interaction of hydrogen with the traps, i.e. dislocations and microfields of increased elastic stresses (microstresses), sufficient for fracture propagation [3–6]. The initial temperature of possible initiation of cracks at the cooling curve branch is considered by different researchers in a rather wide range: approximately from 300 °C and to the temperature of environment [7–10]. However, the more precise determination of temperature, below which a risk of delayed fracture arises, has a significant applied importance. To specify the temperature range of manifestation of tendency to cold crack formation, it is shown in work [11] that the risk of crack formation in welded joints of martensite steels arises at the temperature below 140–120 °C. In the range of about 80–100 °C these joints have the lowest crack resistance, which is determined by a minimal duration of fracture growth. At lower and higher temperatures the period of fracture increases. It is also shown that joints of steel with bainite-martensite transformation, characterized by a lower level of hardening and higher resistance against cold crack formation, the temperature interval

of cracking is limited by the upper threshold temperature of about 80 °C. To widen the conceptions about the factors influencing the formation of cold cracks, it is necessary to find out the possible reasons of changing the kinetics of a delayed fracture depending on the temperature of joints metal.

The aim of this work is to analyse some physical and metallurgical phenomena influencing the tendency of welded joints of hardening steels to delayed fracture depending on the temperature at which they are at the stage of cooling after the phase recrystallization.

The results of tests, performed using the Implant method at maintaining the constant temperature of welded joints in the range of about from 160 °C down to the room temperature, were used in this work. The test machine was equipped for this purpose by the system of automatic control of temperature and heating and started operation when the joint reached the preset temperature at the curve branch of cooling after completion of welding [11]. The experiments were performed using a manual arc welding with covered electrodes. To load the welded joints, the lever system with changeable loads was used. In the process of specimen testing the load remained unchanged. The movement λ in a welded joint was recorded using sensors [12], that allowed evaluation of creep rate $\dot{\epsilon}$ ($\dot{\epsilon} = \Delta\lambda / \Delta t$, where $\Delta\lambda$, Δt is the increment of movements and relative time period, respectively) [13] at the steady stage of delayed fracture development (Figure 1). To evaluate the energy of activation of processes considered in the work, the results of measurement of speed of process studied at different temperatures (at delayed fracture – creep rate) and an approach based on the relation, correlated the process speed with energy of activation and temperature were used [14, 15]:

$$\dot{\epsilon} = A \exp \frac{-E}{RT},$$

where E is the energy of activation, kJ/mole; R is the universal gas constant; T is the absolute temperature, K; A is the constant.

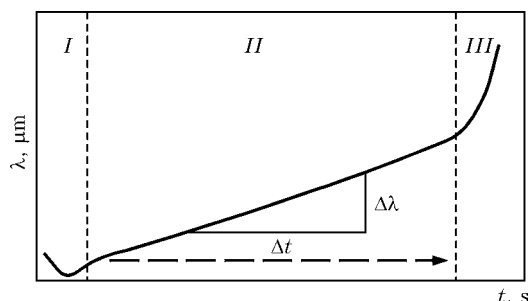


Figure 1. Diagram of development of creep at a delayed fracture: I – initial stage of increment of movements; II – stage of a steady creep; III – fracture; dotted line – absence of deformation and fracture

To perform the dilatometric investigations of peculiarities of low-temperature tempering of martensite, the specimens of steels with a martensite transformation, hardened in water after furnace heating up to 1200 °C, were applied.

The results of tests of joints of steels, hardened with a formation of martensite structure, are shown in Figures 2 and 3. In the experiments the electrodes, providing the martensite structure of deposited metal, were used: to weld specimens of steels 10Kh9MFB, 25Kh2NMFA — FOX C9MV (Boehler, Austria), 38KhN3MFA — experimental electrodes with alloying close to steel. The revealed dependence of technological strength on temperature was, probably, due to peculiarities of growth of thermally-activated processes influencing the structural changes and process of crack formation.

According to the existing concepts the delayed fracture is the result of a gradual growth of interatomic breaks in the zones with an increased density of defects of crystalline structure and microstresses under the influence of hydrogen [16–18]. The beginning of fracture is preceded by the stage of ionized hydrogen accumulation in the prefracture zone up to concentration, sufficient to formation of a microbreak. The main contribution to achievement of a critical state of metal and initiation of its fracture is made by dislocations, transporting or binding the hydrogen in the zone of their accumulation near obstacles, usually near grain boundaries. In this connection, the local microplastic deformation, as a result of starting and moving of dislocations in the most pliable microareas under the influence of stresses, is considered as initial (and necessary) stage of a delayed fracture [3, 19, 20]. The fracture development, representing consecutive alternation of actions of initiation and growth of microcracks, is also accompanied by a gradually growing deformation under the action of applied load. It is this kind of deformation, i.e. creep, caused by formation and growth of inner defects, that is recorded in the process of testing (see Figure 1).

Thus, the locality of initial microplastic deformation is the main factor of fracture development. In its turn, the distribution of microdeformations in large volumes impedes the formation of a local critical state sufficient to originate the sources of fracture and its further propagation [13]. Therefore, the heterogeneity of microstructure, the presence and character of distribution of microareas prone to deforming in the volume of a rigid matrix, can essentially influence the reduction of resistance against the delayed fracture, that is also confirmed by the data of work [19].

The mechanical and technological properties of martensite metal depend on the level of tempering (or decay) of initial hardened solid solution. Though the notable decrease in strength and, consequently, improvement in ductility occur even at holding of hardened metal within the range of relatively low temperatures, approximately from 100 up to 200 °C [20]. The similar structural changes should influence the

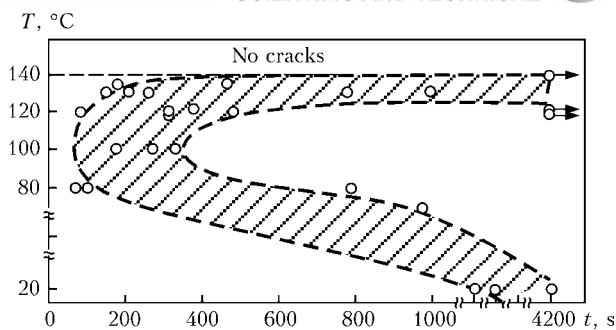


Figure 2. Character of change of time of a delayed fracture of martensite steel 10Kh9MFB welded joints depending on temperature (tests at loading stress $\sigma = 430$ MPa)

tendency to cold crack formation (for example, the known phenomenon of «self-tempering» of martensite in a low-temperature range after phase restructuring is the factor of increase of crack resistance).

The low-temperature changes in martensite have the following peculiarities. Martensite, being tense and metastable structure, is characterized by a higher tendency to decay. The decay process is going towards the «elastic thermal equilibrium» in crystalline system as a result of redistribution of excessive carbon in interstitial spaces and its evolution to the zones of defects accumulation [21–25]. At room temperature the notable changes in the properties of martensite do not occur due to a low diffusive mobility of carbon. However, with increase in temperature the thermal activation of carbon diffusion (at 100 and 200 °C the diffusion carbon coefficient, as compared with the room temperature, increases accordingly by 3 and 6 orders [26]) leads to the first stage of tempering of hardened martensite with a considerable decrease in metal volume. In non-alloyed carbon steels the decay of martensite at the first stage of tempering is activated at 70–80 °C and finished at 170–200 °C, in the interval of 100–150 °C the process runs most intensively [21–23]. At this stage the carbon evolves from the solid solution, forming the laminated metastable ϵ -carbide of M_2C type, that is accompanied by decrease of lattice tetragonality [21]. As a result, the metal is partially weakened and acquires higher ductility than that in initial hardened state.

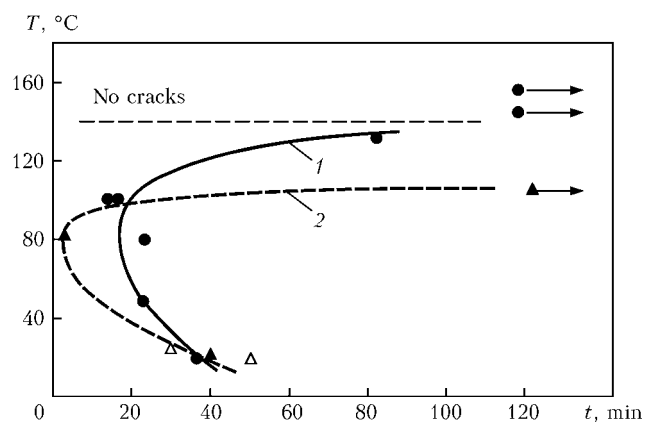


Figure 3. Thermal kinetic curves of a delayed fracture of welded joints: 1 — steel 25Kh2NMFA, $\sigma = 400$ MPa; 2 — 38KhN3MFA, $\sigma = 170$ MPa

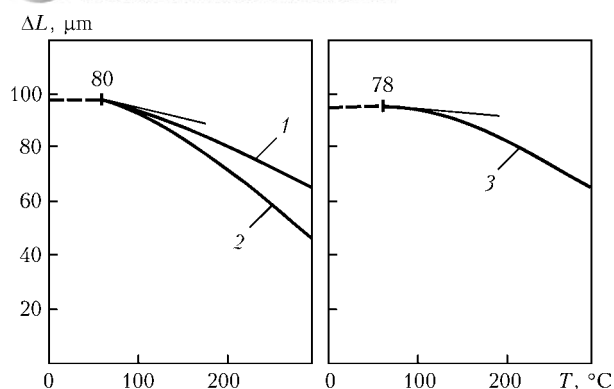


Figure 4. Dilatometric curves of tempering the martensite steels with 9% Cr: 1 – 10Kh9MFB; 2 – 40Kh9MFB; 3 – 25Kh2NMFA

Decay of martensite in the volume of metal has a gradual nature. The initial migration of carbon to microdefects, origination and growth of carbide in this zone take place due to the adjacent carbon, then the process is spread in the larger amount of elementary microvolumes. As a result, the areas of solid solution with decreased and initial high concentration of carbon are formed [21, 23]. The kinetics of process is defined by carbon mobility depending on temperature. Thus, according to data of work [20], the martensite half-decay duration in high-carbon steel at room temperature is 36 years, at 80 °C is 7 h 50 min, at 100 °C – 50 min, at 120 °C – 8 min, at 140 °C – 2.3 min, at 160 °C – 45 s. According to calculations, the activation energy of martensite decay in the range of considered temperatures is 108 kJ/mole.

Thus, in the process of martensite decay the heterogeneous structure is formed, consisting of initial rigid martensite matrix and microareas near the boundaries with lower degree of distortion of crystal-line lattice and lower resistance to a plastic shear. Hence, it follows that degree of decay development defines the character of distribution of microplastic shear deformations in the metal volume under the influence of external load or shrinkage stresses.

As is seen from the experimental data (see Figures 2 and 3) the interval of temperatures from the beginning of manifestation of tendency to crack formation to the decrease of crack resistance to minimum

(from 140 down to 100–80 °C) coincides with the range of the first stage of martensite decay. It is most probable that there exists the correlation between crack resistance of welded joints of alloyed steels and changes in the structure and strength of martensite which appear in the process of its low-temperature decay.

It was experimentally established that tempering phenomena followed by decrease of volume in the investigated steels with low carbon content (10Kh9MFB, 40Kh9MFB, 25Kh2NMFA, 38KhN3MFA) as well as in high-carbon steels begin to activate at the temperatures of about 80 °C (Figure 4). The obtained results confirm the possibility of effect of martensite decay in the range higher than 80 °C on the technological strength of welded joints of these steels.

The temperature influences the manifestation of hydrogen factor in different ways. At high temperature the ions of hydrogen diffuse easily along the voids of α -lattice, i.e. they perform «jumps» with a low activation energy, being about from 7 to 12.5–14.7 kJ/mole according to different estimations [3, 26–28], here no hydrogen brittleness appears. At the temperature below 200 °C the interaction of hydrogen with dislocations and grain boundaries is intensified [3, 26, 27]. Under these conditions the diffusion prevails at hydrogen overcoming energetic barriers (in the zone of traps binding hydrogen) at an activation energy of about 25–41 kJ/mole [26–28]. As the brittleness is caused by hydrogen, bound with dislocations, the delayed fracture propagation should be observed at temperatures below 200 °C. Moreover, following the data of works [27, 28] the sufficiently powerful trapping of dislocation hydrogen is occurred at the temperature below 120 °C.

To specify the possible mechanism of temperature effect on the variation of tendency to crack formation, the calculation of energy of activation of creep of welded specimens, recorded in the process of delayed fracture test, was made additionally. As far as during the test of several specimens under the same conditions the scatter in fracture duration and creep rate values was observed, the calculations gave averaged approximate values of E . Having compared the obtained E values with the approximate values of energy of activation of known processes, it is possible to reveal that thermally-activated internal process in metal which controls the development of experimentally studied phenomenon [13, 15].

In connection with the fact that the curves of change in duration and rate of fracture (Figure 5) at change of temperature for welded joints of martensite steel have a bend at 80–100 °C, that corresponds to the minimum of crack resistance, the separate determination of activation energy of creep within the temperature ranges above and below the bend area was performed: above 80–100 (high-temperature area) and below 80 °C (low-temperature area). The correspond-

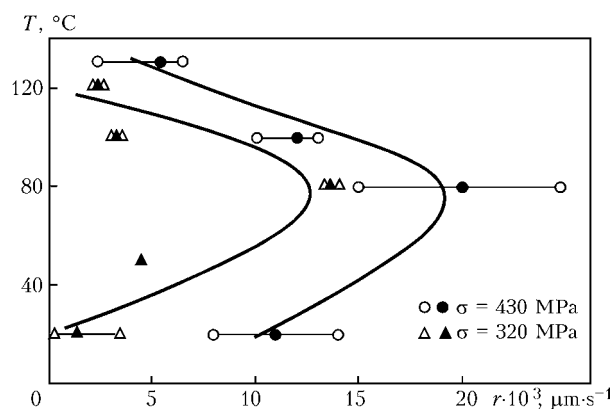


Figure 5. Correlation between the temperature and creep rate at a delayed fracture of welded joints of steel 10Kh9MFB: light and dark symbols – marginal (minimum, maximum) and average values of loading, respectively



ing rates were calculated according to the creep curves (see Figure 1), obtained experimentally.

During the tests of joints of martensite steel of the 10Kh9MFB type in high-temperature range (from 100 up to 120–140 °C) two types of creep were recorded: creep, not accompanied by fracture, which is typical of considerably low rate (about 10^{-4} – 10^{-3} $\mu\text{m/s}$) and gradual increase in rate with increase in temperature; average value of absolute energy of activation E is about 85–67 kJ/mole (at the range of values from 54 up to 150 kJ/mole); creep at delayed fracture with $E \approx 22$ –40 kJ/mole, the rate of which (about 10^{-2} – 10^{-3} $\mu\text{m/s}$) decreased with increase in temperature. The first type of creep (with $E \approx 85$ –87 kJ/mole) can be connected with partial weakening and facilitation of metal deformation due to the first stage of martensite decay propagation ($E = 108$ kJ/mole), which in its turn is controlled by carbon diffusion (for carbon diffusion in α -iron at lowered temperatures $E = 84$, at the temperatures up to 500 °C – 105 kJ/mole [26]). The second type of creep (with $E \approx 22$ –40 kJ/mole) is controlled by decohesive action of hydrogen entering the fracture zone at interaction with dislocations ($E \approx 25$ –41 kJ/mole) [26–28].

In low-temperature region only one type of creep was developed, connected with a delayed fracture. The calculated value of energy of activation ($E \approx 9$ –33 kJ/mole), the same as in previous case, is comparable with the energy of activation of hydrogen movement at interaction with dislocations. That is correlated with a determinative role of hydrogen in development of crack formation. The notable changes in martensite in low-temperature range do not occur. Therefore, one can suppose that high rigidity of metal and decrease in dislocations mobility at lowered temperatures lead to arresting the microplastic deformation, required for initiation and growth of a crack, and also for delay of diffusive hydrogen accumulation in pre-fracture zone. That is the possible reason of increase of delayed fracture period of welded joints of martensite steels with decrease in temperature.

The obtained results allow making the following assumptions regarding the factors determining the change in kinetics of delayed fracture of welded joints of martensite steels depending on temperature.

In the interval of tendency to cold crack formation (below 140–130 °C) the main destructive factor is hydrogen, interacting with traps (dislocations). At the temperature above 80–100 °C the thermally-activated process, similar to the first stage of martensite tempering, has an additional influence on the character of delayed fracture development. At this stage, as shown above, the decay of martensite is proceeding gradually as a result carbon movement from the crystalline lattice to the adjacent defects of crystalline structure and to the boundaries [29]. The areas of martensite which partially lost their carbon are weakened and become more prone to microplastic deformation than surrounding solid solution with initial carb-

on content. At temperatures near the beginning of decay activation (80–100 °C) the diffusive movement of carbon is relatively slow. One can suppose that gradually developed decay and, as a consequence, the heterogeneous weakening of martensite, create conditions for passing the local microplastic deformations in the zone of grain boundaries and rapid formation of cracks during hydrogen embrittlement. Moreover, for initial stage of decay the development of heterogeneous carbon distribution (formation of clusters in the form of zones of Guinier–Preston) and origination of submicroscopic carbides in the crystalline defects are characteristic [29]. The accumulation of carbon and precipitating phases create microzones with local increased stresses (effect of dispersion hardening) [29]. Microstructural heterogeneity and solidification of matrix can also contribute to proceeding of local microshear processes in less strong grain boundary microzones and development of intergranular fracture [30]. The minimum of crack resistance in the range 80–100 °C (Figure 6) can be, probably, connected with the development of such phenomena. At the higher temperature the thermal activation of diffusion of carbon promotes the rapid spreading of martensite decay. It is obvious that under these conditions the increase in sizes of areas of partially tempered martensite, prone to deformation, leads to distribution of plastic deformations in large volumes. It results in decrease of probability of a rapid local clustering of dislocations and hydrogen up to the critical level and the delayed fracture propagation is arrested. One can logically suppose that the absence of tendency to crack formation at the temperatures above 140 °C is the reason of a rapid volumetric martensite decay, weak binding of hydrogen with dislocations, and also partial evolution of diffusive hydrogen from the welded joint. At lowered temperatures (below 80 °C) only delayed fracture development is caused by hydrogen. With the decrease in temperature the duration of fracture in this range is increased, which can be due to relaxation of thermal activation of dislocations mobility and hydrogen movement in a rigid martensite.

In the joints of bainite steel (Figure 7, welding using electrodes TML-3U) the minimum of crack resistance is shifted to the region of room temperature

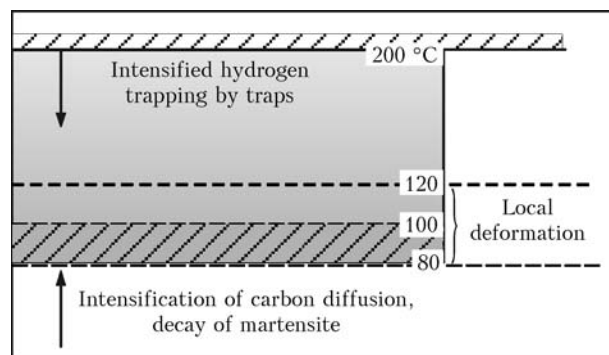


Figure 6. Correlation between the temperature and factors regulating the development of a delayed fracture of welded joints of martensite steels (hatched area – temperature area of minimum crack resistance)

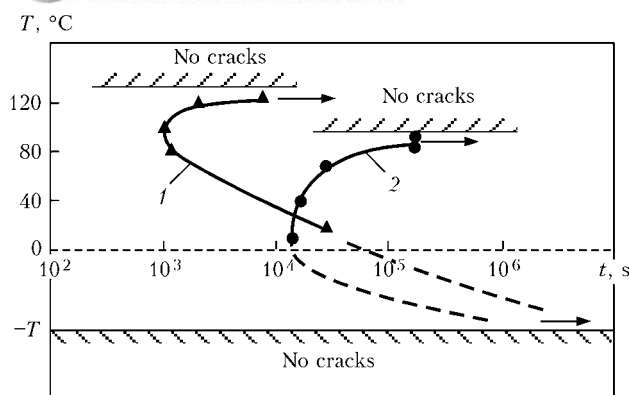


Figure 7. Generalized thermal kinetic curves of a delayed fracture of welded joints of martensite steel 10Kh9MFB (1) and bainite steel 10GN2MFA (2) at $\sigma = 320$ MPa

(no experiments were carried out at lower temperatures). With the increase in temperature of tests the crack resistance increases. It is obvious that in this case the changes in crack resistance can be determined by the following factors. Usually under the conditions of cooling in the manual arc welding the joints acquire not the purely bainite, but martensite-bainite structure with a predominant fraction of martensite. This metal is characterized by heterogeneity of level of hardening of different phases, caused by a non-uniform carbon distribution at the stage of intermediate transformation. As a result, the initial structure has, alongside with the strong and hard-to-deform areas, the microareas with a lower strength and larger tendency to shear deformation. In the process of tests at increased temperatures the decay of martensite component is possible in such metal (similarly with the first stage of martensite decay). This contributes to the general increase in ductility and increase in resistance against a delayed fracture. For example, during testing at temperature 70–80 °C using sensors of micromovement the shortening of specimen was observed, that could be a consequence of hardening structure decay. Here, the spreading volumetric weakening is obviously a factor of crack resistance improvement. At lowered temperatures the structural changes (in time scales of carried out tests) do not take place. The preserved high rigidity and structural heterogeneity of martensite-bainite metal, and also some thermal activation relaxation of dislocations mobility could create the conditions for development of local deformations in less strong microareas. Probably, due to this the time of delayed fracture development was decreased with the decrease in temperature. In this series of experiments the energy of activation of fracture as a result of hydrogen embrittlement was about 22 kJ/mole.

With the decrease in temperature in the negative area both the movement of dislocations and also hydrogen diffusion are arrested, and at the certain temperature $-T$, the delayed fracture becomes impossible [15, 28, 31, 32]. For example, A.M. Makara showed that crack formation is interrupted at -70 °C [32], according to data of work [28] the hydrogen brittleness in steel Fe–5Cr was not possible at the tempera-

ture below $-60 - -100$ °C. With account for the obtained experimental data and mentioned influence of negative temperatures on the hydrogen brittleness the generalized temperature dependence of crack resistance in the temperature–time coordinates of delayed fracture acquires a form of C-like curves (see Figure 7).

It follows from the obtained results that during the control of heat modes of welding it is necessary to take into account the thermal kinetic peculiarities of crack formation. For example, in case of martensite steels it is reasonable to provide the decrease in cooling rate of a joint in the interval of high resistance against a delayed fracture (not lower than 140 °C). The result of application of such procedure is partial (and rapid enough) volumetric weakening of martensite, and also evolution of diffusive hydrogen from the joint. The cooling rate of welded joint should not exceed the rate of spreading the decay of martensite solid solution. In case of rapid temperature drop the joint metal can appear to be in the state of beginning of formation of structural heterogeneity (at temperatures close to 100–80 °C), which has a risk of quick development of cracks formation. The rational procedure to increase the cracks resistance is a low-temperature relaxation after the completion of welding [33], which also should be performed in the range of high resistance against crack formation.

Thus, it is shown that in the range of temperatures of carried out tests of welded joints of hardening steels (from 140 °C down to room temperatures) the crack formation was connected with destructive (embrittled) action of hydrogen. It was assumed that determinant effect on change in kinetics of crack formation is the character of distribution of microplastic deformations initiating the development of a delayed fracture. With the growth of level of localization of microshear processes in rigid hardened metal the probability of a rapid arising of critical state (critical density of dislocations and hydrogen concentration) required for initiation and propagation of a crack should grow. It is shown that change of crack resistance under the influence of temperature can be correlated with the character of spreading of a low-temperature martensite decay, determining the rigidity level of metal and peculiarities of formation of weakened (prone to deformation) microareas. It was established that in the investigated low-carbon alloyed steels the decay of martensite, similar to the known low-temperature martensite decay in carbon steels, is spread at the temperatures above 80 °C. Microstructural heterogeneity occurred in joints of martensite steels at the temperatures in the area of beginning of activation of decay (80–100 °C), can be a reason of development of local microshear deformations in the zone of grain boundaries, that leads to a rapid development of a delayed fracture and defines the minimum of crack resistance. The revealed arresting of fracture at higher temperatures can be connected with a rapid spreading of weakening, distribution of microdeformations in



large volumes, and also with the decrease in energy of hydrogen binding with dislocations and partial hydrogen evolution from the fracture zone. In the range below 80 °C the crack formation in the joints of martensite steels with decrease in temperature is also delayed. It can appear to be a consequence of growth of resistance of rigid martensite matrix to the propagation of microplastic deformation, weakening of diffusive mobility of hydrogen and resulting delay of formation of microzones with a critical density of dislocations and hydrogen. In contrast to martensite metal the welded joints of bainite steels acquire the heterogeneous martensite-bainite structure during welding. For such a metal, as is known, the heterogeneity by the mechanical properties is typical, connected with the presence of different microstructural components. The decrease in period of a delayed fracture of bainite steel joints at the decrease in temperature below 80–70 °C is obviously connected with increase in level of localization of microshear deformations in less strong microareas and, as a consequence, a quick initiation and growth of cracks. One can also suppose that high resistance of bainite steel welded joints against cold crack formation at the temperature 70–80 °C or higher is predetermined by increase in metal ductility as a result of a low-temperature decay of hardening structure and partial evolution of diffusive hydrogen from the joint. It is advisable to take into account the considered regularities of changes in crack resistance of welded joints of alloyed low-carbon steels in the selection of rational thermal modes (preheat temperatures, postweld isothermic holding modes) in welding of steels with similar alloying systems.

1. Shorshorov, M.Kh., Chernyshova, T.A., Krasovsky, A.I. (1972) *Weldability testing of metals*. Moscow: Metallurgiya.
2. Hrivnak, I. (1984) *Weldability of steels*. Moscow: Mashinostroenie.
3. Karpenko, G.V., Kripyakevich, R.I. (1962) *Hydrogen effect on steel properties*. Moscow: Metallurgiya.
4. Makarov, E.L. (1977) Nature of fracture in cold crack formation in high-strength hardenable steels during welding. In: *Advanced technology of structural materials*: Transact. of N.E. Baumann MVTU, 248, Issue 3.
5. Sarraf, V.I., Filippov, G.A. (1981) Effect of admixtures on brittleness of steel after hardening. *Fiz.-Khimich. Mekhanika Materialov*, 2, 96–101.
6. Kolachev, B.A. (1985) *Hydrogen brittleness of metals*. Moscow: Metallurgiya.
7. Makara, A.M., Mosendz, N.A. (1971) *Welding of high-strength steels*. Kiev: Tekhnika.
8. Suzuki, H. (1978) Cold cracking and its prevention in steel welding. *IIW Doc. IX-1074-78*.
9. Pidgaetsky, V.V. (1970) *Pores, inclusions and cracks in welds*. Kyiv: Tekhnika.
10. Terasaki, T., Hall, G.T., Parteger, R.I. (1991) Cooling time and prediction equation for estimating hydrogen diffusion in CTS test welds. *Transact. of JWS*, 22(1), 53–56.
11. Skulsky, V.Yu. (2009) Thermokinetic peculiarities of formation of cold cracks in welded joints on hardening heat-resistant steels. *The Paton Welding J.*, 3, 8–11.
12. Kasatkin, B.S., Brednev, V.I., Volkov, V.V. (1981) Procedure for determination of deformations in delayed fracture. *Avtomatich. Svarka*, 11, 1–7, 11.
13. Brednev, V.I., Kasatkin, B.S. (1988) Specific work of formation of cold crack sites in welding of low-alloy high-strength steels. *Ibid.*, 11, 3–8, 11.
14. Garofalo, F. (1968) *Principles of creep and long-term strength*. Moscow: Metallurgiya.
15. Honeycomb, R. (1972) *Plastic deformation of metals*. Moscow: Mir.
16. Kasatkin, O.G. (1994) Specifics of hydrogen embrittlement of high-strength steels in welding. *Avtomatich. Svarka*, 1, 3–7.
17. Kasatkin, B.S., Smiyan, O.D., Mikhajlov, V.E. et al. (1986) Hydrogen effect on susceptibility to crack formation in HAZ with stress raiser. *Ibid.*, 11, 20–23.
18. Pokhodnya, I.K., Yavdoshchin, I.R., Paltsevich, A.P. et al. (2004) *Arc welding metallurgy. Interaction of metal with gases*. Kiev: Naukova Dumka.
19. Boniszewski, T., Watkinson, F., Baker, R.G. et al. (1965) Hydrogen embrittlement and heat-affected zone cracking in low-carbon alloy steels with acicular microstructures. *British Welding J.*, 12(1), 20–42.
20. Kikuta, Y., Araki, T. (1980) Microscopic redistribution behaviors of hydrogen and fracture morphology of HAZ cold cracking in high-strength steel. *IIW Doc. II-927-80*.
21. Gulyaev, A.P. (1978) *Metals science*. Moscow: Metallurgiya.
22. Kurdymov, G.V., Utevsky, L.M., Entin, R.I. (1977) *Transformations in iron and steel*. Moscow: Nauka.
23. Lysak, L.I., Nikolin, B.I. (1975) *Physical bases of heat treatment of steel*. Kiev: Tekhnika.
24. Kehoe, M., Kelly, P.M. (1970) The role of carbon in the strength of ferrous materials. *Scripta Metallurgica*, 4(6), 473–467.
25. Novikov, V.M. (1986) *Theory of heat treatment of metals*. Moscow: Metallurgiya.
26. Fast, J.D. (1975) *Interaction of metals with gases. Kinetics and reaction mechanism*. Vol. 2. Moscow: Metallurgiya.
27. Choo, W.Y., Lee Young Jai (1982) Thermal analysis of trapped hydrogen in pure iron. *Metal. Transact. A*, 13(1), 135–140.
28. Moroz, L.S., Chechulin, B.B. (1967) *Hydrogen brittleness of metals*. Moscow: Metallurgiya.
29. Goudremont, E. (1951) *Special steels*. Vol. 1. Moscow: Metallurgizdat.
30. Zemzin, V.N., Shron, R.Z. (1978) *Heat treatment and properties of welded joints*. Leningrad: Mashinostroenie.
31. Macklintok, F., Argon, A. (1970) *Deformation and fracture of materials*. Moscow: Mir.
32. Makara, A.M. (1960) Study of cold crack nature in welding of hardening steels. *Avtomatich. Svarka*, 2, 9–33.
33. Kozlov, R.A. (1986) *Welding of heat-resistant steels*. Leningrad: Mashinostroenie.



INFLUENCE OF THERMAL CYCLES OF WELDING AND EXTERNAL LOADING ON STRUCTURAL-PHASE VARIATIONS AND PROPERTIES OF JOINTS OF 17Kh2M STEEL

L.I. MARKASHOVA, G.M. GRIGORENKO, V.D. POZNYAKOV, E.N. BERDNIKOVA and T.A. ALEKSEENKO
E.O. Paton Electric Welding Institute, NASU, Kiev, Ukraine

Structural-phase transformations in samples of high-strength low-alloy steel 17Kh2M were studied at different cooling rates simulating different processes of their welding and subsequent deformation at increment of external load. Analytical evaluation of the specific contribution of structures formed in the welding zone to mechanical property values, as well as magnitude and distribution of strains, residual inner stresses and their gradients localized along the boundaries of structural-phase components was performed.

Keywords: *high-strength steel, welding simulation, structural-phase parameters, strengthening, mechanical properties, property prediction, strain localizing, local inner stresses, theoretical strength*

The most significant characteristics of high-strength steels and their welded joints are high yield limit, low temperature of brittle transition, good weldability, providing a welded joint reliable in operation [1–7]. A number of criteria for weldability evaluation have also been developed, such as equivalent carbon content C_{eq} [8], probable cracking parameter [9], maximum HAZ metal hardness [10], relative index of the cooling rate [11], etc., allowing mainly for the composition of steel, influence of alloying on maximum hardness in the HAZ metal, intensity of the general stressed state and a number of other factors (phase transformation kinetics at austenite cooling, variation of element diffusion rate in a wide temperature interval, role of forming structures, cooling modes) [5–7]. Unfortunately, the proposed criteria did not yield any reliable results on evaluation of the conditions of producing sound (in terms of strength and crack resistance properties) welded joints even for limited welding conditions [11, 12], while the calculated values, for instance HV_m [13], are close to the actual ones only in some cases.

Further on, at evaluation of the cracking criterion, considered in [9], noticeable deviations in the proposed dependencies [14] for steels with a wider alloying range [15] were taken into account. In analysis of numerous experimental data and analytical dependencies attention was also given to the role of structural factors in formation of properties and service characteristics of high-strength steel joints [16, 17]. On the other hand, the diversity of the mechanisms of austenite transformation at cooling in the HAZ metal in a broad temperature interval, complexity of the influence of alloying, technological modes of welding and a number of other factors of evaluation by the proposed equations without objective experimental in-

formation on the real structural states of the metal, particularly, in problem zones of welded joints, do not provide a sufficient accuracy. This circumstance confirms the need to expand the experimental investigations (in particular at different structural levels) of these processes.

This work gives some results of investigations in this direction: features of structural changes in the welded joint metal at characteristic thermodeformational conditions of welding; role of each of the structural parameters (phase components, grain, subgrain and dislocation structure, composition, phase precipitates, etc.) in variation of mechanical properties in different joint zones; structural conditions, mechanisms of increase of local inner stresses and damageability in welded joints under the impact of technological parameters of welding and external loading; establishing the conditions and mechanisms of stress relaxation (plastic relaxation, or relaxation by cracking with brittle fracture), as well as structural parameters, having a certain role in the processes of increase of internal stresses and their relaxation mechanisms.

Materials and experimental procedures. The first stage of the work was performed on samples of high-strength low-alloyed 17Kh2M steel of the following composition, wt. %: 0.17C; 1.55Cr; 0.3Mo; 0.11Ni; 0.6Mn; 0.2Si; 0.006S; 0.014P, at cooling rates $w_{6/5} = 2.5$ and 20°C/s . Investigations were performed on samples directly after heat treatment by the thermodeformational cycle of welding (TCW) and their subsequent deformation by stretching at a varying external load P_{ex} approximately from $0.7\sigma_{0.2}$ up to $0.8\sigma_t$. Samples of 13×13 mm cross-section and 150 mm length were heated by passing current ($v_{heat} = 150^\circ\text{C/s}$) up to the temperature of $1250\text{--}1300^\circ\text{C}$, and then were cooled by a preset program at different rates.

Structural-phase and concentration changes, nature of distribution and density of crystalline lattice



defects in the weld metal and different sections of the HAZ metal were studied using optical metallography, analytical scanning electron microscopy (SEM-515, Philips, Holland) and microdiffraction transmission electron microscopy (JEM-200CX, Jeol, Japan). Comprehensive studies provided experimental information on different structural levels — from macro(grain) to micro(dislocation), thus allowing evaluation of differentiated contribution of individual structural-phase components and other structural parameters to the change of the overall (integral) value of strength characteristics $\sigma_{0.2}$, σ_t , as well as distribution of localized strain ϵ_l and local inner stresses τ_{in} in different zones of welded joints.

Experimental results. The following structural parameters were studied: type of phase constituents (upper bainite B_{up} , lower bainite B_l , martensite M); grain size D_{gr} , volume fraction of phases V_{fr} formed in different sections of the HAZ metal, as well as the corresponding changes of HV microhardness for conditions with minimum cooling rate $w_{6/5} = 2.5^\circ C/s$. It is established that the structure in zone I of HAZ metal (coarse-grain — overheated zone, Figures 1, *b* and 2, *a*) is represented by grains of upper and lower bainite (B_{up} , B_l) at $D_{B_l} = 45\text{--}108\ \mu m$; $V_{fr}(B_{up}) \sim 58\%$; $HV_{B_l} = 2500\text{--}2700\ MPa$ for B_{up} and $D_{B_{up}} = 22\text{--}80\ \mu m$; $V_{fr}(B_{up}) \sim 25\%$; $HV_{B_l} = 3000\text{--}3400\ MPa$ for B_l with ferrite fringes (FF) of $6\text{--}7\ \mu m$ thickness. Normalized section (zone II, Figures 1, *b* and 2, *b*) is characterized by a structural change with increase of volume fraction of the ferrite-pearlite component, including FF thick-

ness, abrupt grain refinement (2 times) at a slight variation of microhardness of the structural elements. Incomplete recrystallization section (zone III, Figures 1, *b* and 2, *c*) is characterized by a fine-grained structure ($D_{gr} = 15\text{--}30\ \mu m$) at volume fraction of ferrite $V_{fr}(F) = 40\%$. HAZ zone IV is characterized predominantly by ferrite-pearlite fine-grained structure ($D_{gr} = 10\ \mu m$) at almost equal fractions of ferrite and pearlite, microhardness for pearlite and ferrite being $HV\ 2450\text{--}2600$ and $HV\ 1800\text{--}1900\ MPa$, respectively (see Figure 1, *a*).

Transmission microscopy examination of the fine structure was used to consider factors, which are the most significant from the view point of ductility and crack resistance, namely change of dislocation density and distribution in different structural elements (in the internal volumes and along the boundaries) and nature of substructure formation in the internal volumes of the subgrains. As regards the dislocation structure, the following should be noted: a low volume density of dislocations ($\rho \sim (2\text{--}4) \cdot 10^{10}\ cm^{-2}$) at their uniform distribution is observed along all the HAZ sections (from I to IV). The lowest values of volume fraction of dislocations are characteristic for HAZ zone I, although the substructure in this zone is not sufficiently clear — subboundaries are broad, blurred with low disorientation angles (θ of up to 5°), which is indicative of running of the initial stages of substructure formation in the overheated zone — the coarse grain (Figure 3, *a-c*). Distribution of dislocations in the near-boundary zones is somewhat different: characteristically, extended dislocation clusters

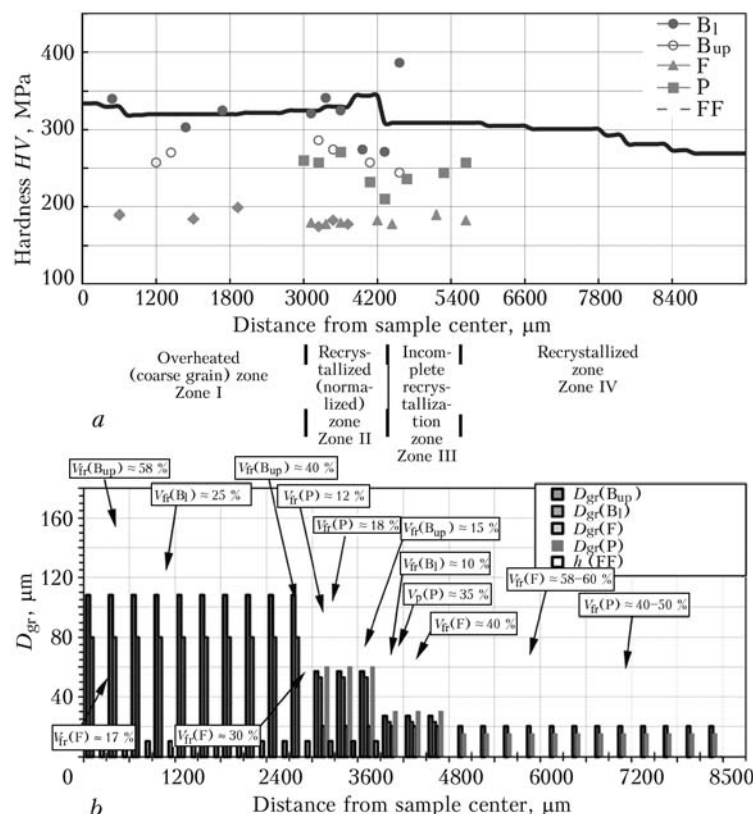


Figure 1. Structural parameters of 17Kh2M steel in all the sections of the HAZ metal at $w_{6/5} = 2.5^\circ C/s$: *a* — HAZ metal microhardness; *b* — size of structural-phase components

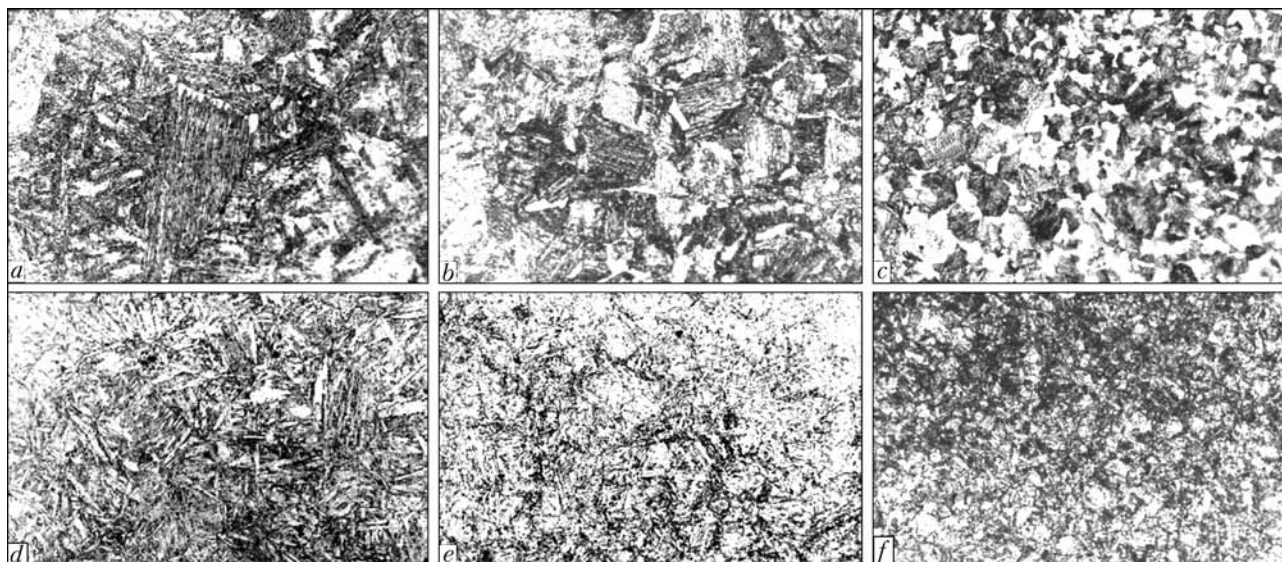


Figure 2. Microstructure ($\times 320$) of HAZ metal (17Kh2M steel, welding simulation) at different cooling rates $w_{6/5} = 2.5$ (a–c) and 20 (d–f) °C/s; a, d – overheated zone; b, e – normalized zone; c, f – incomplete recrystallization zone

of a high density ($\rho \sim (8-9) \cdot 10^{10} \text{ cm}^{-2}$) form along the intergranular boundaries (predominantly along the upper bainite boundaries), thus creating a high gradient of dislocation density (from $(1-3) \cdot 10^{10}$ up to $9 \cdot 10^{10} \text{ cm}^{-2}$) in such structural elements (Figure 3, a, b).

At increase of cooling rate ($w_{6/5} = 20 \text{ °C/s}$) the following structural changes are observed (Figures 2, d–f and 3, d–f). At the general considerable refinement of the structure (by approximately 1.2–1.7 times), particularly in the overheated (zone I) and recrystallized (zone IV) zones, and increase of microhardness (HV) by 10 % on average, phase composition of the metal structural constituents changes in all the HAZ zones, volume fraction of lower bainite increases significantly (approximately 2–3 times) at reduction of the upper bainite fraction (approximately 4–6 times); purely ferrite constituent is practically completely absent and martensite structure forms (with microhardness $HV \sim 4200-4700 \text{ MPa}$), the volume fraction of which varies in a comparatively uniform fashion from 30 up to 17 % (at transition from zone I to IV in the HAZ). Under the conditions with minimum cooling rate $w_{6/5} = 2.5 \text{ °C/s}$ the martensite component is practically absent.

For the fine metal structure (dislocation density, nature of their distribution, dimensions and features of structural elements) in the HAZ metal the following should be noted at increase of the cooling rate.

Against the background of the increase of the bulk (intragranular) dislocation density, also the non-uniformity of their distribution is increased. Dislocation density is somewhat higher on the boundaries of B_{up} packs, laths, particularly, in the area of location of carbide precipitates along B_{up} laths, where it reaches approximately $(1.0-1.2) \cdot 10^{11} \text{ cm}^{-2}$. Against the background of total increase of dislocation density, however, the gradient between the bulk and grain-bound-

ary dislocation density for the conditions with high-rate cooling is significantly decreased, i.e. $\Delta\rho_{w_2} < \Delta\rho_{w_1}$ (see Figure 3, d, e).

Thus, in samples of 17Kh2M steel after simulation of the welding process, a change of primarily the HAZ metal phase composition (from bainite-ferrite at $w_{6/5} = 2.5 \text{ °C/s}$ to bainite-martensite structure at $w_{6/5} = 20 \text{ °C/s}$) occurs in the most sensitive HAZ zone (particularly in I) at transition from the minimum to the maximum cooling rate, which is accompanied by an increase of the volume fraction of lower bainite as a result of reduction of upper bainite and microhardness increase in all the HAZ zones. In addition, a general refinement of the structure and substructure, and increase of dislocation density at simultaneous reduction of their gradients along the boundaries take place.

Experimental data base (optical, analytical scanning, transmission electron microscopy) allowed evaluation of the contribution of each of the structural parameters to change of the strength ($\sigma_{0.2}$, Figure 4) and ductility (K_{1c} , Figure 5) properties. It was assumed that the total (integral) value of $\sigma_{0.2}$, according to Archard's dependence [18], is the summary value, consisting of a number of components, namely: σ_0 – resistance of metal lattice to free dislocation motion (lattice friction stress or Peierls–Nabarro stress) [19]; $\Delta\sigma_{s.s}$ – solid solution strengthening by alloying elements and impurities (solid solution strengthening) [20]; $\Delta\sigma_{gr}$, $\Delta\sigma_s$ – strengthening due to a change of grain and subgrain size, according to Hall–Petch dependence (grain-boundary and substructural strengthening) [18, 21–23]; $\Delta\sigma_p$ – strengthening due to pearlite [20]; $\Delta\sigma_d$ – dislocation strengthening due to interdislocation interaction [24, 25]; $\Delta\sigma_{d.s}$ – strengthening due to dispersed particles by Orowan (dispersion strengthening) [26, 27].

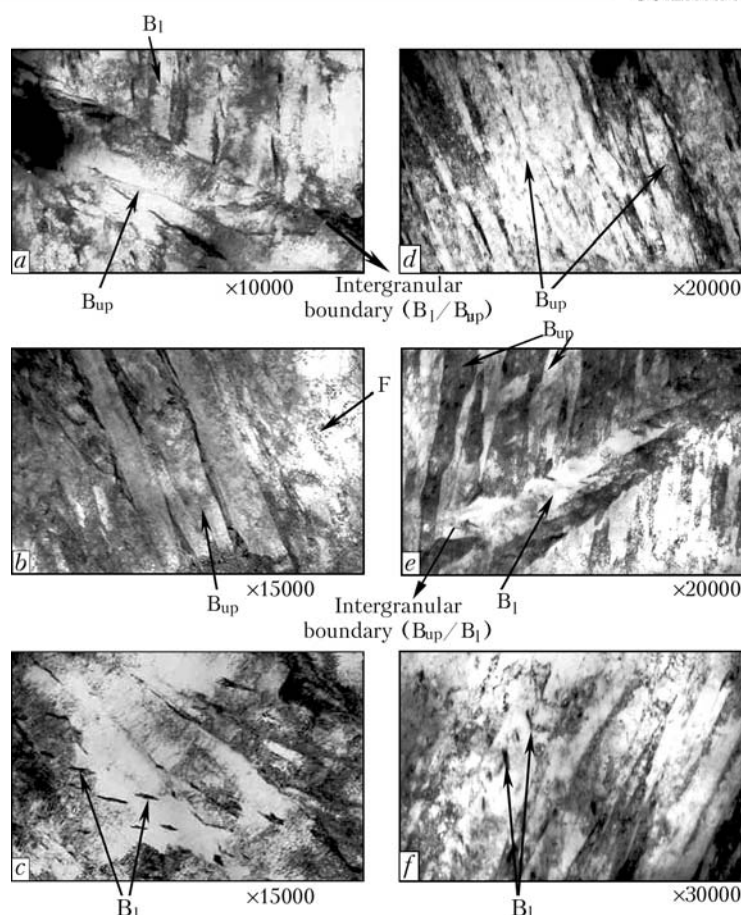


Figure 3. Fine microstructure of 17Kh2M steel (welding simulation) in the incomplete recrystallization zone at cooling rates $w_{6/5} = 2.5$ (a–c) and 20 (d–f) °C/s (characteristics structures B_{up} , B_l , F and their contact boundaries are marked by arrows)

Comparison of the change of mechanical (strength) properties across the HAZ (at analytical evaluation of the composition of various structural parameters, see Figure 4, a, c) shows that the total level of $\sigma_{0.2}$ (Figure 4, d) in all the zones of the HAZ increases by approximately 30 % at increase of the cooling rate, which is related to the increase mainly of the contribution of subgrain ($\Delta\sigma_s$) strengthening in B_l structures ($\Delta\sigma_s \sim 240\text{--}280$ MPa). The grain structure makes a minimum contribution to strengthening ($\Delta\sigma_{gr} \sim 80$ MPa), contribution of dislocation structure to $\sigma_{0.2}$ only slightly exceeds this value ($\Delta\sigma_d \sim 100\text{--}110$ MPa, which is less than 10 % of the total level of $\sigma_{0.2}$). Grain strengthening ($\Delta\sigma_{gr} \sim 180$ MPa) prevails in HAZ zone IV.

Thus, experimental-analytical study points to an increasing influence of the structure (particularly, B_l) on improvement of the strength properties in the HAZ of high-strength steel 17Kh2M, particularly with increase of the cooling rate during welding.

Since evaluation of mechanical properties by forming structures allows revealing the structural parameters influencing the lowering or increase of the properties of welded joint metal, application of the accepted approach enables forecasting the mechanical properties of the joints, depending on the structural state of the materials being welded [28–30].

An example of such a prediction for high-strength steels by the most significant structural parameters is given in Figure 6. From the Figure one can see how $\sigma_{0.2}$ can change for steel, depending on the size of grain D_{gr} , subgrain d_s , dislocation density ρ , dimensions and effective distance between the particles of phase precipitates λ_p , and content of the pearlite component P. The greatest contribution to increment of $\sigma_{0.2}$ ($\Delta\sigma_{0.2}$) is made by particles of phase precipitates, refinement of grain and subgrain. Maximum values of $\Delta\sigma_{0.2}$ increment (more than 100 MPa) can be achieved by grain refinement to 10 μm and less, and subgrain refinement to about 1 μm . As regards dispersion strengthening, the greatest effect is yielded by dispersed particles of up to 1 μm , namely particles of about 0.1 μm and less.

The second stage of structural-analytical examination of the structure influence on the properties of high-strength steel joints is related to analysis of the pattern of the zone of distribution and localizing of strain ϵ_l , as well as internal stresses $\tau_{in/1}$ – internal stress raisers for evaluation of the level of these stresses relative to theoretical strength of the material. In addition, dynamics of ϵ_l , $\tau_{in/1}$ variation was analyzed, depending on the conditions of welded joint cooling and subsequent external force impact on the HAZ metal, P_{ex} . The defined problem is of key importance,

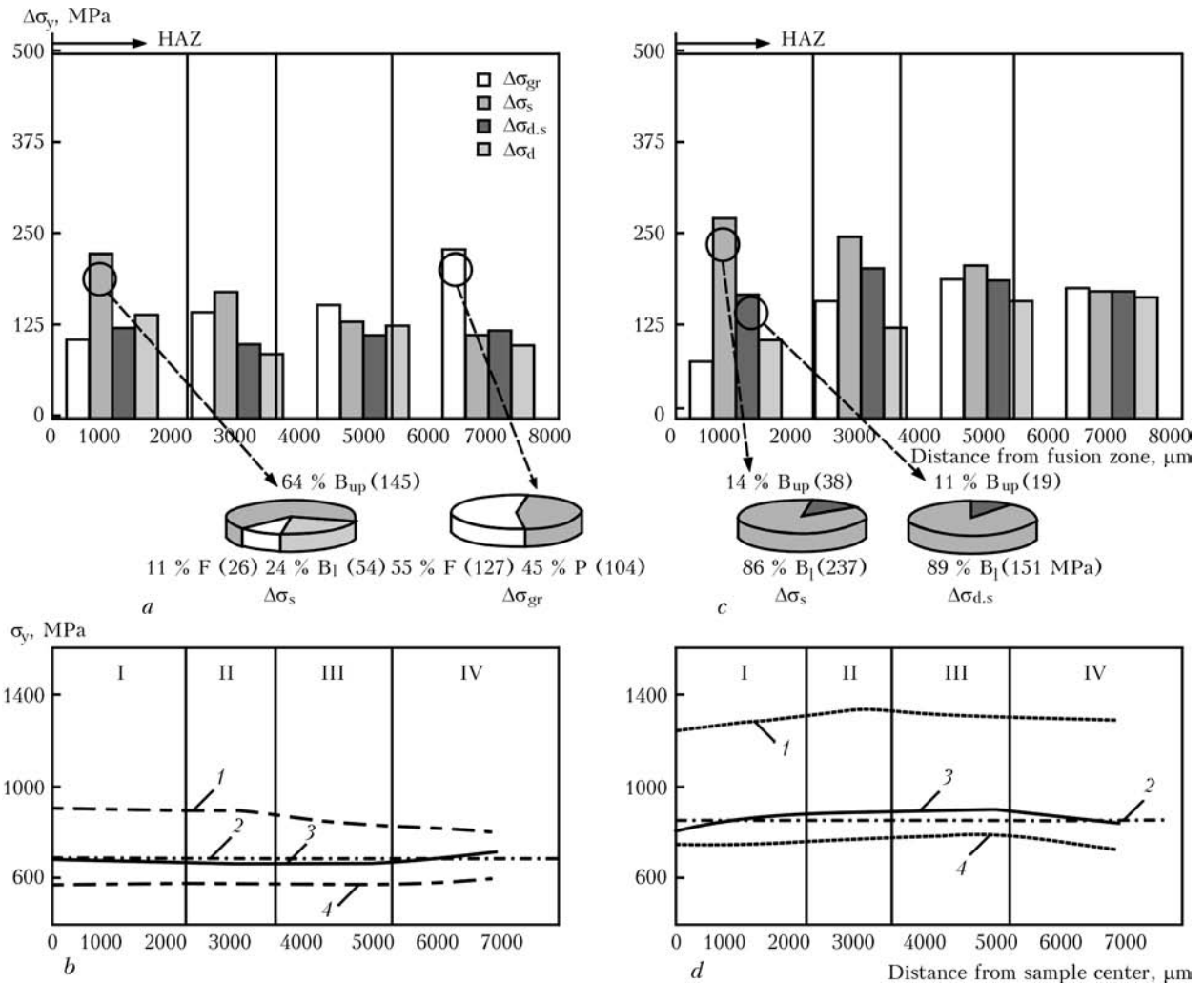


Figure 4. Histograms and sector diagrams (*a, c*) reflecting the differentiated contribution of individual structural parameters (size of grain, subgrain, dislocation density, phase precipitates) into increment of the yield point $\Delta\sigma_y$ and total (integral) σ_y variation in all the HAZ zones for minimum ($w_{6/5} = 2.5$ °C/s – *a, b*) and maximum ($w_{6/5} = 20$ °C/s – *c, d*) cooling rates: 1 – $\sigma_{y \max}$; 2 – $\sigma_{0.2 \text{ test}}$; 3 – $\sigma_{y \text{ calc}}$; 4 – $\sigma_{y \text{ min}}$

as the processes of delayed fracture and crack resistance are directly related to formation of internal stress raisers, i.e. crack initiation and propagation sites [31]. Such a problem is solved allowing for the actual patterns of distribution and evaluation of dislocation density in structures of different types.

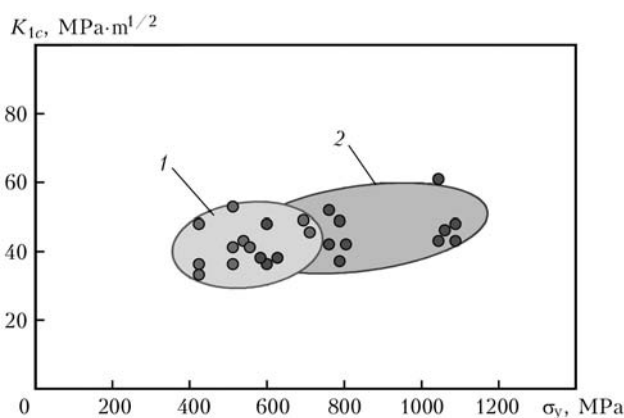


Figure 5. Probabilistic change of K_{Ic} value in 17Kh2M steel heat-treated to TCW (zone I) as a result of the external force impact on the metal: 1 – $w_{6/5} = 2.5$; 2 – 20 °C/s

Changes in internal stress $\tau_{in/l}$, gradients of these stresses $\Delta\tau_{in/l}$, level of localized strain ϵ_l , depending on the type of forming structures, were assessed by the known dependencies for τ_{in} [32]:

$$\tau_{in} = Gbh\rho/\pi(1 - \nu),$$

where G is the shear modulus; b is the Burgers vector; h is the foil thickness ($2 \cdot 10^{-5}$ cm); ν is the Poisson's ratio.

Localized strain ϵ_l was determined from Conrad dependence [33]

$$\epsilon_l = \alpha_1 \rho b S,$$

where α_1 is the coefficient correlating the tensile strain with shear strain, equal to 1.4; S is the average distance of dislocation displacement during loading, which practically corresponds to substructure parameters [34].

Experimental data on the nature of distribution of dislocations, their density in dislocation clusters, as well as obtained on their basis calculated values of the level of internal stresses localized in this zone

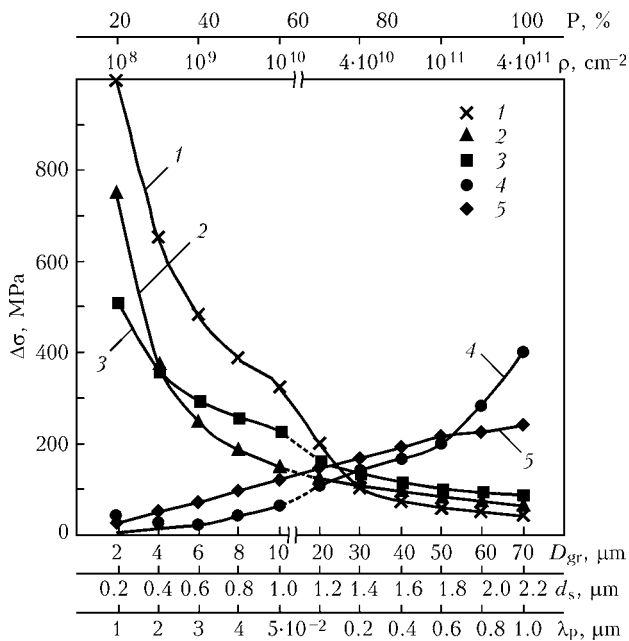


Figure 6. Variation of yield point $\sigma_{0.2}$ of 17Kh2M steel heat-treated to TCW depending on the structural-phase parameters: 1 – dispersed; 2 – subgrain; 3 – grain boundary; 4 – dislocation; 5 – pearlite strengthening

correlated with the structures (lower and upper bainite, ferrite, martensite, etc.), forming in the metal of welded joint HAZ, are given in Figure 7.

So, the following was established for upper and lower bainite structures (as structural components the most characteristic for steel). The most dense and extended ($\sim 1.2\text{--}3.0\text{ }\mu\text{m}$) dislocation clusters with a high dislocation density ($\rho \sim (8\text{--}9) \cdot 10^{10}\text{ cm}^{-2}$) form predominantly along the continuous cementite plates directed along the upper bainite boundaries. As a result, stress raisers in structures of such a type form predominantly along the grain boundaries, and values of stresses τ_{in} and strains ϵ_l localized along grain boundaries are of the order of $\tau_{in} = 1500\text{--}1700\text{ MPa}$, which corresponds to approximately $0.2\tau_{theor}$ (values of theoretical strength) and ϵ_l of up to 40 % (see Figure 3, *a*). Contrarily, dislocation clusters in lower bainite structures feature a much shorter extent ($l \sim 0.4\text{--}0.7\text{ }\mu\text{m}$), are distributed across the inner volume of bainite laths (in keeping with carbide distribution in the structure), and, in addition, dislocation density in such clusters is essentially decreased (to $\rho \sim (2\text{--}4) \cdot 10^{10}\text{ cm}^{-2}$), thus promoting not only dispersal, but also lowering of both the level of internal stresses in the zones of their localizing to $\tau_{in} = 370\text{--}740\text{ MPa}$ ($\sim (0.04\text{--}0.09)\tau_{theor}$), and of localized strain $\epsilon_l \sim 10\text{--}20\text{ }\%$ (see Figure 3, *c*).

In addition, it should be noted that the highest values of local internal stresses τ_{in} , their gradients $\Delta\tau_{in}$ and regions of localizing of strain ϵ_l are observed, as a rule, in the zone of contact of coarse-grained phase constituents, essentially differing by their physical characteristics, for instance, upper bainite/ferrite ($\Delta\tau_{B_{up}/F} = 1600\text{ MPa}$; $\epsilon_l \sim 40\text{ }\%$), etc. (Figure 7, *a*). The most uniform distribution and comparatively uni-

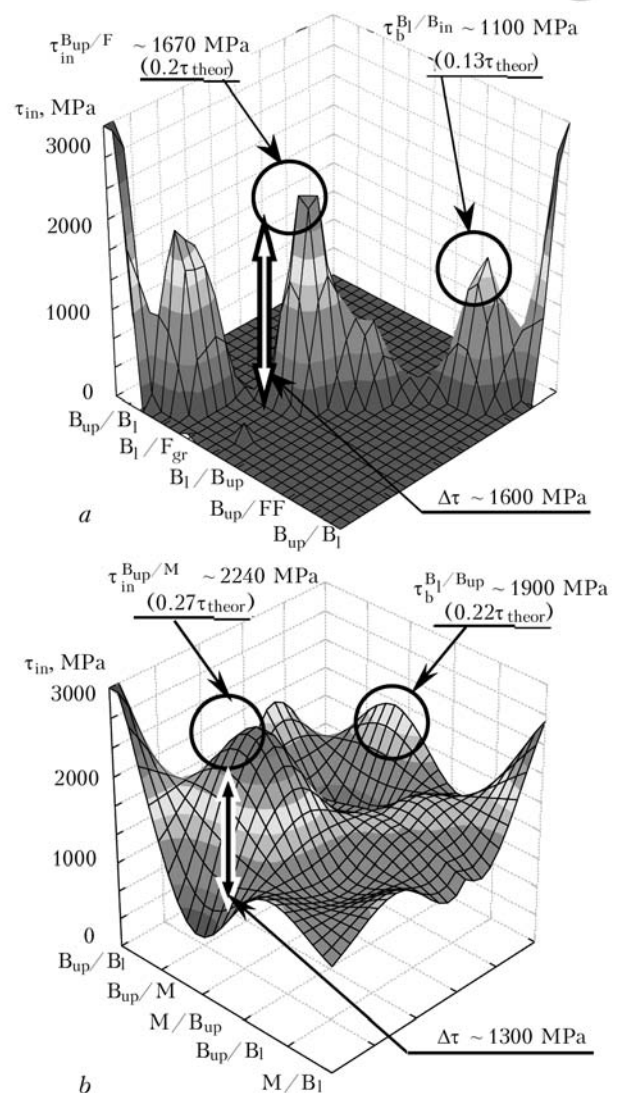


Figure 7. Calculated values of internal stresses τ_{in} forming in zones of B_{up} , B_1 , F localizing and their contact boundaries in the complete recrystallization zone of 17Kh2M steel at different cooling rates: *a* – $w_{6/5} = 2.5$; *b* – $20\text{ }^{\circ}\text{C/s}$

form value of τ_{in} is observed at formation of finely-dispersed structures of, predominantly, lower bainite and tempered martensite $\tau_M = 1900\text{ MPa}$, $\Delta\tau_{M/B_1} = 400\text{--}900\text{ MPa}$, $\epsilon_l \sim 10\text{--}20\text{ }\%$ (Figure 7, *b*).

Comparison of the results of experimental studies and their respective analytical estimation show that distribution of residual local internal stresses and strains largely depends on the structural-phase condition of the weld and HAZ metal. High-gradient internal stress raisers are characteristic for the HAZ metal of welded joints of 17Kh2M steel, which were welded with lower parameters ($w_{6/5} = 2.5\text{ }^{\circ}\text{C/s}$). The situation is further aggravated by the fact that in this case the volume fraction of the critical structure (in terms of stress raiser formation), namely that of upper bainite, is increased. In addition, the zone with formation of abrupt gradients of internal stresses $\Delta\tau_{in}$, which are the potential sites of crack initiation and propagation, in this case includes also the regions of adjacent microvolumes of bainite and FF (Figure 7, *a*).

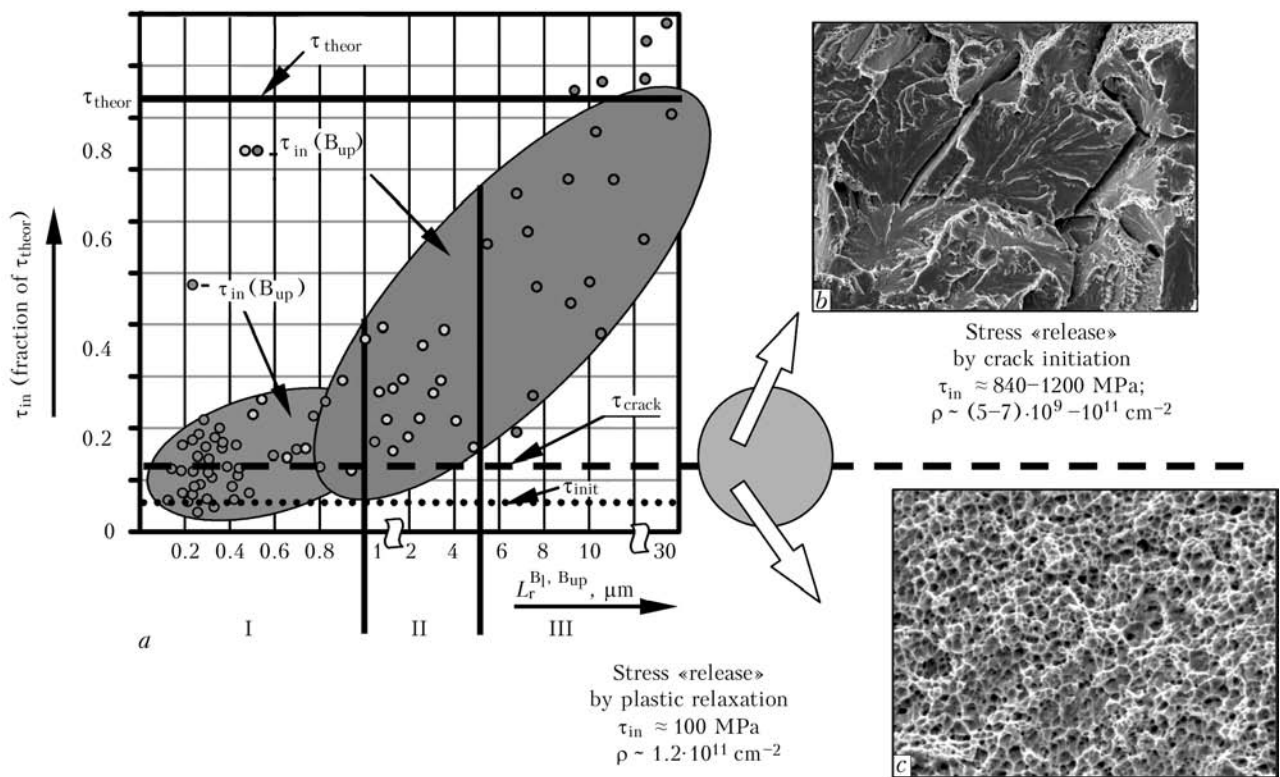


Figure 8. Interrelation between the structure, internal stresses (as a function of power and length of the raiser) (a) and brittle (b), tough (c) nature of fracture ($\times 240$)

At increase of cooling rates $w_{6/5}$ up to 20°C/s , the total level of τ_{in} increases (approximately to 2200 MPa). However, the field of τ_{in} distribution is comparatively uniform, without abrupt gradients, which is ensured by a prevailing formation of structures of the type of lower bainite (see Figure 3, f).

Another issue, which is of special practical importance is how the localized residual stresses vary under the conditions of external loading, and what type of structures will promote plastic relaxation (by dislocation slipping and rotation of structural elements), and, thus, plastic «release» of the increasing internal stresses under these condition and what structures will provoke an abrupt increase of local stresses up to a critical level, i.e. value of theoretical strength, with subsequent brittle fracture. It should be emphasized that realization of a particular mechanism of stress relaxation depends not only on the power of the local internal stress raiser $\Delta\tau_{in/l}$, but also on raiser length L_r . So, at its short length (about $1 \mu m$), which is characteristic primarily for lower bainite structures, the raiser usually blocked by obstacles (phase precipitates, sub- and intergranular boundaries, etc.), as a rule, promotes structure fragmentation. It is exactly the fact of fragmentation, i.e. structure dispersion, that expands the possibilities of plastic relaxation, as the regular dislocation mechanisms in stress «release» are complemented by an additional one — the rotation mechanism, being quite active, as a rule, due to facilitated rotation of fragmented finely-dispersed structures.

In the case of formation of internal stress raisers of a considerable extent ($L_r > 5-10 \mu m$), it is noted

that for upper bainite structures crack initiation and growth and the following brittle fracture are realized practically unhindered. These processes are illustrated in the diagram (Figure 8, a), which presents a change of the length of the internal stress raiser in different structural constituents and change of the fracture mode (brittle, Figure 8, b, or tough fracture, Figure 8, c), depending on these factors.

Performed $\tau_{in/l}$ estimates for the above structures of HAZ metal forming at different cooling rates ($w_{6/5} = 2.5$ and 20°C/s) and their dynamics in the external loading field P_{ex} at transition from the as-welded state P_0 to $P_{ex} \sim 0.8\sigma_t$ showed the following. Under the conditions when the welded joints are cooled at low rates ($w_{6/5} = 2.5^\circ \text{C/s}$), the most critical structural zones are zones of contact of upper bainite with ferrite. In as-welded condition their $\Delta\tau_{in/l}$ level reaches approximately 1700 MPa ($0.2\tau_{theor}$). At subsequent external loading ($P_{ex} \sim 0.8\sigma_t$) value of local stresses in the respective zones rises abruptly up to values of approximately 8400 MPa, i.e. reaches the level of theoretical strength, which may lead to initiation and growth of cracks and brittle fracture, respectively (Figure 8, b). If the most critical in terms of delayed fracture zones under the conditions, when $w_{6/5} = 20^\circ \text{C/s}$, are zones, where upper bainite borders on martensite and $\Delta\tau_{in/l}$ reaches approximately 2200 MPa ($0.27\tau_{theor}$), then at similar external loading ($P_{ex} \sim 0.8\sigma$), τ_{in} level can be close to the theoretical strength value only in the above zones. As the volume fraction of such zones in the HAZ metal is equal to about 5 %, the probability of brittle fracture in such a metal is low — mainly a quasibrittle or tough frac-



ture is observed (Figure 8, *c*). This fact is another indication of the positive influence of structures forming at increased cooling rates (this is particularly true for increase of lower bainite fraction) on improvement of ductility properties of high-strength low-alloyed steel joints.

CONCLUSIONS

1. Investigation of structural-phase state of metal in welded joints of hardening low-alloyed high-strength steels forming at different cooling rates and analytical estimate of their influence on mechanical properties showed that the greatest contribution to increase of yield limit $\sigma_{0.2}$ of HAZ metal of 17Kh2M steel is made by a substructure, due to a large extent to fragmentation of lower bainite, and the minimum contribution is made by the grain structure.

2. Structural-analytical estimates were the basis for prediction of the possible methods to improve the strength properties of welded joints due to adjustment of their structural-phase composition.

3. Characteristics of dislocation distribution and density were used to analyze the processes of formation of zones of strain localizing and internal stress raisers, depending on the type of structures forming in different welding modes ($w_{6/5}$) and magnitudes of subsequent external loading. It is shown that the highest level of local internal stresses is characteristic for zones, in which a structure gradient (ferrite/upper bainite, etc.) is observed. The maximum density and extent of such zones — stress raisers — is observed at application of modes, which provide a low ($w_{6/5} \leq 5$ °C/s) cooling rate of the welded joint, which is related to higher content of upper bainite in the HAZ metal structure in 17Kh2M steel and overall increase of grain size.

4. Under the conditions of external loading the level of local internal stresses (particularly in zone of contact with upper bainite structures) reaches the level of theoretical strength.

- (1953) *Automatic electric arc welding*. Ed. by E.O. Paton. Kiev: Mashgiz.
- (1965) *High-strength steel*. Ed. by L.K. Gordienko. Moscow: Metallurgiya.
- Goudremont, E. (1959) *Special steels*. Moscow: Metallurgizdat.
- Goldshtejn, M.I., Litvinov, V.S., Bronfin, B.M. (1986) *Metals physics of high-strength alloys*: Manual for higher schools. Moscow: Metallurgiya.
- Zherbin, M.M. (1974) *High-strength structural steels*. Kyiv: Budivelnik.
- Enzhin, R.I., Klejner, L.M., Kogan, L.I. et al. (1979) Low alloy martensitic steels. *Izvestiya AN SSSR. Series Metallurgy*, **3**, 114–120.
- Potak, Ya.M. (1972) *High-strength steel*. Ed. by M.L. Bernshtejn, Moscow: Metallurgiya.
- Dahl, W. (1974) Pruefung des Schweiseseignung und Zae-higkeit von Druckbehaelterstaelen. *Der Stahlbau*, **43**(6), 190, 191.
- Ito, Y., Bessyo, K. (1968) Weldability formula of high strength steels related to heat-affected zone cracking. *IIFW Doc. IX-576-68*.
- Coe, F.R. (1973) *Welding steel without hydrogen cracking*. TWI: Abington Hall.
- Makarov, E.L. (1981) *Cold cracks in welding of alloy steels*. Moscow: Mashinostroenie.
- Makarov, E.L., Chaburkin, F.V., Livshits, L.S. (1972) Selection of welding technology ensuring cold cracking resistance of welded joints. *Svaroch. Proizvodstvo*, **8**, 30–32.
- Hrivnak, I., Pitrunova, M., Zayats, Ya. (1983) Measurement and calculation of maximum hardness in near-weld zone of structural steel welded joints. In: *Proc. of 2nd Symp. of CMEA on Application of Mathematical Methods in Study of Weldability* (Sofia, 1983), Pt 2, 213–221.
- Sasaki, H., Watanabe, K., Kirihaire, S. et al. (1974) Influence of reactive stresses on weld root crack formation in welding of high-strength steels. *J. JWS*, **43**(1), 3–14.
- Kasatkin, O.G., Musiyachenko, V.F. (1977) Calculation of welding parameters of high-strength steel. *Avtomatich. Svarka*, **10**, 11–15.
- Kasatkin, O.G., Seyffarth, P. (1984) Interpolation models for evaluation of phase state of heat-affected zone in arc welding of low-alloy steels. *Ibid.*, **1**, 7–11.
- Kasatkin, O.G. (1987) *Calculation of welding parameters and properties of welded joints of higher strength low alloy steels*. Kiev: Znanie.
- Suzuki, H. (1967) About yield strength of polycrystalline metals and alloys. In: *Structure and mechanical properties of metal*. Moscow: Metallurgiya.
- Ashbi, M.F. (1972) About Orowan stress. In: *Physics of strength and ductility*. Moscow: Metallurgiya.
- Goldshtejn, M.I., Litvinov, V.S., Bronfin, B.M. (1986) *Metals physics of high-strength alloys*. Moscow: Metallurgiya.
- Conrad, H. (1973) Model of deformation strengthening to explain the influence of grain size on yield stress of metals. In: *Ultrafine grain in metals*. Ed. by L.K. Gordienko. Moscow: Metallurgiya.
- Armstrong, R. ((1973) Strength properties of metals with ultrafine grain. *Ibid.*
- Petch, N.J. (1953) The cleavage strength of polycrystalline. *J. Iron and Steel Inst.*, **173**(1), 25–28.
- Orowan, E. (1954) *Dislocation in metals*. New York: AIME.
- Ashby, M.F. (1983) Mechanisms of deformation and fracture. *Adv. Appl. Mech.*, **23**, 118–177.
- Kelli, A., Nickolson, R. (1966) *Dispersion hardening*. Moscow: Metallurgiya.
- Ebelling, R., Ashby, M.F. (1966) Yielding and flow of two phase copper alloys. *Phil. Mag.*, **13**(7), 805–809.
- Markashova, L.I., Grigorenko, G.M., Arsenyuk, V.V. et al. (2002) Evaluation criterion of mechanical properties of dissimilar material joints. In: *Proc. of Int. Conf. on Mathematical Modeling and Information Technologies in Welding and Related Processes* (16–20 Sept. 2002, Crimea, Ukraine). Kiev: PWI, 107–113.
- Markashova, L.I., Grigorenko, G.M., Arsenyuk, V.V. et al. (2004) Structural approach to evaluation of mechanical properties in HAZ of steel and alloy joints. *Ibid.*, 174–179.
- Markashova, L.I., Grigorenko, G.M., Poznyakov, V.D. et al. (2008) Structural factors determining the properties of strength, ductility and fracture of welded joints. *Ibid.* (to be publ.).
- Fridman, Ya.B. (1974) *Mechanical properties of metals*. Moscow: Mashinostroenie.
- Koneva, N.A., Lychagin, D.V., Teplyakova, L.A. et al. (1986) *Theoretical and experimental study of disclinations*. Leningrad: LFTI.
- Conrad, H. (1963) Effect of grain size on the lower yield and flow stress of iron and steel. *Acta Metallurgica*, **11**, 75–77.
- Ke, A.S. (1964) *Direct observation of imperfections in crystals*. Moscow: Metallurgiya.



CALCULATION OF PARAMETERS OF LONGITUDINAL MAGNETIC FIELD PROVIDING REMOVAL OF DROP FROM ELECTRODE TIP IN ARC SURFACING

A.D. RAZMYSHLYAEV and M.V. MIRONOVA
Priazovsky State Technical University, Mariupol, Ukraine

Mathematical model of the process of removal of a drop from electrode tip in arc surfacing using the longitudinal magnetic field was developed. It is shown that a field pulse of the appropriate duration is required to remove the drop from the electrode tip at a certain value of the radial component of induction in the drop zone.

Keywords: arc surfacing, longitudinal magnetic field, optimal parameters, calculation model, wire melting coefficient

As follows from studies [1–3], the longitudinal magnetic fields (LMF) used in arc surfacing increases the electrode melting coefficient and, hence, productivity of the surfacing process. This is associated with decrease in size of electrode drops in the axial direction during their rotation under the effect of LMF, as well as with improvement of transfer of heat of the arc to the consumable electrode tip [3, 4]. Study [5] describes the use of calculations to determine the value of only one electromagnetic force (Lorentz force) causing rotation of a drop about the longitudinal axis of an electrode. In our opinion, it is necessary to use the calculation method that would allow for the effect on the drop also by other forces, which form in the drop or influence on it in arc surfacing under the effect of LMF, which will make it possible to reasonably select parameters of LMF to provide removal of drops from the electrode tip and increase productivity of the surfacing process. The present study is dedicated to solving this problem.

As follows from study [6], rotation of a drop at the tip of an electrode from ferromagnetic materials in arc surfacing (welding) under the effect of LMF is caused by the electromagnetic forces acting in the drop metal, which form because of interaction of the radial component of induction of LMF with the axial component of current density in the drop. Proceeding from study [7], the radial component of current density in the drop can be neglected. Therefore, we will allow in the calculations for the above components of induction of LMF and current density in the drop.

When solving the problem, we assume that for the surfacing process parameters [8–10] the maximal diameter of a drop is not in excess of that of the electrode, and that the drop by the moment of detachment has the form of a hemisphere.

To solve the problem, we use the method of balance of integral forces, the expediency of the application of which for addressing such problems is substantiated in study [11].

We proceed from the fact that in arc surfacing with the LMF effect a drop is removed from the electrode tip provided that the balance of forces is violated in its rotation about the axis (vertical, coinciding with the electrode axis). We allow for the effect of four forces — surface tension $F_{s,t}$, centrifugal forces F_c , LMF driven electromagnetic forces (volumetric) F_{em} , and electromagnetic forces F_r (volumetric, reducing the drop in the radial direction), which form in the drop under the effect of the surfacing current flowing in it.

Assume that at the flat tip of a cylindrical electrode a liquid drop has the form of a hemisphere, where the main curvature radius in the horizontal plane (orthogonal to the electrode axis) is equal to the electrode radius ($r_1 = d_e/2$), and that the main curvature radius passing through vertical axis x is $r_2 = r_1$ (Figure 1, *a*). Select an element of layer of the liquid drop with height h , adjoining a solid flat tip of the electrode with radius $r_1 = d_e/2$ in the form of a sector with angle φ (Figure 1, *b*).

As shown by preliminary calculations (estimations), the maximal values of friction forces between the rotating liquid drop and solid surface S_1 of the electrode tip, as well as friction forces between the liquid regions (in the case of detachment of this region) over surfaces S_2 , which prevent motion (rotation) of the drop or detachment of the selected region of the drop with angle φ (Figure 1, *b*), are negligible compared with other forces affecting the drop. In this connection, allow for the effect of forces $F_{s,t}$, F_c , F_{em} and F_r (Figure 1, *b*), which influence the selected region (element) of the liquid drop.

The purpose of the calculations is to determine such a level of induction B_r within the zone of the selected region of the drop, at which this region will detach in a direction of radius r , i.e. the drop will be removed. At the same time, assume that the process of rotation of the drop is considered from the beginning of the effect of a square half-wave of LMF with unchanged values of inductions B_z and B_r . Assume also that the drop was removed during the previous half-wave of LMF, and that it is not necessary to spend forces for its deceleration. It is split into elements of identical sizes, and the above four forces affect each element of the liquid drop with angle φ .

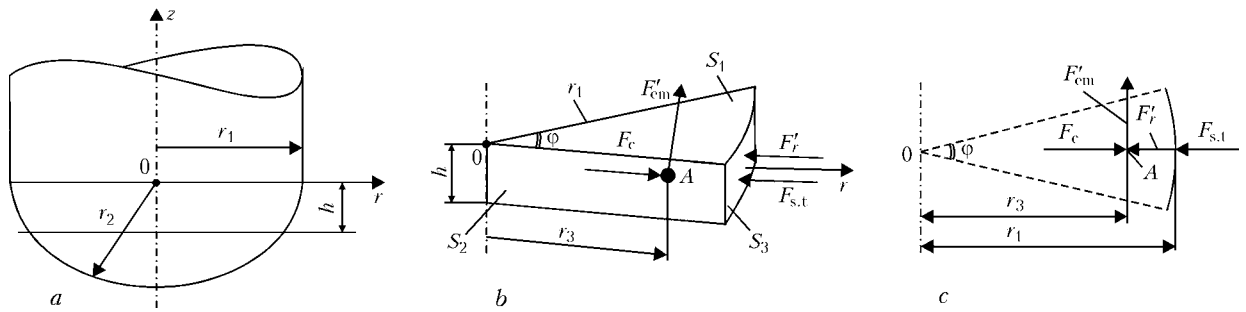


Figure 1. Calculation diagram for rotation of liquid drop in surfacing under the LMF effect (see explanations in the text)

The drop, like each of its elements with a low value of angle ϕ , starts rotating with uniform acceleration (with constant angular acceleration). If the level of induction B_r , as well as the associated level of induction B_z , is higher than the certain limiting level, the balance of forces projected to axis r will be violated, and the drop will be removed by the centrifugal force from the electrode tip.

The required values for the calculations can be determined from the following formulae:

surface area of the drop

$$S_1 = \frac{\phi\pi}{360} r_1^2 [\text{m}^2] \quad (1)$$

(in this and all other formulae the angle is measured in degrees);

$$S_2 = r_1 h [\text{m}^2], \quad (2)$$

$$S_3 = \frac{2\pi r_1 \phi}{360} h [\text{m}^2]; \quad (3)$$

volume of the considered element of the drop with angle ϕ

$$V = S_1 h [\text{m}^3]; \quad (4)$$

surface tension force according to the Laplace's law

$$F_{s,t} = \sigma \left(\frac{1}{r_1} + \frac{1}{r_2} \right) S_3 [\text{N}], \quad (5)$$

where σ is the surface tension of the liquid drop, N/m.

Density of the electromagnetic forces due to induction B_r of LMF with surfacing current I_s flowing in the drop is

$$F_{em} = \frac{4I_s B_r}{\pi d_e^2} [\text{N}/\text{m}^3]. \quad (6)$$

The azimuthal electromagnetic force affecting the element of the drop is

$$F'_{em} = F_{em} V [\text{N}]. \quad (7)$$

The centrifugal force

$$F_c = \rho V \frac{v^2}{r_3} [\text{N}] \quad (8)$$

is generated in the element of the drop under the effect of F'_{em} , where ρ is the density of the liquid drop, kg/m^3 ; and v is the speed of rotation of the drop element (at the centre of the element, at distance $r_3 = 2/3r_1$), m/s.

The density of the electromagnetic field reducing the drop is [11]

$$F_r = \frac{\mu_0 I_s^2 r}{2\pi^2 r_1^4} [\text{N}/\text{m}^3], \quad (9)$$

where r is the current radius, m.

The electromagnetic force reducing the drop in the radial direction is driven in the element of the drop by the surfacing current flowing in it:

$$F'_r = F_r V [\text{N}]. \quad (10)$$

Determine speed v of rotation of the drop (point A in Figure 1, c) from the condition of uniformly accelerated motion:

$$v = \sqrt{2La} [\text{m}/\text{s}]. \quad (11)$$

The path of acceleration of the centre of the selected drop volume (point A in Figure 1, c) is

$$L = \frac{2\phi\pi}{360} r_3 = \frac{4\phi\pi}{3 \cdot 360} r_1; \quad r_3 = \frac{2r_1}{3}. \quad (12)$$

Determine acceleration under the effect of azimuthal electromagnetic field F'_{em} from the following relationships:

$$F'_{em} = F_{em} V; \quad F_{em} = \frac{4I_s B_r}{\pi d_e^2}; \quad F'_{em} = \rho V a; \quad a = \frac{4I_s B_r}{\pi d_e^2 \rho}. \quad (13)$$

Then

$$v = \sqrt{2La} = \sqrt{\frac{16\phi I_s B_r}{3 \cdot 360 d_e \rho}}. \quad (14)$$

The drop will be removed from the electrode tip if projection of all the radial forces affecting its element (Figure 1, b) and axis r is higher than zero (Figure 1, c):

$$F_c - F_{s,t} - F'_r > 0 \quad (15)$$

or

$$V\rho \frac{v^2}{r_3} - \sigma \left(\frac{1}{r_1} + \frac{1}{r_2} \right) S_3 - F'_r > 0. \quad (16)$$

Find from expression (16) that

$$v = \sqrt{\frac{[\sigma(1/r_1 + 1/r_2)S_3 + F'_r]r_3}{V\rho}}. \quad (17)$$

By equating the right parts of expressions (14) and (17), we obtain that

$$\frac{16\phi I_s B_r}{3 \cdot 360 d_e} = \frac{[\sigma(1/r_1 + 1/r_2)S_3 + F'_r]r_3}{V}. \quad (18)$$



Considering that $r_3 = d_e/3$ and $r_1 = d_e/2$, and taking the value of $r = r_1 = d_e/2$ in formula (9), determine that

$$F_r = \frac{4\mu_0 I_s^2}{\pi^2 d_e^3}, \quad F'_r = F_r \frac{V}{2} = \frac{\mu_0 I_s^2 \phi h}{2\pi d_e 360}.$$

The right part in equation (18) can be simplified, allowing for

$$\begin{aligned} S_3 &= \pi d_e \phi h / 360, \quad V = \pi d_e \phi h / 4 \cdot 360, \\ \frac{[\sigma(1/r_1 + 1/r_2)S_3 + F'_r]r_3}{V} &= \\ &= \frac{4 \left[\sigma(1/r_1 + 1/r_2)\pi d_e^2 + \frac{\mu_0 I_s^2}{2\pi} \right]}{3\pi d_e}. \end{aligned}$$

By equating this expression to the left part of equation (18), we obtain the formula for calculation of the minimal value of B_r required for removal of the drop from the electrode tip:

$$B_r = \frac{360 \left[\sigma(1/r_1 + 1/r_2)\pi d_e^2 + \frac{\mu_0 I_s^2}{2\pi} \right]}{4\phi I_s \pi d_e}, \quad (19)$$

and angle of rotation of the drop in its removal

$$\phi = \frac{360 \left[\sigma(1/r_1 + 1/r_2)\pi d_e^2 + \frac{\mu_0 I_s^2}{2\pi} \right]}{4I_s B_r \pi d_e}. \quad (20)$$

The time required for acceleration of the drop in its rotation at speed v and its removal by a pulse of LMF (pulse duration) at $t = 2L/v$, allowing for the L and v values from formulae (12) and (14), is

$$t_{\min} = \sqrt{\frac{\phi}{360} \frac{d_e^3 \rho}{3I_s B_r}}. \quad (21)$$

Substitution of the value of angle ϕ calculated from (20) to expression (21) yields an estimate of the minimal duration of the LMF pulse required for removal of the drop from the electrode tip:

$$t_{\min} = \frac{d_e \sqrt{\rho}}{2\sqrt{3\pi} I_s B_r} \sqrt{\sigma(1/r_1 + 1/r_2)\pi d_e^2 + \frac{\mu_0 I_s^2}{2\pi}}. \quad (22)$$

As follows from (22), duration t of the LMF pulse depends upon the values of d_e , I_s , B_r and r (as well as upon σ , r_1 and r_2). It should be noted as a positive moment that formulae (20) through (22) do not include parameter h .

Determine from formula (22) the minimal time of the pulse with induction B_r of LMF required for removal of the drop in arc surfacing using the electrode of preset diameter d_e and certain surfacing current I_s to increase coefficient α_m of melting of the electrode wire.

Estimate from formula (22) the minimal level of induction required for removal of the drop:

$$B_{r \min} = \frac{d_e \sqrt{\rho}}{2\sqrt{3\pi} I_s t} \sqrt{\sigma(1/r_1 + 1/r_2)\pi d_e^2 + \frac{\mu_0 I_s^2}{2\pi}}. \quad (23)$$

As follows from expressions (22) and (23), the product of parameters $B_r t$ providing removal of the drop from the electrode tip is a constant value for d_e , I_s , ρ and σ used in the calculations.

Surface tension of the drop metal is characterised by the maximum uncertainty for calculation of parameters $B_{r \min}$ and t_{\min} . It is a known fact that at boiling temperature T_b it is practically equal to zero. To estimate the effect of σ on the above LMF parameters, the calculations were made at $\sigma = 1$ N/m and $\sigma = 0$. Angle ϕ was assumed in the calculations to be equal to 36° , layer height $h = 2$ mm, liquid drop metal density $\rho = 7 \cdot 10^{-3}$ kg/m³, and $r_1 = r_2 = 2 \cdot 10^{-3}$ m. It should be noted that B_r is 20–30 % of the axial component of induction B_z of LMF within the zone of the drop at the tip of an electrode from a ferromagnetic material [6]. It was assumed in the calculations that $B_r = 0.2B_z$.

Thus we determined duration t_{\min} of the LMF pulse removing the electrode drop at minimal induction $B_r = 12 \cdot 10^{-3}$ T, which, at the same time, is sufficient for increasing α_m of the electrode [6], at variable values of surfacing current I_s ($d_e = 4 \cdot 10^{-3}$ m). The calculation results showed (Figure 2, *a*) that t_{\min} decreased with increase in I_s . Within the $I_s = 300$ –1000 A range, which is the most common for surfacing with a wire by the submerged-arc method, pulse duration t_{\min} varies over very narrow ranges — $t_{\min} \approx (2.0$ – $3.5) \cdot 10^{-3}$ s. At a constant value of surfacing current I_s , increase in induction B_r leads to decrease in the values of t_{\min} (Figure 2, *b*). At constant values of B_r and I_s , increase in the electrode diameter leads to growth of pulse duration t_{\min} (Figure 2, *c*). It also follows from this Figure that for electrode wires with diameters $d_e = 3$ –5 mm, which are widely applied in arc surfacing, the minimal duration of the LMF pulse required for removal of the drop from the electrode tip in arc surfacing varies within the above narrow ranges, i.e. $t_{\min} \approx (2.0$ – $3.5) \cdot 10^{-3}$ s.

The calculations showed that the effect of σ on $B_{r \min}$ and t_{\min} decreases with increase in I_s and decrease in d_e (at preset I_s). If the effect of σ is neglected (σ is assumed to be equal to zero), the calculated values of t_{\min} decrease by no more than 33 % (curves 2 in Figure 2). If we assume that $r_2 = \infty$ (flat lower surface of the drop), all the calculation data in Figure 2 will be located between curves 1 and 2. Therefore, formulae (22) and (23) suggested for the calculation of $B_{r \min}$ and t_{\min} can be applied for estimations.

Of interest is to determine whether LMF of a commercial frequency can provide removal of drop of the electrode tip by each induction pulse with duration 0.01 s and, thus, increase the values of coefficient α_m in surfacing.

It was assumed in the calculation made for this purpose that after termination of the effect of the LMF pulse and effect of the LMF pulse without a pause in the opposite direction, it would be necessary to determine the time spent for complete deceleration

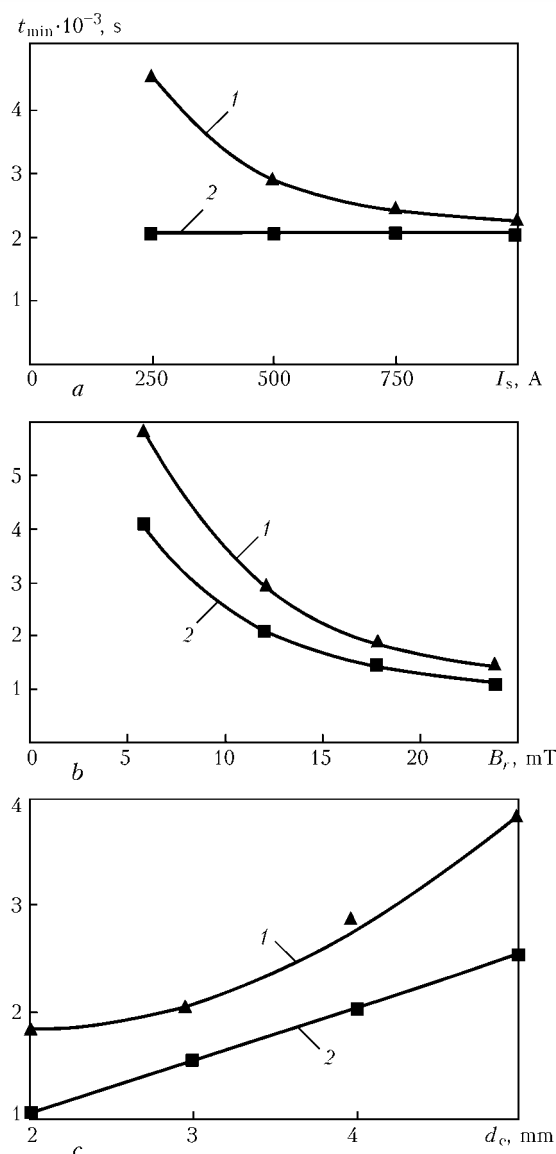


Figure 2. Dependence of duration t_{\min} of the LMF pulse upon the surfacing current (at $d_e = 4 \cdot 10^{-3}$ mm and $B_r = 12 \cdot 10^{-3}$ mT (a)), LMF induction B_r (at $d_e = 4 \cdot 10^{-3}$ mm and $I_s = 500$ A (b)), and electrode diameter (at $I_s = 500$ A and $B_r = 12 \cdot 10^{-3}$ mT (c)): 1 – $\sigma = 1$ N/m; 2 – $\sigma = 0$

of motion of the drop. It became evident in this case that the drop in acceleration passed a certain way with length L (angle ϕ), while in the opposite LMF pulse it should pass the same way (or angle ϕ) in the opposite direction.

The calculation was made for surfacing by using wire Sv-08A (ferromagnetic) with a diameter of 4 mm at $I_s = 500$ A and $B_r = 12$ mT.

If we suppose (as an extreme case) that it is necessary to provide deceleration of the drop with the opposite pulse and its acceleration in the opposite direction, the time of its deceleration at LMF frequency $f = 50$ Hz will be $t = 2.87 \cdot 10^{-3}$ s (Figure 3).

Therefore, in arc surfacing, if the frequency is 50 Hz, the coefficient of melting of electrode wire from ferromagnetic materials will be increased.

Filming of the process of melting of electrode wire with the open arc of reverse polarity without the LMF effect and statistic processing of the frames prove the assumption made with the calculation method that in

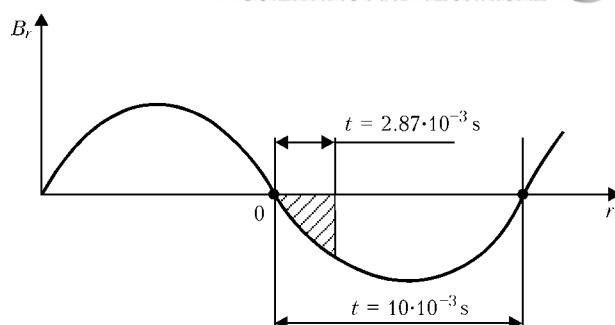


Figure 3. Diagram to allow for the time of deceleration of the drop under the effect of LMF with 50 Hz frequency

general the drop size does not exceed the electrode diameter. Under the effect of constant and alternating LMF with a frequency of 50 Hz, the electrode tip is flat, having a thin interlayer of liquid metal on it. This confirms the calculation data that under the effect of both constant and alternating LMF, including with a frequency of 50 Hz, the magnetic field pulses effectively remove liquid metal from the electrode tip, thus decreasing thickness of the liquid interlayer and leading to increase in the electrode wire melting coefficient [6].

CONCLUSIONS

1. The mathematical model was developed for the process of removal of drop from the electrode tip under the effect of LMF. The model allows determining by calculations the optimal parameters ($B_{r\min}$ and t_{\min}) of LMF, which provide increase in the efficiency of melting of electrode wires in arc surfacing.

2. At a value of the radial component of induction equal to $B_{r\min} = 10$ –12 mT within the drop zone, the LMF pulse with minimal duration $t_{\min} = (2$ –4) $\cdot 10^{-3}$ s is required to remove the drop from the electrode tip.

3. The drop from the electrode tip can be removed and, therefore, the electrode melting coefficient can be increased at a frequency of LMF equal to 50 Hz.

1. Erdman-Jesnitzer, F., Feustel, E. (1967) Grundlagen des Magnetimpulsschweißens. *Schweißen und Schneiden*, 19(1), 2–8.
2. Boldyrev, A.M., Birzhev, V.A., Chernykh, A.V. (1989) Increase in the efficiency of electrode wire melting in longitudinal magnetic field welding. *Svarochn. Proizvodstvo*, 4, 18–19.
3. Boldyrev, A.M., Birzhev, V.A., Chernykh, A.V. (1991) Peculiarities of electrode metal melting in external magnetic field welding. *Ibid.*, 5, 28–30.
4. Kuznetsov, V.D., Malinkin, I.V., Syrovatka, V.V. et al. (1972) Arc behaviour and electrode metal transfer in longitudinal magnetic field welding. *Ibid.*, 4, 3–4.
5. Patskevich, I.R., Zernov, A.V., Serafimov, V.S. (1973) Effect of longitudinal magnetic field on melting and transfer of electrode metal. *Ibid.*, 7, 8–10.
6. Razmyshlyayev, A.D., Deli, A.A., Mironova, M.V. (2007) Effect of longitudinal magnetic field on the efficiency of wire melting in submerged-arc surfacing. *The Paton Welding J.*, 6, 23–27.
7. Voropaj, N.M., Kolesnichenko, A.F., Lunkova, O.N. (1982) Electromagnetic forces in drops during arc melting of cylindrical electrode. *Tekhn. Elektrodinamika*, 6, 11–15.
8. Pokhodnya, I.K., Kostenko, B.A. (1965) Electrode metal melting and its interaction with slag in submerged-arc welding. *Avtomatich. Svarka*, 10, 16–22.
9. Voropaj, N.M., Kolesnichenko, A.F. (1979) Modelling of electrode metal drop shape in gas-shielded welding. *Ibid.*, 9, 27–32.
10. Kolesnichenko, A.F., Voropaj, N.M., Lunkova, O.N. et al. (1977) Numerical method for determination of free surface of drops of electrode metal in its transfer in magnetic field of welding arcs. *Magn. Gidrodinamika*, 3, 121–126.
11. Berezovsky, B.M. (2003) *Mathematical models of arc welding*. Vol. 3: Arc pressure, defects in welds, electrode metal transfer. Chelyabinsk: YuurGU.



LASER WELDING OF TITANIUM ALLOYS

B.E. PATON, V.D. SHELYAGIN, S.V. AKHONIN, V.F. TOPOLSKY, V.Yu. KHASKIN, I.K. PETRICHENKO,
A.V. BERNATSKY, R.N. MISHCHENKO and A.V. SIORA
E.O. Paton Electric Welding Institute, NASU, Kiev, Ukraine

The article describes the optimal scheme of gas shielding chosen for laser welding, which was used to produce joints on alloys VT1-0, VT6, SP15, VT22, VT23 and T110. The feasibility of laser welding of low- and medium alloys was proved. It is shown that the technology of laser welding of high titanium alloys requires further improvement.

Keywords: *laser welding, titanium alloys, gas shielding, process parameters, butt joints, mechanical properties, stress corrosion resistance*

Titanium alloys are widely applied in aircraft and space engineering, ship building, chemical engineering, power generation and many other industrial sectors [1]. For example, the modern aircraft construction industry uses stringer panels produced by welding stiffeners to a one-piece panel with the slot welds. Welded T-beams of a titanium alloy are employed to manufacture long-length structures of sea-going ships. Casing structures of some devices consisting of titanium components are also planned to weld. Solving the above problems is complicated by large sizes and small thickness of walls of the parts to be welded. In this connection, the most common method for joining thin-sheet structures of titanium alloys is electron beam welding [2]. However, this method is not always applicable for large-size structures, as it requires the use of vacuum chambers. Traditional arc welding methods often have low productivity, and may lead to substantial distortions and buckling of welded structures [3]. All the above-said raises interest of researchers in laser welding, which allows making narrow welds with a small heat-affected zone (HAZ) at a speed that is 2–3 (or more) times higher than that of arc welding, without the need to employ sophisticated vacuum chambers [4].

The first attempts to apply laser radiation for welding titanium alloys date back to the early 1970s. In particular, such work was performed at the E.O. Paton Electric Welding Institute [5]. The work showed that liquid metal of the weld pool, because of its active chemical interaction with the environment, requires a reliable inert gas shielding. As reported in study [5], the use of helium instead of argon for shielding the pool metal allows the metal penetration depth to be increased by more than 50 %. The first examples of commercial application of laser welding for joining titanium parts appeared at the beginning of the 1980s. Worthy of notice in this respect is the work done by the I.V. Kurchatov Atomic Energy Institute. For example, in 1983 the All-Russian Association «Baltiysky Zavod» applied the commercial technology for laser welding of a special titanium alloy heat-exchanging

module, where the tubes with a wall thickness of up to 2.5 mm were welded into the tube plate [6]. The possibility of using laser radiation for welding titanium parts is also reported in study [7].

The purpose of the present study was to optimise the laser welding process on the basis of criteria of mechanical properties of welded joints on titanium alloys by selecting the process speed at a fixed power of the laser beam. To achieve this purpose, the system was developed for gas shielding of the weld pool and region of its tailing part where the metal had a temperature above 200 °C, as at such a temperature the probability exists of saturation of upper layer of the weld metal and base metal with air nitrogen [1]. Commercial titanium VT1-0, medium alloy VT6 with β -stabilisers, and high alloys SP15, VT22, VT23 and T110 were used as materials of the workpieces 5.0–7.5 mm thick. Chemical composition of these alloys is given in Table 1.

The experiments were carried out by butt welding of plates measuring $300 \times 50 \times \delta$ mm using the Rofin Sinar (Germany) Nd:YAG laser DY 044 with a power of up to 4.4 kW and the welding head comprising an objective lens with focal distance $F = 300$ mm. The beam was transferred from the laser to lens via an optical fibre 600 μ m in diameter. The welding head with the shielding system was moved during the welding process. In all the cases the lower (root) part of the weld was shielded by argon at a flow rate of 7 l/min. For this, argon was fed via a tube located in the pressure device. The upper part of the weld (molten pool and its tailing part) was shielded by using the welding head nozzle.

A series of preliminary experiments was conducted in order to optimise design of the shielding nozzle and choose the shielding gas type. The first to test was the scheme of welding shown in Figure 1. It was found that the shielding gas (argon or helium) fed ahead of the welding head leads to leakage of air to the welding zone, which is intolerable. Then the scheme shown in Figure 2 was tried. The coaxial feed of gas (argon or helium) provided a reliable shielding of the welding zone. However, this caused a substantial decrease (up to 50 %) in metal penetration depth, compared with that achieved with the scheme shown in Figure 1.

Table 1. Chemical composition of base metal of workpieces

Alloy grade	Chemical composition, wt.%									
	Al	Mo	V	Fe	Cr	Nb	Zr	O ₂	N ₂	H ₂
VT1	0.4	–	–	0.15	–	–	–	0.1	0.035	0.008
VT6	6.35	–	4.2	–	–	–	–	0.15	0.05	0.012
SP15	4.5	3.18	3.3	–	–	4.22	1.9	0.16	0.028	0.002
VT22	6.0	4.8	5.1	1.0	1.0	–	–	0.18	0.05	0.015
VT23	4.5	2.0	4.5	0.6	1.0	–	–	0.17	0.004	0.018
T110	4.9	0.9	1.25	1.61	–	4.74	0.5	0.13	0.04	0.002

Moreover, it turned out that the scheme of Figure 2 failed to provide shielding of the cooling metal from the ambient air. As a result, a thin (0.1–0.3 mm thick) surface layer of the weld metal was saturated with nitrogen to form titanium nitride, having a goldish colour.

To eliminate drawbacks of both gas shielding schemes, the system was developed for differential feed of laminar gas flows to shield the weld pool and cooling metal of its tailing part from the air effect (Figure 3). As found in the course of investigations of technological capabilities of this welding scheme, the feed of argon to shield the weld pool led to partial screening of the laser beam by the plasma plume formed over the pool, thus causing a substantial decrease in the penetration depth. The use of helium permitted avoidance of this effect. Therefore, further experiments were conducted by using the scheme shown in Figure 3. For this case, helium at a flow rate of $Q_1 = 7$ l/min was used as a shielding gas for the weld pool, and argon at a flow rate of $Q_2 = 12$ l/min was used to shield the cooling metal. The

optimal welding parameters given in Table 2 were chosen from the criterion of complete penetration of metal with formation of a narrow (0.5–1.0 mm) weld root, the beam power being $P = 4.0$ – 4.3 kW.

All the workpieces were subjected to X-ray inspection after welding. Results of X-ray tests of the laser welded joints showed the presence of only isolated pores in the welds made by the optimal scheme and at the optimal parameters (Figure 4, *a*). Deviation from the optimal welding technology led to formation of a continuous chain of pores along the weld axis (Figure 4, *b*).

The laser weld metal was studied to check the content of gas impurities (Table 3). As shown by gas analysis, the use of helium and argon as a shielding atmosphere provided the content of oxygen, nitrogen and hydrogen in the welds at a level of that of the base metal, which corresponded to requirements of GOST 22178-176 and ASTM, while that for T110 corresponded to requirements of TUU 27.4.0544/6923.071–2005.

To relieve residual stresses and stabilise structure, the workpieces were subjected to annealing at tem-

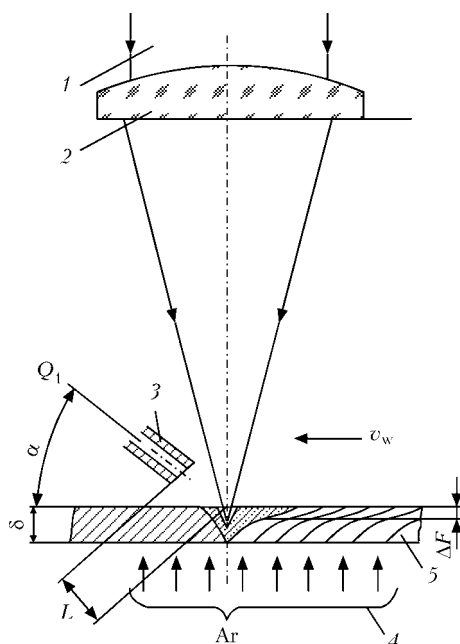


Figure 1. Scheme of laser welding with shielding gas fed ahead of the welding head: 1 – laser radiation; 2 – focusing lens; 3 – nozzle for feed of shielding gas; 4 – shielding of weld root; 5 – workpiece

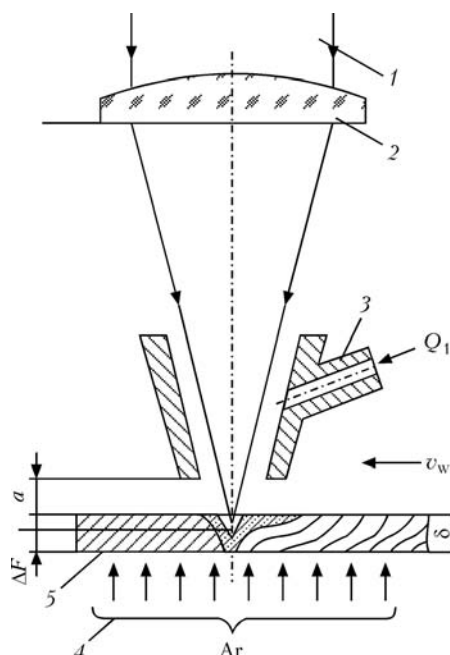


Figure 2. Scheme of laser welding with coaxial feed of shielding gas: 1 – laser radiation; 2 – focusing lens; 3 – nozzle for feed of shielding gas; 4 – shielding of weld root; 5 – workpiece

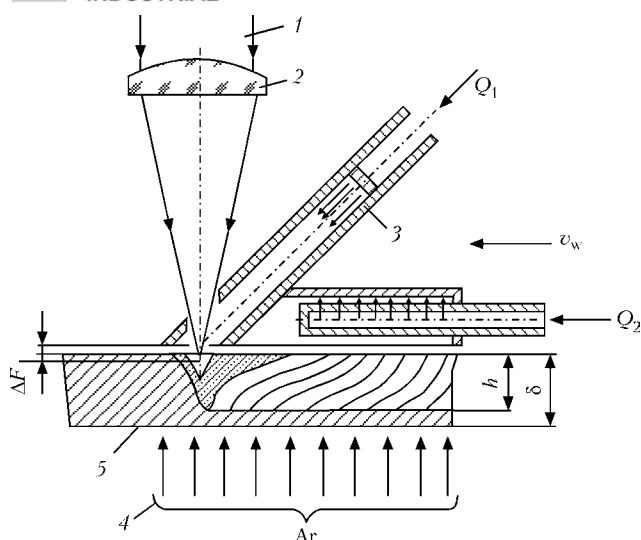


Figure 3. Scheme of laser welding with differential shielding of weld pool and cooling metal by using laminar gas flows: 1 – laser radiation; 2 – focusing lens; 3 – nozzle for differential feed of shielding gases at flow rates Q_1 and Q_2 ; 4 – shielding of weld root; 5 – workpiece

perature of 650–950 °C, depending upon the alloy grade. The welded joints were tensile and impact bend tested in the as-welded condition and after annealing. Results of the mechanical tests are given in Table 4.

The joints on commercial titanium and alloy VT6, the coefficient of stability of the β -phase of which was 0.3, had high mechanical properties in compliance with the GOST requirements. The welded joints on alloys with a coefficient of stability of the β -phase equal to 0.6 or more (alloys SP15, VT23, T110 and VT22) exhibited a high sensitivity to the thermal cycle of laser welding. Both in the as-welded condition and after annealing, the weld and HAZ metals on these alloys had a finely dispersed structure, which provided strength of the joints equal to that of the base metal. However, impact toughness of the welds and HAZ on the high alloy was unsatisfactory both in the as-welded condition and after annealing.

The weld and HAZ metals of the laser welded joints on alloy VT6 had a coarse acicular structure (Figure 5, *a*), in contrast to similar zones of the welded joints on the high alloys having an extremely fine intragranular structure (Figure 5, *b, c*). These structural differences are one of the reasons of a considerable decrease in impact toughness of the high alloys, compared with commercial titanium and alloy VT6, where the cracks at fracture had a crooked propagation path. In the high alloys with a finely dispersed structure the cracks propagated via a trajectory close to the straight-line one, this requiring less energy than in the case of alloys VT1-0 and VT6 [8].

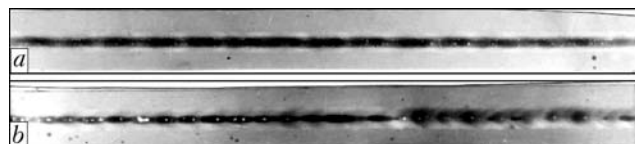


Figure 4. X-ray patterns of laser welded joints on alloy VT6: *a* – laser welding at optimal parameters; *b* – at non-optimal parameters

Table 2. Laser welding process parameters

Base metal	Workpiece thickness δ , mm	Power P , kW	Welding speed v , m/h	Focus deepening ΔF , mm
VT1	5.0	4.1	48	2.0
VT6	7.5	4.3	36	2.0
SP15	6.5	4.0	42	2.0
VT22	6.5	4.2	30	2.0
VT23	6.0	4.0	42	1.0
T110	7.0	4.0	42	2.0

Improvement of the technology for laser welding of high titanium alloys is indicated with a purpose to increase ductile properties of metal in parallel with selecting the optimal parameters for heat treatment of the resulting joints.

It was of high interest to compare results obtained on VT6 alloy joints made by laser welding and VT6 alloy joints made by other welding methods. For this, investigations of the joints on widely applied alloy VT6 made by laser welding were carried out in parallel with investigations of the joints on the same alloy made by the earlier optimised technologies of argon-arc welding (AAW) and electron beam welding (EBW) [9, 10].

The butt joints on plates were made by using the EBW machine UL-144 (power unit ELA 60/60) and commercial equipment for TIG welding of titanium. TIG welding was performed over the layer of flux ANT-25A. Helium and argon were used as a shielding gas for laser welding, and argon – for TIG welding. In all the cases the welding process parameters ensured formation of the welds in one pass without groove preparation. Filler wire was not used. Despite the fact that heat input in laser welding was lower (2.43 kJ/cm) than in EBW (3.11 kJ/cm) and arc welding (4.77 kJ/cm), that is 1.3–2 times, respectively, the values of strength of the welded joints differed just insignificantly, and were close to those of the base metal (Table 5). Impact toughness of the weld and HAZ metal was 70–80 % of that of the base metal, which in all the cases met requirements of

Table 3. Content of gas impurities in laser welds

Alloy	Content of impurities, wt.%					
	O ₂		N ₂		H ₂	
	Weld	HAZ	Weld	HAZ	Weld	HAZ
VT1-0	0.12	0.13	0.04	0.041	0.012	0.011
VT6	0.15	0.10	0.05	0.045	0.013	0.011
VT22	0.18	0.17	0.05	0.05	0.014	0.012
VT23	0.17	0.20	0.045	0.05	0.017	0.016
SP15	0.14	0.13	0.043	0.041	0.016	0.015
T110	0.15	0.12	0.06	0.045	0.013	0.013



Figure 5. Microstructure of weld metal of laser welded joints on titanium alloys: *a* – VT6 (×200); *b* – VT23 (×400); *c* – T110 (×400)

Table 4. Mechanical properties of laser welded joints on titanium alloys

Alloy grade	Condition studied	Welded joints			Base metal	
		σ_t , MPa	KCV, J/cm ²		σ_t , MPa	KCV, J/cm ²
			Weld	HAZ		
VT1-0	As-welded	460	140	130	460	150
	After annealing	440	150	145		
VT6	As-welded	1010	30	34	980	45
	After annealing	980	35	38		
SP15	As-welded	1040	12	18	1030	43
	After annealing	1030	19	30		
VT23	As-welded	1050	8	9	1050	31
	After annealing	1020	16	21		
T110	As-welded	1080	12	19	1100	38
	After annealing	1050	13	20		
VT22	As-welded	1070	8	11	1050	30
	After annealing	1040	9	12		

GOSTs and technological instructions for titanium alloy VT6.

The sensitivity of alloy VT6 and its welded joints to stress corrosion cracking was determined in solution of methyl alcohol with an addition of 0.4 % hydrochloric acid. The tests were carried out at room temperature for 790 h. Each batch consisted of 5 specimens. One of them (reference), No. 1, in each batch was tested in air, whereas the others were tested in the aggressive environment. According to the standard, if all the specimens in a batch did not crack after holding in the aggressive environment for 100 h, the alloy or welded joint should be considered resistant to stress corrosion cracking.

Results of the corrosion tests of the VT6 alloy joints are given in Table 6. Analysis of the results shows that the VT6 alloy joints made by different welding methods using the optimised technologies, including laser welding, are resistant to corrosion cracking.

CONCLUSIONS

1. The optimal scheme of shielding of the weld metal and composition of the shielding atmosphere were chosen for laser welding of titanium alloys. The optimal

Table 5. Mechanical properties of welded joints on titanium alloy VT6 made by different welding methods

Welding method	σ_t , MPa	KCV, J/cm ²		Fracture location
		Weld	HAZ	
Arc welding	940	33	34	Weld
EBW	970	34	31	HAZ
Laser welding	980	35	36	HAZ
Base metal: $\sigma_t = 998$ MPa, $\sigma_{0.2} = 970$ MPa, $\delta = 12$ %, $\psi = 24$ %, KCV = 42 J/cm ² .				

parameters of laser welding were chosen for alloys VT1-0 and VT6. It was shown that it is necessary to use helium to shield the weld metal, and argon – to shield the cooling regions of the base metal in laser welding of commercial titanium and alloy VT6.

2. Strength of the laser welded joints on alloy VT6 is at a level of the base metal, and impact toughness of the welds and HAZ is about 70 % of KCV of the base metal.

3. The welded joints on alloy VT6 made by the improved technologies of AAW over the flux layer, EBW and laser welding meet requirements of the

**Table 6.** Sensitivity of welded joints on alloy VT6 to stress corrosion cracking

Characteristic of specimens tested	Specimen No.	Time to formation of corrosion crack, h	Total test time, h	Fracture location
Base metal	1	N/D	790 (air)	All specimens were removed from tests without fracture
	2	Same	790	
	3	»	790	
	4	»	790	
	5	»	790	
AAW	1	»	790 (air)	No fracture
	2	107	107	Weld
	3	N/D	790	No fracture
	4	264	264	HAZ
	5	N/D	790	No fracture
EBW	1	Same	790 (air)	Same
	2	»	790	»
	3	330	330	HAZ
	4	350	350	Same
	5	N/D	790	No fracture
Laser welding	1	Same	790 (air)	Same
	2	»	790	»
	3	»	790	»
	4	504	504	»
	5	N/D	790	»

standard and are resistant to stress corrosion cracking, although corrosion resistance of the welded joints is inferior to that of the base metal.

4. The need was established for further improvement of the technology of laser welding and optimisation of parameters of heat treatment of the welded joints on high titanium alloys.

Acknowledgement. *The authors express gratitude to Prof. Polyakov S.G. and associates of his department for consultations and conducting of investigations of stress corrosion resistance of welded joints on titanium alloy VT6.*

1. Gurevich, S.M., Zamkov, V.N., Blashchuk, V.E. et al. (1986) *Metallurgy and technology of welding of titanium and its alloys*. Kiev: Naukova Dumka.
2. Nazarenko, O.K., Kajdalov, A.A., Kovbasenko, S.N. et al. (1987) *Electron beam welding*. Ed. by B.E. Paton. Kiev: Naukova Dumka.
3. (1974) *Technology of fusion electric welding of metals and alloys*. Ed. by B.E. Paton. Moscow: Mashinostroenie.
4. Grigoriants, A.G., Shiganov, I.N. (1988) *Laser technique and technology*. Book 5: Laser welding of metals: Manual. Moscow: Vysshaya Shkola.
5. Velichko, O.A., Garashchuk, V.P., Molchan, I.V. et al. (1974) Laser welds on steel and titanium. *Avtomatic. Svarka*, **10**, 19–21.
6. Zhurov, N.V., Milrud, S.R. (1983) Some technological peculiarities of laser welding of pipe joints. In: *Proc. of Short-Term Seminar on Application of High Energy Density Power Sources in Welding Production* (20–21 December, 1983, Leningrad). Leningrad: LDNTP.
7. Zamkov, V.N., Prilutsky, V.P., Novikov, Yu.K. (1993) Achievements in titanium welding technology. *Avtomatic. Svarka*, **5**, 25–27.
8. Borisova, E.A., Bocharov, G.A., Brun, M.Ya. et al. (1980) *Titanium alloys. Metallography of titanium alloys*. Moscow: Metallurgiya.
9. Zamkov, V.N., Prilutsky, V.P. (1980) Technological possibilities of argon-arc welding of titanium over a layer of flux. In: *Proc. of 1st All-Union Conf. on Current Problems of Welding of Non-Ferrous Metals*. Kiev: Naukova Dumka.
10. Zamkov, V.N., Prilutsky, V.P., Petrichenko, I.K., et al. (2001) Effect of the method of fusion welding on properties of welded joints in alloy Ti–6Al–4V. *The Paton Welding J.*, **4**, 2–6.

APPLICATION OF ELECTRON BEAM WELDING IN THE NUCLEAR INDUSTRY (REVIEW)

Yo. URATANI¹, G. TAKANO², M. NAYAMA¹ and Yo. SHIMOKUSU¹

¹Mitsubishi Heavy Industries, Ltd., Kobe, Japan

²Nuclear Plant Service Engineering Co. Ltd., Kobe, Japan

Nuclear power generation in the energy supply is becoming increasingly important from the viewpoint of future energy resources and preventing of global warming. The assurance of safety in the nuclear power plant is an absolutely essential condition. In the fabrication of related nuclear power plant equipments, improvements have been conducted in order to raise the reliability. One of the most suitable joining techniques is the electron beam welding. This review describes the recent application of the electron beam welding for PWR nuclear power plant.

Keywords: *electron beam welding, PWR, nuclear power plant, austenitic stainless steel, carbon steel, low alloy steel, welding conditions, weld defect, toughness, welded joint properties, postweld heat treatment*

In Japan, nuclear power generation occupies about 30 % of gross generation in the energy supply and holds an important position in electric power supply. Since nuclear power plant (NPP) should not leak radioactive materials to the outside, it is important to increase the reliability of welding techniques. In the fabrication of related NPP equipment, improvements have been sought in every aspect in order to improve reliability. One of the most suitable joining techniques is the electron beam welding (EBW) and its application can do much toward improving the quality and reliability of NPP components.

The authors studied in a wide range about the welding conditions, weld defects and welded joint properties for the purpose of applying the EBW to austenitic stainless steel, carbon steel and low alloy steel equipments for PWR NPPs. This review describes the recent application of the EBW for PWR NPP.

PWR nuclear power plant. PWR NPP system is shown in Figure 1. Materials to be used for PWR NPP are required to have high performance to endure severe operation circumstances such as irradiation embrittlement resistance, corrosion resistance and high temperature strength, etc. Because of this reason, carbon steel, low alloy steel, austenitic stainless steel, alloy 600, etc. are used.

Vessels exposed to the reactor coolant primary water are the reactor vessel, steam generator, pressurizer and accumulator inside the containment vessel and are various auxiliary tanks outside the containment vessel. The pressure vessels in the containment vessel are made of low alloy steel or carbon steel, and their inner surfaces are overlaid with stainless steel. There are about 100 sets of the auxiliary tanks in 4 loops of PWR NPP and they are made of austenitic stainless steel. Pippings connecting these vessels are made of austenitic stainless steel. The main coolant pipes for cooling the reactor are about 900 mm in

outside diameter and about 80 mm in wall thickness. Besides, reactor core internals are also made of austenitic stainless steel. The accumulator (diameter of 3.5 m, height of 5.2 m, wall thickness of 90 mm) is made of carbon steel and the steam generator (diameter of 2.35 m, wall thickness of 120 mm) is made of low alloy steel.

Austenitic stainless steel. In applying EBW to the actual fabrication, careful studies are required of on the features of the welding equipment and problems relating to welding procedures. These are roughly classified into items, such as EBW equipment, materials, weld defects and welded joint properties. In conducting the tested, AISI 304 and AISI 316 types of austenitic stainless steel with plate thickness below 80 mm were used. Welding was carried out using EBW equipment with 120 kW capacity.

EBW conditions. The appropriate welding conditions were studied for AISI 304 plates with thicknesses of 20, 50 and 80 mm at the accelerating voltage of 60 kV. Melt-run welding was carried out with a constant focal length at various beam currents and welding speeds. The internal weld quality was checked using radiographic testing and macrosection inspection. Figure 2 shows the appropriate welding conditions arranged for heat input and welding speed per unit plate thickness. This shows that as the plate becomes thicker the appropriate range is narrower and the appropriate speed is slower.

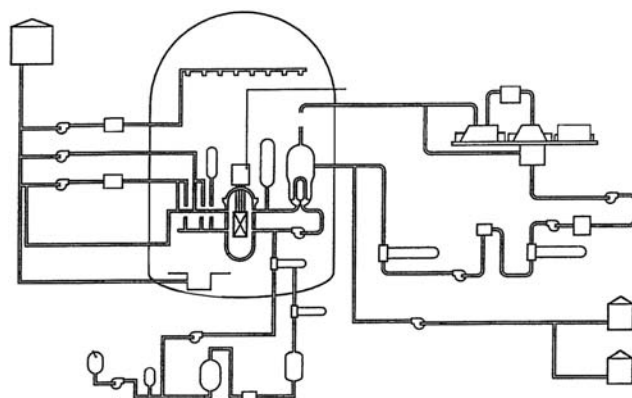


Figure 1. PWR NPP system

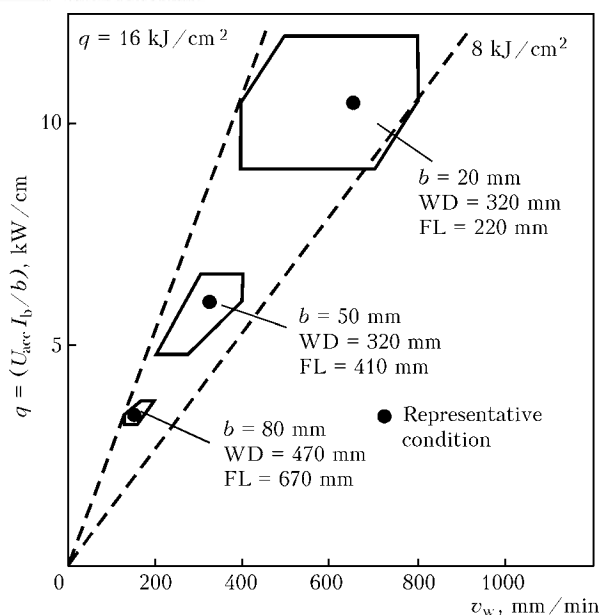


Figure 2. Suitable welding speed v_w and heat q input for various thicknesses of AISI 304 plate b at $U_{acc} = 60$ kV in horizontal EBW

Effect of vacuum pressure. For EBW, a vacuum pressure of $6.7 \cdot 10^{-2}$ Pa is generally used in a welding chamber. However, an EB gun provided with a differential pumping system, such as used in the present test, can be used even at a vacuum pressure of 6.7 Pa in a welding chamber. Even if vacuum level has no

effect on penetration characteristics or weld quality, low vacuum welding is still desirable from an economical viewpoint for reducing vacuum exhaust time. For EBW local vacuum system [1], as a rule, low vacuum of 1.3–6.3 Pa is used. Vacuum pressure of about 13 Pa is considered to cause a sharp change in depth of penetration [2], thus, investigation was undertaken on weldability varying vacuum pressure of a welding chamber in the range of 6.7 – $1.3 \cdot 10^{-2}$ Pa. A macrostructure is shown in Figure 3 for horizontal position welding at 50 and 80 mm thickness and flat partial penetration welding at 50 mm. In each case, vacuum pressure of below 6.7 Pa allowed similar weld results to be obtained. The gas content of weld metal with that of base metal is compared. With the vacuum pressure of a welding chamber in the range of 6.7 – $1.3 \cdot 10^{-2}$ Pa, the oxygen and nitrogen levels of weld metal were not different from each other, and constant. These oxygen and nitrogen levels were both lower than those for the base metal, suggesting that degasification occurred. The above results revealed that vacuum pressure of below 6.7 Pa has no effect on EBW.

Chemical compositions for preventing weld defects. For welding of austenitic stainless steel, weld metal with a ferrite level of above 5 % is generally used to prevent hot cracking [3, 4]. However, the ferrite level of weld metal for EBW, for which filler metal is not usually added, depends on the ferrite

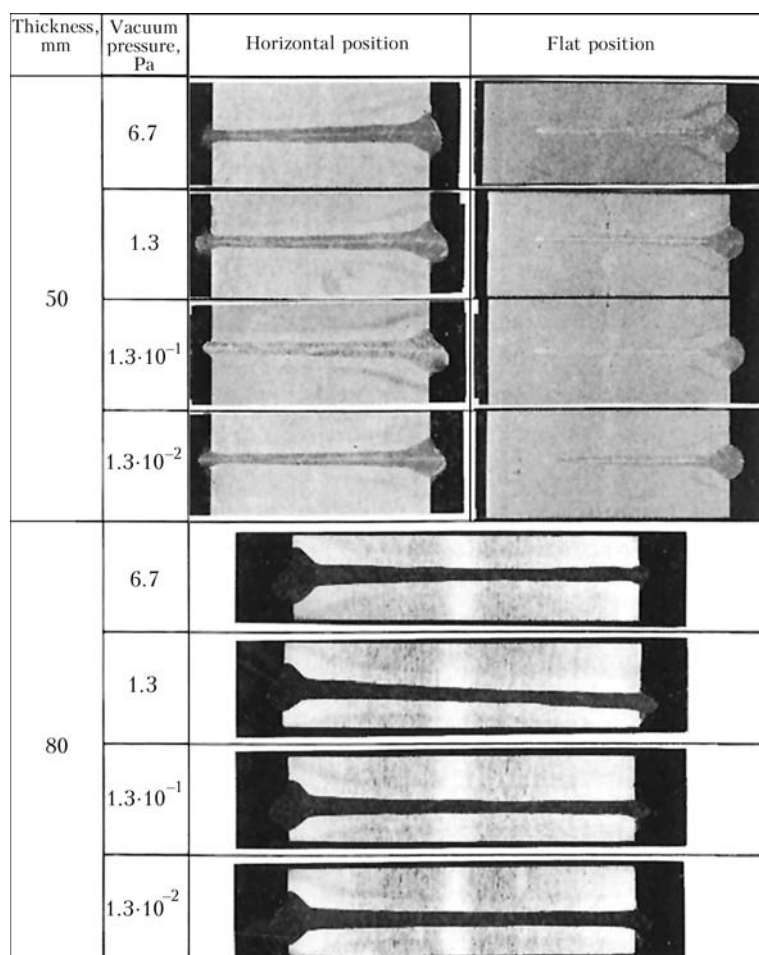


Figure 3. Effect of vacuum pressure on bead shape

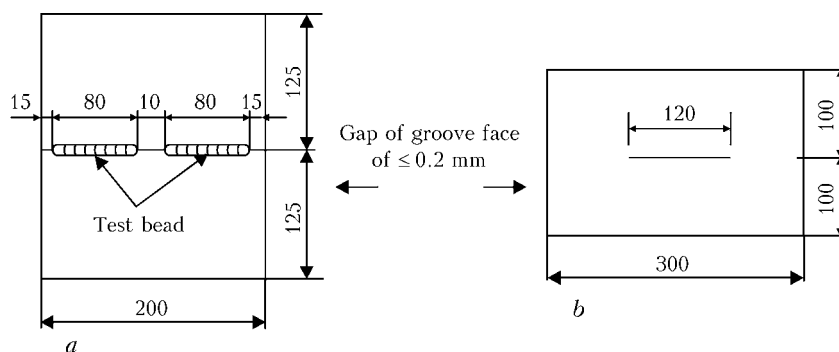


Figure 4. Shape of the weld cracking test plate 20 (a) and 80 (b) mm thick

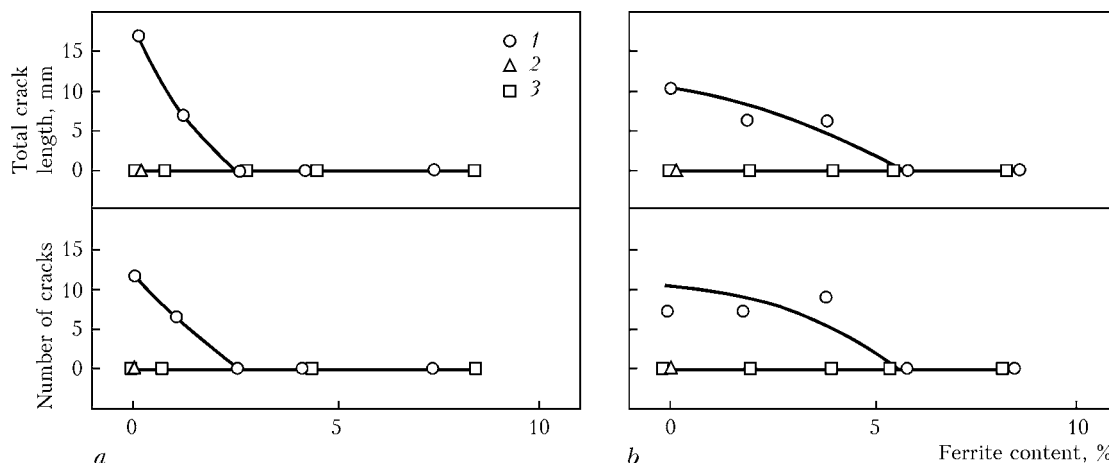


Figure 5. Weld cracking test results: a – AISI 304; b – AISI 316: 1 – $(P + S) = 0.07$; 2 – 0.045; 3 – 0.03 wt.%

level of the base metal chemical compositions. We examined a series of alloys to determine the influence of ferrite on cracking in electron beam weldments. Because $(P + S)$ also contributes to hot cracking susceptibility, we included two $(P + S)$ levels in the materials to be examined: 0.03 % (ordinary material) and 0.07 % (upper limit of standard). The ferrite level varied at 5 levels of 0, 1, 3, 5 and 8 %. Further, a total of 11 types of materials with ferrite level of 0 % and $(P + S)$ level of 0.045 % were applied to two kinds of material, AISI 304 and AISI 316, to provide a total of 22 types of materials for testing. The shape of test plate is shown in Figure 4. For a thickness of 20 mm, the FISCO type cracking tests was performed. The slit type cracking test was performed on 80 mm plate. Welding conditions are shown in Table 1. For the plate thickness of 20 and 80 mm, crack examination was conducted on 6 and 5 sections, respectively. The test results on AISI 304 is shown in Figure 5, a. In materials with $(P + S)$ levels of 0.045 and 0.03 %, no cracks were observed for changes of 0 to 8 % in ferrite level. However, in materials with $(P + S)$ level of 0.07 %, fine hot cracks were detected inside weld metal at a plate 20 mm thick for ferrite level of below 1.1 %. Figure 5, b indicates the test result for AISI 316. As in the case of AISI 316, no cracks were observed in materials with $(P + S)$ level of below 0.045 %, while hot cracks were detected in materials with $(P + S)$ level of 0.07 % and ferrite level of below 3.8 %. This difference in crack susceptibility between

AISI 304 and AISI 316 is thought attributable to a solidification structure. That is, all the AISI 304 materials, whose weld metal microstructure is considered to have the primary δ -crystals had a structure of ferrite being present in austenite matrix, not being influenced by ferrite level. On the other hand, AISI 316 materials mostly had an austenite structure at a ferrite level of below 2 %, and a structure on ferrite in an austenite matrix at ferrite levels of about 4 %.

The weld cracking test results are compared with Moissio's diagram [5] in Figure 6. Cr_{eq}/Ni_{eq} level to occur hot cracking is almost equal between EBW and arc welding. But concerning $(P + S)$ level to occur hot cracking, critical value of EBW is higher than that of arc welding. The difference in crack susceptibility between EBW and arc welding is thought the following reason. EBW performed by 1 pass with 2

Table 1. EBW conditions for AISI 304 steel to be evaluated for weld metal crack susceptibility

Thickness, mm	Welding position	Beam current, mA	Welding speed, mm/min	Focus current, A (focal length, mm)	Work distance, mm
20	Horizontal	300	700	0.903 (220)	320
80	Same	500	200	0.755 (670)	470
80	Flat	350	550	0.750 (570)	450

Note. Accelerating voltage of 60 kV, vacuum pressure – $133.3 \cdot 10^{-2}$ Pa.

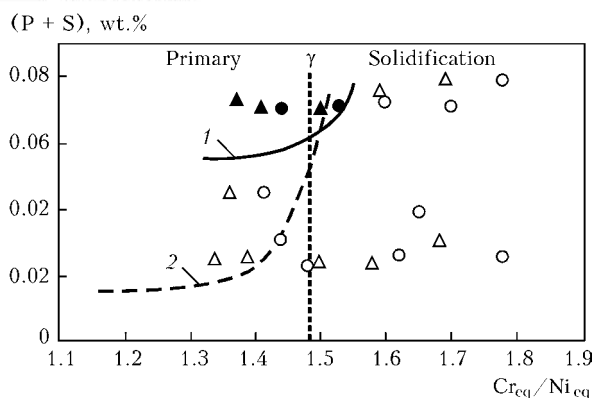


Figure 6. Effect of Cr_{eq}/Ni_{eq} and $(P + S)$ level on hot cracking susceptibility of AISI 304 (O) and AISI 316 (Δ) weld metal: ●, ▲ — cracks present; 1 — critical line for EBW; 2 — of Moissio's diagram

dimensional heat flow, consequently induced strain to weld metal is small. The above results revealed that EB-welded metal also requires its $(P + S)$ or ferrite level to be limited so as to prevent hot cracking as in the case of arc welding. In actual welding, it is considered to be more effective to control $(P + S)$ level.

With EBW, high gas contents of the base metal lead to porosity inside the weld metal occurring. To prevent this for steel materials, the oxygen and nitrogen levels are required to be limited to approximately 100 ppm or below. Austenitic stainless steel usually contains about 400 ppm of nitrogen and about 75 ppm of oxygen in the austenite structure, which allows larger solubility of nitrogen than ferrite structure. AISI 304 materials whose gas contents have been varied at nitrogen levels of 300, 600, 900 and 1200 ppm and oxygen levels of 50, 75 and 100 ppm were used for testing. In addition, to investigate the effects of plate thickness and welding position, plate thickness of 20, 50 and 80 mm were used for horizontal position welding, and 80 mm plate (depth of penetration of about 40 mm) was used for flat position partial penetration welding. Testing was conducted by meltrun welding using conditions representative for each plate thickness. Figure 7 shows the test result. The gas contents that caused no porosity to occur were nitro-

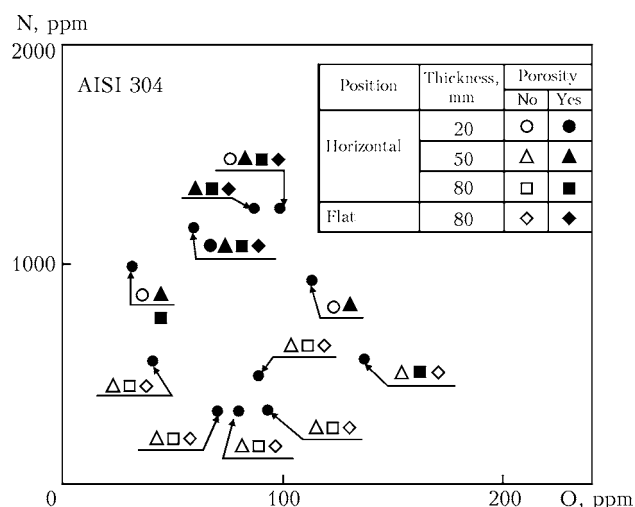


Figure 7. Effect of gas contents on porosity of weld metal

gen levels of below 1200 ppm and oxygen levels of below 100 ppm for the plate thickness of 20 mm, nitrogen levels of below 900 ppm and oxygen levels of below 50 mm and nitrogen level of below 600 ppm and oxygen levels of 50–100 ppm for 50 mm plate thickness, and nitrogen level of below 600 ppm and oxygen level of below 100 ppm for 80 mm plate thickness. No definite difference was observed in porosity occurrence between horizontal position welding (50 mm) and flat position welding in relation to the testing conditions used in the present tests, although the latter is considered to be more advantageous. The difference in nitrogen level between base and weld metal was 20–126 ppm when the nitrogen level of base metal was about 300–600 ppm, and 216–336 ppm when the base metal nitrogen level was about 1200 ppm, indicating that the larger the nitrogen content of the base metal, the larger the reduction. On the other hand, the oxygen level of weld metal decreased to 23–49 ppm, about below half of 43–150 ppm for base metal. As mentioned above, both nitrogen and oxygen levels of weld metal were lower than those of the base metal. This suggests that nitrogen and CO gas result in porosity. The above results revealed that austenitic stainless steel also needs gas contents to be controlled according to plate thickness to prevent porosity.

EB-welded joint properties. In relation to C, Si, P, S Ni, Cr and Mo of elements analyzed, no marked difference was observed in their levels between base metal and weld metal. With regard to N and O, their levels were lower for weld metal than for base metal. Mn level showed a tendency to decrease in the front side. Regarding elements other than Mn, no marked difference was given in their levels inside plate thickness.

The strength of stainless steel is determined by chemical compositions (in particular, by C and N levels) and grain size. On the other hand, for EB-welded metal, whose nitrogen level decreases from that of the base metal, the joint strength ratio is considered to become below 1 with weld metal subjected to fracture in a welded joint tensile test.

The cooling rate of EBW and TIG welding is almost same. But electron beam method is a single-pass welding against multi-pass TIG method. Then EBW is superior to arc welding from the view point of sensitizing of HAZ. Figure 8 shows the results of the sensitizing level measured with the electrochemical potentiokinetics reactivation (EPR) method. It is known that EBW is better than TIG welding.

Application. Since 1983 when application of the EBW to austenitic stainless steel for PWR NPPs was approved as the rules of the Ministry of International Trade and Industry of Japan, on the basis of the above mentioned study results the EBW has been applied to auxiliary tanks, core barrel and reactor core internals made of austenitic stainless steel in PWR NPPs. At present about 700 sets of auxiliary tanks have already been manufactured by the EBW with a large vacuum chamber (approximately 300 m³, measuring 6 × 7 × 8 m).

Carbon steel. EBW conditions. The appropriate welding conditions of one-pass EBW of thick plate are determined in the following sequence. Welding speed and heat input (accelerating voltage \times beam current) are selected depending on the material and plate thickness. Beam current is determined depending on the accelerating voltage of the welding equipment. Proper values of work distance, focal length and oscillation conditions are determined.

In these factors, the proper welding speed becomes lower as the plate thickness increases, and the range arranged in terms of welding speed and heat input per unit thickness tends to narrow as the plate thickness increases. The relation between the work distance and the focal length is the most important parameter. The effect of beam oscillation depends on the beam characteristics of EBW equipment and the plate thickness, but basically it is an important influential factor for forming and maintenance of beam hole during welding. Considering these factors and their effects, investigation into the range of welding conditions of plate thickness of 20 and 100 mm was performed, and the typical welding conditions were selected as shown in Table 2.

Chemical compositions for preventing of weld defects. Because of low cold cracking susceptibility of EBW, weld cracking tests were conducted mainly on hot cracking. Slit type weld cracking test was selected. The hot cracking susceptibility of carbon steel depends on (P + S) content. Accordingly, (P + S) content was varied from 0.01 to 0.04 %. Besides, considering the effect of strength for the cracking susceptibility, materials with different carbon contents were used for this study. The cracking test results are shown in Figure 9. Cracks were found only in the mild steel with (P + S) content of about 0.04 % and carbon content of 0.27 %. These cracks were transverse cracks along the boundary of columnar grains. In carbon steel with over 0.16 % C, quantity of γ -phase in the primary crystals increases because of peritectic reaction. However, the solubility of phosphorus and sulfur in the γ -phase is smaller than that in the δ -phase. Then it is said that hot cracking tend to occur when carbon content becomes higher, and the test results obtained in this study coincided with this tendency. It has been found that cracking can be prevented by controlling (P + S) content under 0.03 % if C content is 0.35 % or less.

Table 2. Typical horizontal EBW conditions for carbon steel

Thickness, mm	Beam current, mA	Welding speed, mm/min	Focal length, mm	Oscillation
20	350	10	280	—
100	650	2.5	460	X: 1 mm Y: 0.5 mm 500 Hz

Note. X — parallel to the welding direction; $U_{acc} = 60$ kV; work distance — 320 mm.

EPR, rel. un.

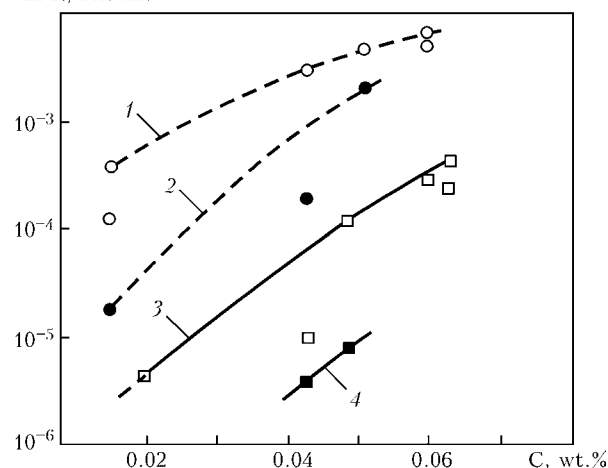


Figure 8. Effect of carbon content and welding method on EPR value for TIG- (1, 3) and EB-welded (2, 4) AISI 304 (1, 2) and AISI 316 (3, 4) 12.0–13.5 mm thick

In horizontal EBW, porosities formed in the molten metal are hard to surface up and tend to be left over in thicker materials. As the cause of porosity formation, gas compositions contained in the steel is considered. Accordingly, occurrence tendency of porosity was studied by using test pieces with various gas compositions (using plates 100 and 150 mm thick). In 150 mm thick plates, accelerating voltage was set at 90 kV. The test results are shown in Figure 10. In 100 mm thick plates no porosity was noticed, and in 150 mm thick plates, porosities were formed in test pieces with nitrogen content of 74 ppm or more. Comparing the gas composition between the base and weld metal, the weld metal became lower in nitrogen content by 0–24 ppm, and in oxygen content by 4–19 ppm. When nitrogen content of the base metal was 40 ppm or less, nitrogen content of the weld metal was nearly same as that of the base metal, and at over 40 ppm it decreased in proportion to the nitrogen content. Oxygen content decreased in the weld metal in proportion to the quantity in the base metal. Gas compositions of killed steel made in Japan is 50 ppm

(P + S), wt.%

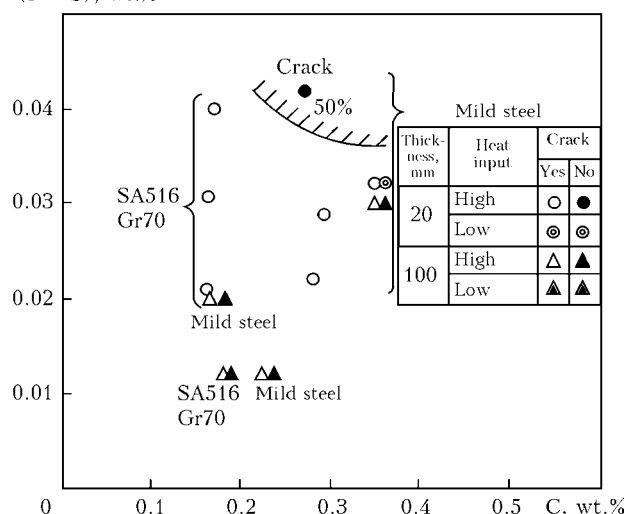


Figure 9. Effect of (P + S) content on hot crack susceptibility of carbon steels with different carbon content

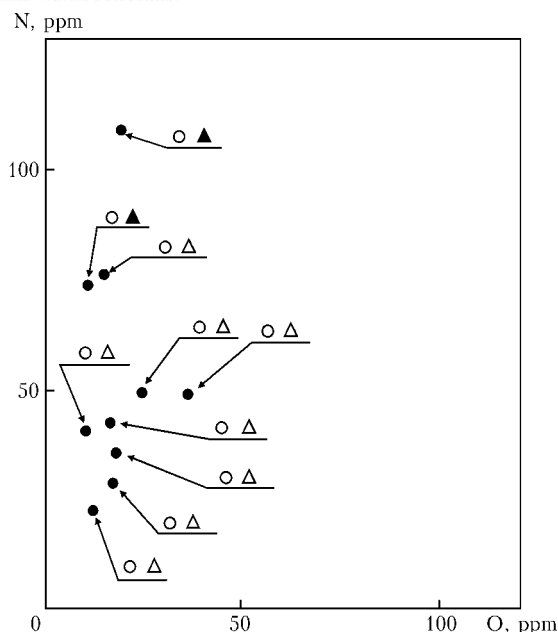


Figure 10. Gas content versus porosity of carbon steel weld metal 100 (○, ●) and 150 (△, ▲) mm thick in horizontal welding with penetration: ●, ▲ — cracks present; ○, △ — no cracks

or less in oxygen and 100 ppm or less in nitrogen. Then it is not particularly necessary to control the gas compositions under 100 mm thickness plate.

Mechanical properties of welded joint. In mechanical properties of EB-welded joint of the carbon steel heavy thickness plate, there is no particular problem in the tensile characteristics and bending properties, but it is important to keep toughness of the welded joint. That is, in EBW of thick plate, higher weld heat input is needed. As a result, grains of weld metal become coarse, and toughness is lowered. To prevent this toughness drop, it is preferable to use the steel containing the special alloys for preventing coarse grains.

Table 3 shows two kinds of steel used. Steel A was conventional steel material, and steel B was titanium oxide treated steel for EBW. The plate thickness was commonly 90 mm. The welding conditions confirmed

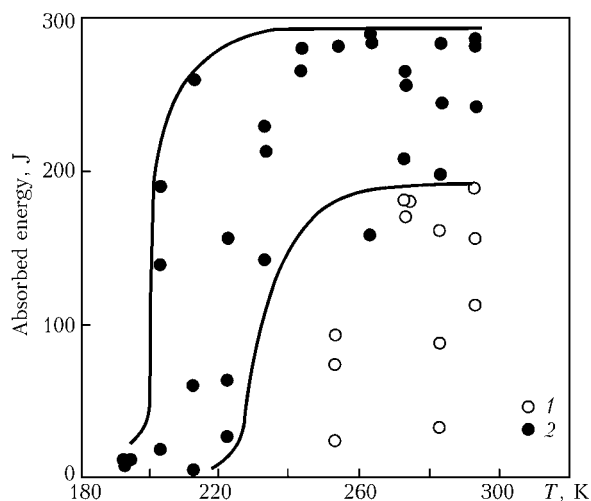


Figure 11. Charpy absorbed energy versus test temperature in 1/4b for conventional (1) and titanium oxide treated (2) steels 90 mm thick (PWHT condition for conventional steel — 868 K for 14,400 s, for treated steel — 888 K for 10,800 s)

Table 3. Chemical compositions and mechanical properties of SA516 Gr70 steel used

Type	Chemical compositions, wt. %					Mechanical properties		
	C	Si	Mn	P	S	σ_y , MPa	σ_t , MPa	δ , %
A	0.16	0.26	1.19	0.005	0.001	422	569	30
B	0.12	0.23	1.15	0.004	0.003	353	490	36

to Table 2, except that beam current was lowered depending on the plate thickness. Charpy impact testing results is shown in Figure 11. Steel B shows an excellent Charpy impact properties at over 243 K, while steel A shows large fluctuation even at 283 K and sufficient toughness was not obtained. Hence, for applying EBW to the carbon steel heavy thickness plates, it is necessary to use properly treated (such as titanium oxide treated) steel materials in order to maintain sufficient toughness.

Application. In PWR NPP equipments made of carbon steel, the biggest one is the accumulator. The accumulator weighs 52 t, and measures 3.5 m in diameter, 5.29 m in height, and 90 mm in wall thickness, and is made of SA516 Gr70 steel. Based on the results mentioned above, the steel material specification was determined and the EBW was applied. Due to the restrictions of the EBW equipment, longitudinal welding was done in vertical down position and circumferential welding was conducted in horizontal position.

Low alloy steel. When a heavy section low alloy steel plate is welded, the weld metal toughness deteriorates. Therefore, in order to apply EBW to heavy section low alloy steel, it is important to increase the weld metal toughness. Bonnin et al. reported that in EBW the target toughness can be secured for plates 100 mm thick or less, but toughness decreases for plates 120 mm thick or more, and so EBW cannot be applied [6]. In general, postweld heat treatment (PWHT) is applied to the pressure vessels. It is known that the weld metal toughness of low alloy steel or high tensile strength steel changes from the as-welded condition due to this PWHT [7, 8]. In addition, the weld metal structure changes in the order of martensite, and lower bainite and also upper bainite with decreasing weld cooling rate. The lower bainite structure has the highest toughness, and the upper bainite structure has the lowest toughness. Therefore, in order to improve toughness, the weld cooling rate should be increased. Then, with low alloy steel plates 20 and 120 mm thick, we have tested the effects of the cooling rate and the PWHT conditions on weld metal toughness, and we have also studied the mechanism of these toughness changes metallographically.

Effect of PWHT conditions on Charpy absorbed energy. Investigated examples of the Charpy absorbed energy of SQV 2B steel (0.21C–1.40Mn–0.56Ni–0.17Cr–0.45Mo) are shown in Figure 12. In this test, EBW was carried out with SQV 2B steel plates 90 mm thick and then PWHT was carried out at 888 K for 14.4 ks. Charpy impact testing were carried out with notches positioned at the weld metal, fusion line, HAZ, and base metal. The Charpy absorbed energies

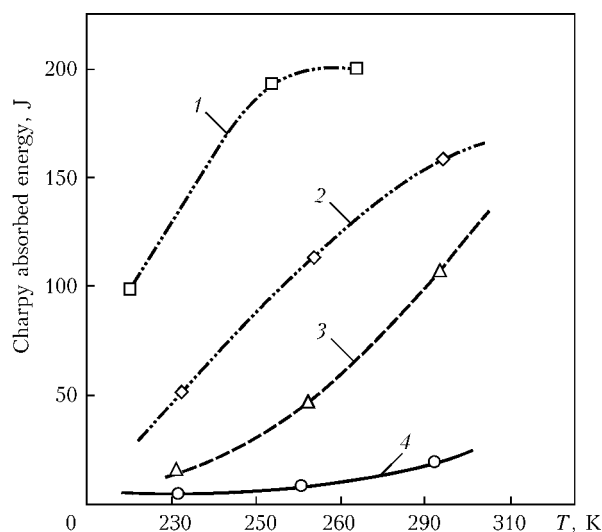


Figure 12. Charpy impact test results for ordinary SQV 2B steel 90 mm thick in 1/2b at PWHT at 888 K for 14.4 ks: 1 – HAZ; 2 – base metal; 3 – fusion line; 4 – weld metal

are in ascending order: HAZ, base metal, fusion line and weld metal. Toughness does not decrease especially in the fusion line, and fusion line is a medium value between those of the weld metal and HAZ. The HAZ has a toughness better than that of the base metal. Consequently, since it was judged important to secure toughness the weld metal for the EB-welded joint of SQV 2B steel, we carried out tests on the weld metal. After manufacturing EB-welded joints and carrying out the specified PWHT, 15 pieces of Charpy impact testing were cut out from the plate middle sections. Then, the Charpy impact testing were carried out at 5 temperature levels to obtain the fracture transition temperature. Figure 13 shows the relations between the fracture transition temperature and the temper parameter in the Charpy impact testing. Figure 14 shows the fracture transition temperature arranged from the viewpoint of the cooling rate in EBW. The cooling rate in EBW has a large effect on the Charpy absorbed energy, and the higher the cooling rate, the better the toughness. That is to say, the fracture transition temperature in the Charpy impact testing after optimum PWHT is about 133 K for plates 20 mm thick (bead width of about 3 mm and cooling time from 1073 to 773 K was about 10 s), but it is 228 K for plates 120 mm thick and suitable welding heat input (bead width of about 4 mm and cooling time from 1073 to 773 K was about 20 s) and it is 253 K for plates 120 mm and higher than suitable heat input (bead width of about 6 mm and cooling time from 1073 to 773 K was about 40 s). These show that with the higher welding heat input and accordingly the lower weld cooling rate, toughness decreases by a great amount. Besides, in as-welded conditions also the fracture transition temperatures are in increasing order of cooling rate, i.e. 173, 313 and 338 K. The toughness in as-welded condition is inferior to the toughness when PWHT is applied, but the effect of the cooling rate is evident. The toughness is improved by PWHT. However, the larger temper parameter means lower toughness, and there is an optimum temper parameter range for obtaining good toughness.

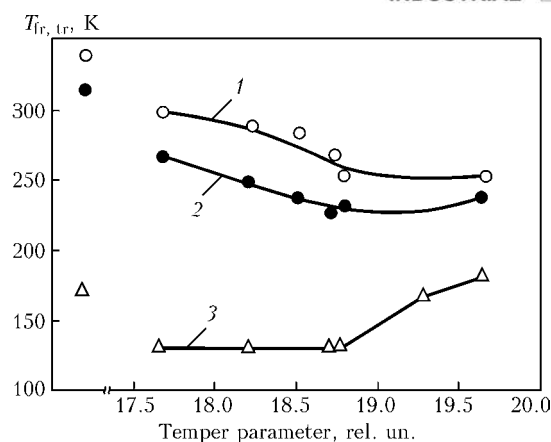


Figure 13. Effect of temper parameter on fracture transition temperature of SQV 2B steel weld metal in 1/2b at notch position on weld metal: 1 – 120 mm thick, high heat input; 2 – 120 mm thick, normal heat input; 3 – 20 mm thick

Under all applied weld cooling rate conditions, the toughness becomes better up to about 19 in temper parameter. However, the toughness tends to decrease above 19. Besides, even at a lower cooling rate for plates 120 mm thick, toughness is improved greatly by PWHT, compared with the as-welded conditions. With these results, it can be clarified that the weld cooling rate and the PWHT conditions have a large effect on the toughness of EB-welded joints on SQV 2B steel. EBW has a limit in penetration, depending on the EB gun capacity. For steel, the maximum penetration is about 100 mm for the 30 kW gun and about 300 mm for the 100 kW gun. Plate thicknesses that can be welded practically will be less than the above values. In addition, when welding with the same EB gun, the welding heat input increases slightly with increasing plate thickness, but it increases sharply on reaching the limit of plate thickness. To reduce the welding heat input, the EB gun capacity and the applied plate thickness should be considered carefully.

Metallographic study of EB-welded metal structures. From the Charpy impact testing results it is clear that the Charpy absorbed energy changes depending on PWHT conditions. Thus, we carried out a metallographic study to investigate these conditions, i.e. as-welded conditions, a temper parameter of 18.8

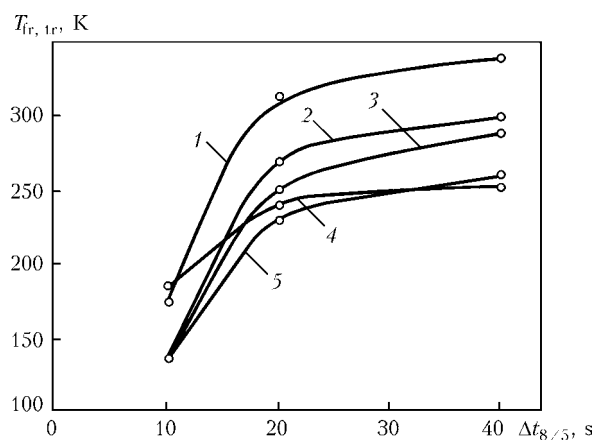


Figure 14. Effect of cooling time $\Delta t_{8/5}$ on fracture transition temperature of SQV 2B steel weld metal in 1/2b at notch position on weld metal in as-welded state (1), at temper parameter 17.7 (2), 18.2 (3), 18.8 (4) and 19.7 (5)

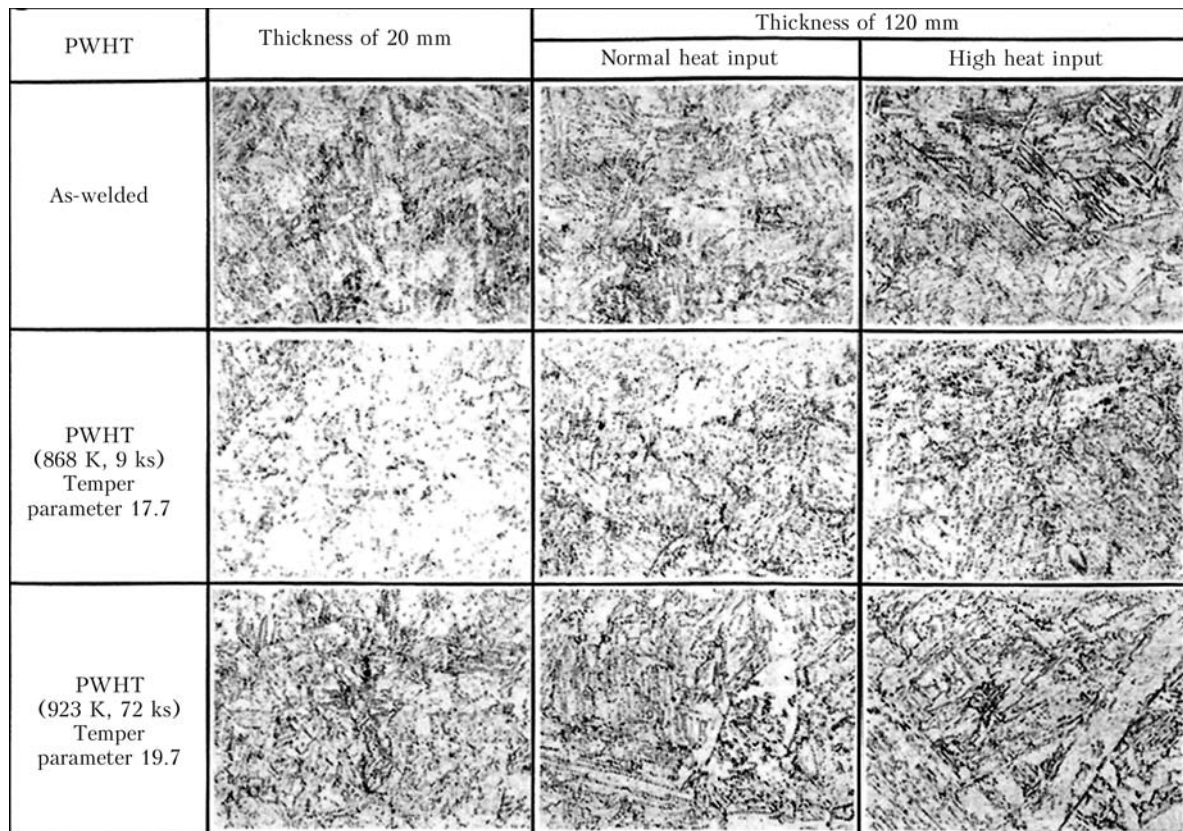


Figure 15. Microstructure of weld metal ($\times 250$)

(the key condition for peak toughness) and that of 19.7 (the key condition for low toughness). Microstructure observation results obtained with an optical microscope and a scanning electron microscope (SEM) are shown in Figures 15 and 16. The as-welded structures are lower bainite for steel plates 20 mm thick and upper bainite for steel plates 120 mm under both suitable welding conditions and higher than suitable welding heat input conditions. The microstructures in the weld metal are uniform and the primary austenite grains become smaller with decreasing heat input. In the optical microphotographs discontinuous black lines appear due to the PWHT and they are seen clearly in the solidification cellular dendrite as the temper parameter becomes larger. These black lines are precipitated carbides from TEM observation re-

sults. With the higher welding heat input, this precipitation starts at the smaller temper parameter. The carbides precipitate along the cellular dendrite boundaries in great quantity. Figure 17 shows TEM observation results with thin foils. In the optical microscope observation there is no difference in microstructure due to the difference in PWHT except carbide precipitation. However, there is a large difference in TEM observation with thin foils. That is to say, the as-welded state is the state of laths have a high dislocation density, but PWHT brings this to a recovery stage. Complete recovery has been attained with a temper parameter of 18.8, and slender subgrains pin-connected by carbides have been uniform. An initial lath tendency remains and the dislocation density is lower than that for the as-welded state, but there

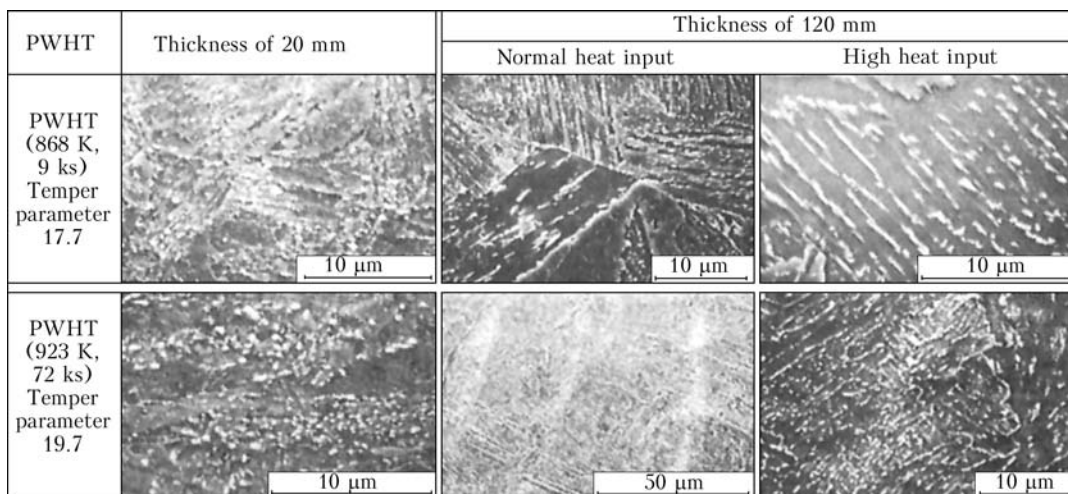


Figure 16. SEM observation of weld metal

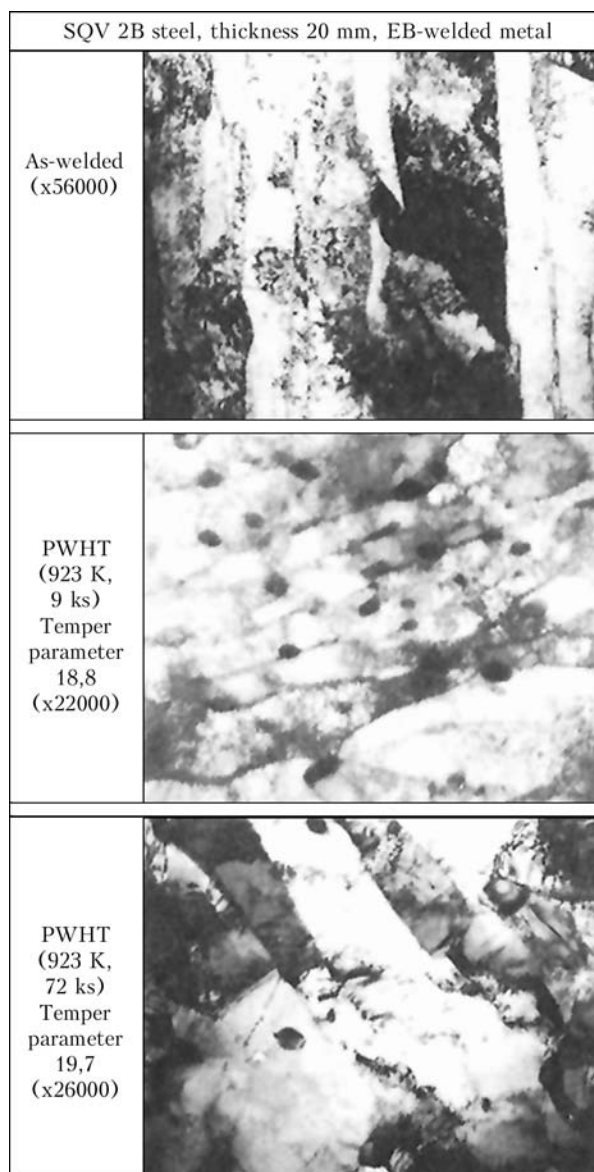


Figure 17. TEM observation by thin foils

still is dislocation in the subgrains. When the temper parameter becomes 19.7, further changes can be seen. In this state not only recovery but also the initial stage of recrystallization appears. The substructure becomes nonuniform because of combination of the recovered subgrains. When changes of the carbide precipitation state due to PWHT are shown with a model, Figure 18 is obtained. In the as-welded state uniformly-distributed fine carbides precipitate near subgrain boundaries due to tempering. As tempering proceeds further, large carbides precipitate in the subgrain boundaries, and so carbides disappear in the neighboring regions. Then, in these regions recrystallization occurs. Thus the causes of toughness change due to PWHT are considered to be as described as follows. In the as-welded state the dislocation density is high, strength is also high, and so toughness is low. However, due to PWHT, the subgrains recover, and so toughness increases. On the other hand, as the temper parameter becomes larger, precipitation of carbides proceeds and also subgrains start recrystallizing

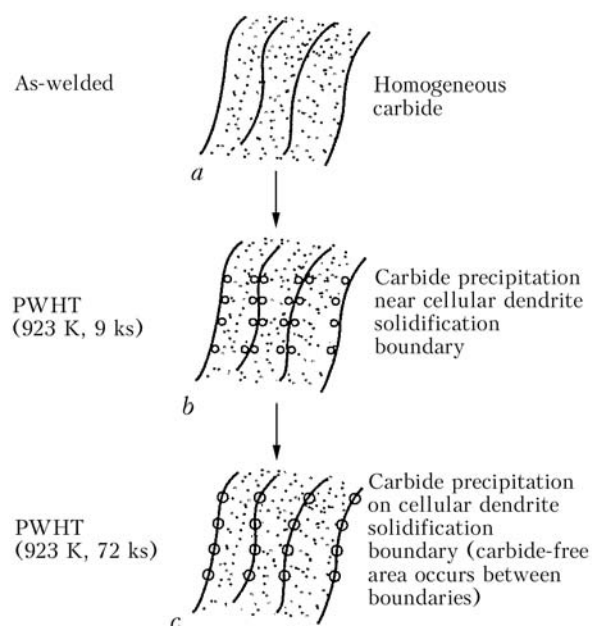


Figure 18. Change of carbide precipitation according to PWHT

to produce regions having no carbide. Therefore, toughness decreases.

Application. Local vacuum EBW was applied to a circumferential joint of a large size pressure vessel model made of a SQV 2B steel plate having an outside diameter of about 2350 mm, a plate thickness of 120 mm and a height of 1000 mm, and it was demonstrated that this method is possible to apply for practical use and that there is no problem in performance of the obtained welded joint [9]. On the basis of the achievements as described above, application of the EBW to the steam generator for PWR NPP was successfully realized.

CONCLUSION

The present research has conducted studies on the appropriateness of the EBW for PWR NPP. A wide range of many sided testing was conducted on the EBW conditions, Chemical compositions for preventing of weld defects and welded joint properties using austenitic stainless steel, carbon steel and low alloy steel.

Based on the results obtained, the authors have applied the EBW successfully for auxiliary tanks, accumulator and steam generators of PWR NPPs.

1. Takano, G. et al. (1983) Practical application of local vacuum electron beam welding technology. *Mitsubishi Technical Review*, 1(20).
2. Matsuda, H., Irie, O. (1969) Experiments on soft-vacuum electron beam welding. *J. JWS*, 10(38).
3. Hull, F.C. (1976) *Welding J.*, 46, 399-408.
4. Brooks, J.A., Thompson, A.W., Williams, J.C. (1984) *Ibid.*, 63, 71-83.
5. Takalo, T., Suutala, N., Moisio, T. (1979) *Metallurgical Transact. A*, 8(10), 1173-1181.
6. Bonnin, P. et al. (1983) Soudage par faisceau d'électrons de l'acier à 533 Gr B classe 1 en forte épaisseur. 3^{eme} C.I.S.F.E.L., 419-426.
7. Kikuta, Y. et al. (1981) Microstructure and toughness of high strength weld metals. *J. JWS*, 1(50), 19-28.
8. Katsumata, M. et al. (1989) Change in mechanical properties with stress relief annealing in pressure vessel steels. *Iron and Steel*, 2(75), 149-156.
9. Takano, G. et al. (1993) Study on electron beam welding with local vacuum for low alloy steel. *Welding in the World*, 1(31), 41-48.



EFFECT OF COMPOSITION OF BASE METAL AND ELECTRODE COVERING ON HYGIENIC PROPERTIES OF WELDING FUMES

K.A. YUSHCHENKO, A.V. BULAT, O.G. LEVCHENKO, O.N. BEZUSHKO, V.I. SAMOJLENKO,
D.I. DOVGAL and N.Yu. KAKHOVSKY

E.O. Paton Electric Welding Institute, NASU, Kiev, Ukraine

The impact of the content of chromium and manganese in high-alloy deposited metal, and of the type of electrode covering on hygienic properties of welding fumes (WF) is considered. It is shown that a change of the chromium content in base metal within 0.30–25 wt.% does not have any essential effect on chemical composition of WF. A change of the content of manganese in base metal from 0.6 to 35 wt.% leads to a 10–15 % increase of its content in WF, and 1.5 times rise in the total level of WF emissions. The minimal level of hexavalent chromium in WF is achieved in welding by using electrodes with coverings of the rutile-silicate type.

Keywords: arc welding, high-alloy steels, covered electrodes, welding fume, hygienic properties, toxicity

Welding of high-alloy chrome-nickel and manganese steels, as well as these steels to low-carbon and low-alloy steels, is performed by using welding electrodes of the E-10Kh25N13G2 and E-10Kh20N9G6S types with basic coverings. Such hygienic properties as the intensity and specific emissions, chemical composition and toxicity of welding fumes (WF) are evaluated primarily in welding steel 12Kh18N10T, which is the most common steel grade. The impact on the above properties by a probable change in chemical composition of base metal has not been studied as yet. When performing erection and repair welding operations (especially inside closed tanks and vessels of high-alloy steels, where local and general ventilation by dilution is difficult or impossible to use), it is necessary to employ electrodes with high hygienic properties. This can be achieved by changing composition of electrode covering.

This study is dedicated to investigation of the effect of the type of base metal and composition of electrode covering on indicators of emissions and chemical composition of WF. As the compounds of hexavalent chromium Cr^{6+} contained in WF are most hazardous in welding of high-alloy steels [1], the focus in this study is on the problem of minimisation of its emissions.

Effect of composition of base metal on level of emissions and chemical composition of WF. Investigations were conducted on samples of plate steel St3sp (killed), 08Kh13, 08Kh17 and 10Kh25N13, measuring $250 \times 120 \times 12$ mm, which were deposited by using 3 mm diameter electrodes ANV-70B (E-10Kh25N13G2 type), as well as on samples of steel St3sp, 110G13-L and 03Kh10G35 of similar sizes, which were deposited by using the same diameter electrodes ANV-66 (E-10Kh20N9G6S type). Experiments (three for each steel grade) were carried out on test pieces made by flat welding at a direct current of

reverse polarity supplied from rectifier VD-500. According to guidelines [2, 3], welding fumes were deposited on filters of fabric FPP-15-1.5 to estimate the level of their emission, and on filters AFA-KhA-18 for chemical analysis of corresponding samples. The experimental results are given in Tables 1 and 2.

As established from the results of a series of experiments with electrodes ANV-70B (E-10Kh25N13G2 type), the weight contents of chromium, manganese and nickel in WF hardly change with an increase of the chromium content in base metal from 0.3 (St3sp) to 24.5 wt.% (steel 10Kh25N13) (see Table 2). At the same time (see Table 1), a 20 % decrease in the arc voltage (power) is accompanied by a decrease in both level of emissions of WF and partial emissions of its components. This can be explained by a relatively high boiling temperature of chromium in the weld pool (Table 3), and by a decreased arc voltage (power).

A different situation took place in a series of experiments with electrodes ANV-66 (E-10Kh20N9G6S). Increase of the manganese content in base metal from 0.6 (steel St3sp) to 34 wt.% (steel 03Kh10G35) (see Table 2) causes increase (by about 10–15 %) of the content of manganese compounds in WF, whereas the content of chromium and nickel compounds remains at the same level. At the same time, decrease in the arc voltage (power) is accompanied by approximately 1.5 times increase in both level of emissions of WF and partial emissions of compounds of the above elements (see Table 1). The said increase in the content of manganese in WF can be caused by a higher pressure of manganese vapours, compared with chromium, and its selective evaporation from the weld pool. This probability is described in study [6] for welding low-carbon and low-alloy steels. It seems that this increase in the level of emissions of WF in the case under consideration can be explained by a growing effect of upward flows of the manganese vapours on electrode metal drops, this leading to dissi-

Table 1. Indicators of the level of WF emissions

Grade (type) of electrode	Grade of 3 mm diameter electrode wire	Base metal	Arc voltage U_a , V	Intensity of WF emissions V_f , g/min	Specific WF emission G_f , g/min
ANV-70B (E-10Kh25N13G2 type)	Sv-07Kh25N13	St3sp	25–26	0.29	11.7
		08Kh13	24–25	0.26	10.1
		08Kh17T	23–24	0.23	9.3
		10Kh25N13	23–24	0.24	9.7
ANV-66 (E-10Kh20N9G6S type)	Sv-08Kh18N10T	St3sp	24–25	0.25	10.0
		110G13-L	23–24	0.27	11.2
		03Kh10G35	22–23	0.38	15.4

Note. Deposition was performed at welding current $I_w = 85\text{--}95$ A.

Table 2. Chemical composition (wt.%) of welding fumes and their hygienic characteristics

Grade (type) of electrode	Base metal	Cr ⁶⁺ (by CrO ₃)	Cr ³⁺ (by Cr ₂ O ₃)	Mn	Ni	F _{sol}	F _{insol}	TLV _f , mg/m ³	NHL, m ³ /min
ANV-70B (E-10Kh25N13G2 type)	St3sp	4.0	3.1	4.2	0.5	5.5	4.3	0.207	1401
	08Kh13	4.6	2.8	4.1	0.5	6.3	4.4	0.183	1421
	08Kh17T	4.4	3.0	4.1	0.5	6.4	3.8	0.190	1211
	10Kh25N13	4.3	3.0	4.6	0.5	6.9	4.3	0.192	1250
ANV-66 (E-10Kh20N9G6S type)	St3sp	3.3	1.6	6.9	0.2	4.5	2.9	0.243	1029
	110G13-L	3.4	1.5	7.7	0.3	4.5	2.5	0.234	1154
	03Kh10G35	3.4	1.5	8.0	0.2	4.5	1.8	0.235	1617

Note. F_{sol} and F_{insol} — soluble (NaF, KF) and insoluble (CaF₂, MgF₂) fluorine compounds [1].

pation of melting products and evaporation of electrode material into the ambient atmosphere.

Comparison of the contents of chromium and manganese in WF of electrodes ANV-70B in welding steel St3sp and other high-chromium steels shows that the level of emissions of the above elements is determined primarily by the composition of electrode material. The same situation takes place in welding with electrodes ANV-66, the only difference being that, in addition to electrode metal at a drop stage, also the weld pool makes a certain contribution (approximately 10–15 %) to the emissions of manganese. The effect by the electrode metal composition on the emissions of chromium and manganese is evident also from comparing compositions of WF of electrodes ANV-70B and ANV-66 formed in welding of steel St3sp: an increased content of chromium and manganese in WF corresponds to an increased content of these elements in electrode material.

The similar situation takes place with the emissions of nickel compounds. According to the data of studies [7, 8], pressure of the manganese vapours grows from zero to 100 kPa at a temperature of 1400–2000 °C. For chromium this occurs at 1800–2600 °C, and for nickel — at 2200–3100 °C. Allowing for the temperature mode characteristic of the weld pool (1550–1650 °C) and electrode metal at a drop stage (1900–

2100 °C), it is apparent that the most probable source of chromium, manganese and nickel in WF is the electrode metal at the drop stage. For this case, Table 4 gives the ratios of the contents of these elements in WF and electrode metal. It should be noted at this point that chromium, manganese and nickel most probably transfer to WF from the metal melt, as the

Table 3. Temperatures of changes in aggregate state of materials [4, 5]

Element or compound	Temperature, K/°C	
	Melting	Boiling
Cr	2123/1850	2773/2500
Cr ₂ O ₃	2673/2400 2553/2280	— 3273/3000
Ni	1726/1453	3183/2910
NiO	2233/1960 2223/1950	— —
Mn Mn ₃ O ₄ MnO	1517/1244 1863/1590 2058/1785 2053/1780	2368/2095 2900/2627 — 3400/3127
CaF ₂	1691/1418	2723/2500
NaF	1270/997	1977/1704
KF	1130/867	1775/1502

**Table 4.** Results of evaluation of content (wt.%) of toxic elements

Base metal	Content in electrode material, wt.%			Content in WF, wt.%		
	Mn	Cr	Ni	Mn	Cr	Ni
St3sp	1.8	25.4	13.5	4.2	4.2	0.5
08Kh13				4.1	4.3	0.5
08Kh17T				4.1	4.3	0.5
10Kh25N13				4.6	4.3	0.5
St3sp	6.5	18.5	9.2	6.9	2.8	0.2
110G13-L				7.7	2.8	0.3
03Kh10G35				8.0	2.8	0.2

temperature of evaporation of corresponding oxides is 500–600 °C higher (see Table 3). As far as fluorine oxides are concerned, according to [7], sodium and potassium fluorides characterised by a lower boiling point than other materials (see Table 3) may form in electrode covering during heating to 600 °C, because of interaction of CaF_2 with solid residue of a liquid glass. In melting of a covering, these fluorides may selectively evaporate from the forming slag and then dissipate in WF.

Results of evaluation of toxicity of WF by the methods described in [9], consisting in calculation of the criteria, i.e. maximum concentration limit of WF, TLV_f , and nominal hygienic requirement to arc exchange, NHL [10] are given in Table 2. As seen from the Table, the main component determining toxicity of WF is hexavalent chromium. In welding steel St3sp, TLV_f has a maximal value, this being indicative of a minimal toxicity of WF in this case, whereas in welding chromium-containing steel this value is not much lower. On this basis, it can be concluded that changes of the chromium content in base metal have an insignificant effect on toxicity of WF.

In the case of increase in the manganese content of base metal, the TLV_f value hardly changes, whereas the NHL value grows 1.5 times, the extent of the

effect by WF on a welder's organism also increasing approximately 1.5 times.

Therefore, it is apparent that the content of chromium compounds in WF does not depend upon that in base metal, whereas the content of manganese, on the contrary, does depend and grows by 10–15 wt.% with increase in its content in deposited metal from 0.6 to 34 wt.%. Increase in the chromium content of base metal leads to lowering of the level of WF emissions approximately by 20 %, the toxicity hardly changing in this case. Increase in the manganese content of base metal leads to about 1.5 times increase in both level of emissions and extent of the effect of WF on the welder's organism.

The content of manganese, chromium and nickel in WF is determined by the contents of these elements in electrode metal, as well as by the pressure of their vapours at temperatures characteristic of the drop stage.

The level of WF emissions depends not only upon the arc voltage (power), but also upon the content of manganese in base metal, which is characterised by the highest pressure of vapours at the weld pool temperature. Also, the vapours of manganese may exert a dissipative effect on melting products and evaporation of electrode material.

Effect of composition of electrode covering on indicators of level of emissions and chemical composition of WF. Three series of experimental electrodes of the E-10Kh25N13G2 type with three types of coverings (Table 5) were made for investigations:

- basic type (series B-1–B-3) with a $\text{CaCO}_3/\text{CaF}_2$ ratio varied from 2.0 to 0.5, and a constant system for deoxidising–alloying of the weld metal (Cr–Mn–Si);
- rutile-basic type (gas- and slag-forming base $\text{TiO}_2\text{--CaCO}_3\text{--CaF}_2$, series R-1–R-4) with constant $\text{CaCO}_3/\text{CaF}_2$ ratio and TiO_2 content, and different systems for deoxidising–alloying of the weld metal (Cr–Mn–Si, Cr–Mn–Al, Cr–Mn–Ti, Cr–Mn);
- rutile-silicate type (gas- and slag-forming base $\text{TiO}_2\text{--SiO}_2\text{--CaF}_2\text{--CaCO}_3$, series RS-1–RS-3) with a

Table 5. Effect of type and composition of covering of welding electrodes of the E-10Kh25N13G2 type on level of WF emissions

Electrode designation	Type of electrode covering	Ratio in electrode covering		Deoxidising–alloying system	V_f , g/min	G_f , g/kg	U_a , V
		$\text{CaCO}_3/\text{CaF}_2$	$\text{TiO}_2/\text{SiO}_2$				
B-1	Basic	2.0	–	Cr–Mn–Si	0.40	16.8	30–32
B-2		1.0			0.35	13.0	28–30
B-3		0.5			0.31	11.5	26–28
R-1	Rutile-basic	1.5	2	Cr–Mn–Si	0.22	8.3	26–28
R-2				Cr–Mn	0.20	7.7	24–26
R-3				Cr–Mn–Ti	0.22	7.9	26–28
R-4				Cr–Mn–Al	0.27	9.8	28–30
RS-1	Rutile-silicate	1.0	4	Cr–Mn–Si	0.20	6.9	24–26
RS-2			3		0.22	8.5	26–28
RS-3			2		0.32	12.9	28–30

Table 6. Chemical composition (wt.%) and hygienic characteristics of WF in welding using electrode of the E-10Kh25N13G2 type with coverings of different types and compositions

Electrode designation	CrO ₃	Cr ₂ O ₃	Mn	Ni	Fi _{sol}	F _{nsol}	TLV _f , mg/m ³	NHL, m ³ /min
B-1	3.86	0.85	4.70	0.64	6.04	6.53	0.209	1914
B-2	4.77	1.02	5.30	0.79	5.90	6.70	0.174	2011
B-3	5.04	1.12	5.05	0.54	5.82	7.01	0.168	1845
R-1	2.80	1.61	3.80	0.43	5.95	2.81	0.279	789
R-2	3.30	2.27	4.30	0.54	6.50	2.16	0.241	830
R-3	4.87	2.87	3.68	0.78	6.79	1.80	0.174	1264
R-4	4.73	3.15	4.51	0.91	5.93	1.75	0.178	1517
RS-1	1.45	6.15	3.92	1.31	4.57	1.67	0.423	473
RS-2	2.80	5.97	3.97	1.97	5.83	1.25	0.256	859
RS-3	6.22	3.86	3.56	1.50	6.56	0.90	0.139	2302

variable TiO₂/SiO₂ ratio (from 4 to 2), constant CaCO₃/CaF₂ ratio and same system for deoxidising-alloying of the weld metal (Cr–Mn–Si).

Coverings were deposited on electrode rods of steel Sv-07Kh25N13, and diameter of all experimental electrodes was 5.2 mm.

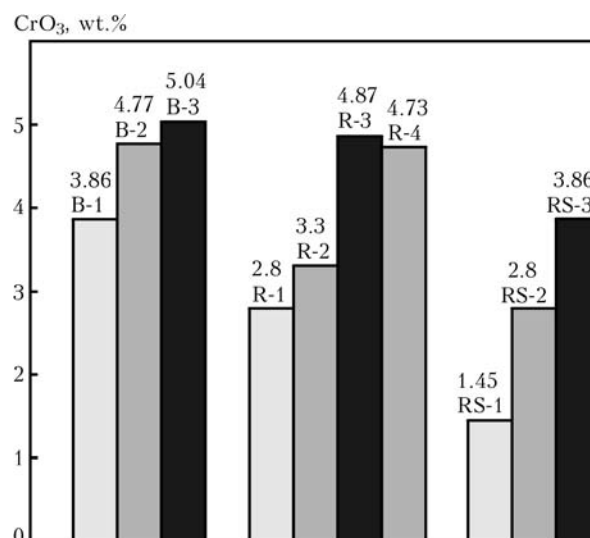
Differences in compositions of coverings of experimental electrodes are shown in Table 5. The level of emissions and chemical composition of WF was evaluated by using the same methods and materials as in the previous series of experiments. Deposition was performed with the electrodes in flat position on plates of steel 12Kh18N10T at a direct current of reverse polarity, $I_w = 90\text{--}100$ A, supplied from welding rectifier VD-500. Results of evaluation of the levels of WF emissions and chemical analysis of corresponding samples are given in Tables 5 and 6.

As established in the course of the experiments with a series of basic electrodes, the maximal level of WF occurs in the case of maximal basicity of a covering (electrodes B-1, CaCO₃/CaF₂ = 2:1), and the minimal level occurs in the case of minimal basicity (electrodes B-3, CaCO₃/CaF₂ = 1:2). This difference, in our opinion, is caused by a higher voltage (power) of the arc of electrodes B-1 and, as a result, by more intensive melting and emission of CO₂ to the arc gap, which dissipates components in the vaporous state into the environment. Electrodes of this series are characterised by the fact that decrease in basicity of a covering and lowering of the level of WF emissions are accompanied by growth of the content of hexavalent chromium in them (see Table 2). This can be explained by growth of the intensity of evaporation of chromium as a result of increase in the time of existence of electrode metal drops [7], as well as by a high pressure of chromium vapours [8] at a temperature of metal at the drop stage.

In electrodes with rutile-basic coverings (see Table 5), the maximal level of WF emissions takes place in the case of using the Cr–Mn–Al, Cr–Mn–Ti and Cr–Mn–Si deoxidising-alloying systems (electrodes

R-4, R-3 and R-1), and the minimal level – the Cr–Mn system (electrodes R-2). This difference can be caused by the fact that the first three variants are characterised by higher values of the arc voltage (power), leading to more intensive melting and evaporation of electrode materials. The minimal content of hexavalent chromium compounds in WF is achieved in deoxidising electrode metal simultaneously with manganese and silicon (electrode R-1).

In a series of rutile-silicate electrodes, decrease in the TiO₂/SiO₂ ratio in a covering leads to increase in the levels of WF emissions (see Table 5), this resulting from increase in the arc voltage (power), as well as intensity of melting and evaporation of electrode materials. Increase in the level of WF emissions is accompanied by increase in the content of hexavalent chromium in them (Figure 1). Supposedly, this is associated with growth of the oxidising ability of a covering and activity of oxygen in slag at the drop stage.

**Figure 1.** Effect of the composition of coverings of E-10Kh25N13G2 type electrodes on content of hexavalent chromium (by CrO₃) in WF

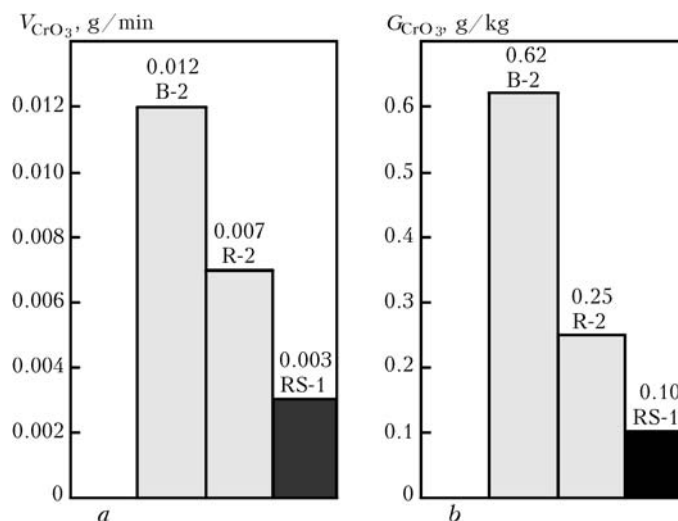


Figure 2. Effect of the type of coverings of experimental electrodes on levels of emissions of hexavalent chromium (by CrO_3) in WF: *a* – intensity of formation of WF, V_{CrO_3} ; *b* – specific emission G_{CrO_3} .

Figure 2 shows the levels of emissions of the most toxic hexavalent chromium compounds in the best variants of experimental electrodes with coverings of the said three systems. It can be seen from the Figure that, other conditions being equal, replacement of basic electrodes by rutile-basic ones, and then by rutile-silicate ones, allows the level of emissions of hexavalent chromium to be decreased 2 and 4 times, respectively. This effect is provided by decrease in the arc voltage (power), smaller amount of carbon dioxide coming to the arc gap because of a low content of marble in a covering, and decrease in the oxidising potential and activity of chromium oxides in slag at the drop stage.

Evaluation of toxicity of WF by the TLV_f and NHL indicators (Table 6) shows that the minimal toxicity of WF is provided by using rutile-silicate electrodes RS-1. At the same time, it may amount to a maximal level when using electrodes RS-3 with the same type of coverings because of a maximal content of hexavalent chromium in WF. Toxicity of WF decreases with growth of the TiO_2/SiO_2 and $CaCO_3/CaF_2$ ratios in electrode coverings, as well as when using manganese or manganese + silicon for deoxidising of electrode metal.

Therefore, the following can be recommended for welding high-alloy steels to minimise the level of emissions of hexavalent chromium in welding fumes and decrease their toxicity:

- to provide the $CaCO_3/CaF_2$ ratio equal to more than one in basic coverings;

- to use manganese or manganese + silicon in rutile-basic electrodes to deoxidise electrode metal;
- to provide the TiO_2/SiO_2 ratio equal to more than three in rutile-silicate electrodes.

The minimal emissions of hexavalent chromium compounds to the work zone air, and minimal level of toxicity of WF can be provided by using electrodes with coverings of the rutile-silicate type.

1. GOST 12.1.007-76: SSBT. Harmful materials. Classification and general safety requirements. Introd. 10.03.76.
2. MU 1927-78: Guidelines. Hygienic evaluation of welding consumables and methods for welding, surfacing and cutting of metals. Moscow: Minzdrav SSSR.
3. MU 4945-88: Guidelines for determination of harmful materials in welding fumes (solid phase and gases). Moscow: Minzdrav SSSR.
4. Krestovnikov, A.N., Vladimirov, L.P., Gulyanitsky, B.S. et al. (1963) *Reference book on calculation of equilibria of metallurgical reactions*. Moscow: GNTIChTsM.
5. Krzhizhanovsky, R.E., Shtern, Z.Yu. (1973) *Thermal-physical properties of nonmetallic materials*. Leningrad: Energiya.
6. Pokhodnya, I.K., Yavdoshchin, I.R., Bulat, A.V. et al. (1983) Search for ways to improve hygienic characteristics of rutile type electrodes. *Gigiena Truda*, Issue 19, 3-9.
7. (1990) *Arc welding metallurgy. Processes in arc and melting of electrodes*. Ed. by I.K. Pokhodnya. Kiev: Naukova Dumka.
8. Pokhodnya, I.K. (1972) *Gases in welds*. Moscow: Mashinostroenie.
9. Yushchenko, K.A., Levchenko, O.G., Bulat, A.V. et al. (2007) Sanitary and hygienic characteristics of covered electrodes for welding high-alloy steels. *The Paton Welding J.*, 12, 35-38.
10. (1978) Criteria for classification of MMA welding electrodes regarding fume. *IIW Doc. II-E-256-78*.



METHOD FOR EVALUATION OF FRACTURE RESISTANCE OF WELDING FLUX GRANULES

V.V. GOLOVKO and I.A. GONCHAROV

E.O. Paton Electric Welding Institute, NASU, Kiev, Ukraine

Method for evaluation of fracture resistance of flux granules and device for its implementation are described. It is shown that the suggested test procedure can be used to generate data on fracture resistance of the flux granules, which is one of the most important welding-operational characteristics of fluxes.

Keywords: *welding flux, granules, method for evaluation, fracture resistance*

One of the peculiarities of granulated fluxes promoting their wide application in fabrication of metal structures and devices by arc welding process is the possibility to reuse this welding consumable. It is well known that refining of a flux takes place in the process of charging it into a hopper of the welding device, welding and removal of residual material from the surface of a welded joint, this resulting in deterioration of welding-operational properties of the flux. Increase of the level of requirements to quality of the weld metal and consistency of formation of the welded joints involved problems related to regeneration of fluxes. As a consequence, customers of fluxes are interested in their ability to retain their initial granule size composition, and manufacturers of this material — in issues associated with increase of fracture resistance of the flux granules in the process of their transportation, storage and application. In this connection, it is a topical problem to develop a suitable method for evaluation of fracture resistance of granules of the welding fluxes.

According to DSTU ISO 14174–2000, fluxes are subdivided into fused and agglomerated ones, depending on the manufacturing technique. Fluxes of these types differ in apparent weight and mechanical strength of their granules. Available methods for evaluation of fracture resistance of flux granules do not give the possibility to obtain comparable results. For example, when testing the fluxes to fracture resistance in a rotating drum together with metal balls [1], the results obtained depend on the degree of filling of the drum with a material. So, it is difficult to compare fluxes if difference in their apparent weights is more than 10 %. Besides, conditions of this test do not simulate the real situations that cause refining of the flux granules, namely in process of their transportation, storage and application.

A method for quantitative evaluation of abrasion resistance of flux granules was proposed by associates of the E.O. Paton Electric Welding Institute [2]. It lies in transportation of a flux dose inside a toroidal vessel for a certain period of time due to the compressed air jet fed to internal cavity, and subsequent

evaluation of changes in granule size composition of the flux. This evaluation method provides an adequate reproducibility of the conditions characteristic of movement of the flux mass when it is removed with a flux aspirator after passage of the welding device. Operating experience with such equipment allows revealing one of its significant disadvantages. It is impossible to maintain pressure of the air jet at a constant level along the whole length of the vessel (about 1 m) because of a rather long path of movement of the flux weight inside this vessel. As a result, if in testing of fluxes with an apparent weight of not more than 1.0 g/cm^3 the granules move inside the torus at an approximately constant speed, then, at their significant apparent weight (over 1.3 g/cm^3), there are zones where the flux speed is considerably lower. In the last case, the test results do not give an idea of the character of changes in granule size composition of the flux in real conditions of the welding process.

Certain changes were introduced in design of the testing device with a purpose of elimination of the above disadvantage (Figure 1). In the improved model, a bulky toroidal vessel was replaced by a small-size metal cup with a double wall. The compressed air, which gets into the internal chamber via several channels, is fed to the gap between the walls under a certain pressure. Uniform movement of the flux mass in the metal cup is provided during the entire test time due to uniform distribution of channels along the circumference of the chamber and their location at an angle to the generatrix.

To carry out investigations, the flux weight is poured into cup 2. Metal grid 5 with a mesh size of $0.2 \times 0.2 \text{ mm}$ is put in the upper part of the device, which is pressed with the help of gaskets 4 by cover 3 to casing 1 after pouring of the flux. An independent compressor, which supplies the compressed air into a cavity located between casing 1 and cup 2, is used to maintain the constant pressure in the device. The compressed air through nozzles 6 is directed in the internal cavity of the cup, where the directed eddy flows of air are formed due to the tangential location with regard to the generating surface of the cup, under the influence of which the flux granules move in the internal cup cavity, while cone 7 positioned in the center of this cavity provides concentration of the whole flux mass in the zone of the highest speeds.

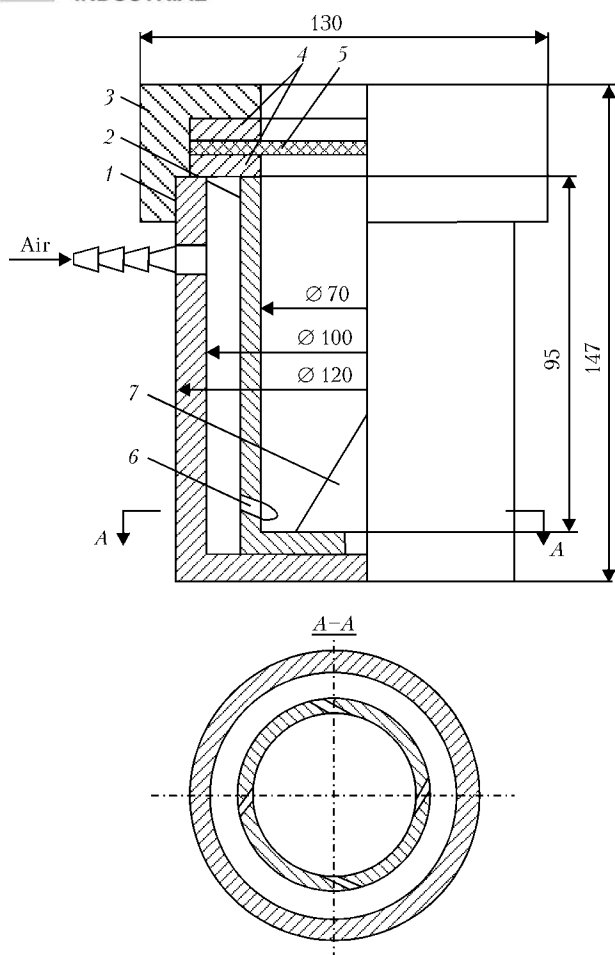


Figure 1. Scheme of device for evaluation of fracture resistance of flux granules (see designations in the text)

In the process of movement of the flux in the device, its granules collide with the cup walls and with each other, thus reproducing the conditions of the flux during its movement along the aspirator. Bearing air flows provide high intensity of this influence as a result of what time of testing is reduced. As a result of abrasion the flux granules partly destroy in the internal cavity of the cup, and a powder-like fraction less than 0.2 mm in size, which is formed in this case, is removed together with the flows of the compressed air via grid 5. The flux weight remaining in the device after completion of the test is weighted, and then fracture resistance (FR) of its granules is determined according to formula

$$FR = 100 - \{[(M_1 - M_2)/M_1] \cdot 100\},$$

where M_1 , M_2 are the masses of the flux weight before and after the tests, respectively, g.

Mass of the flux weight, pressure of the compressed air and test time are setting parameters of this process. As determined as a result of the tests, for the device with design dimensions shown in the scheme, the highest reproducibility of the results at maintaining the high efficiency of analysis can be obtained with the following test parameters: weight mass (30 ± 5) g; compressed air pressure ± 1 kPa; test time (10 ± 1) min.

Results of FR tests of the agglomerated fluxes manufactured with a different mass fraction of a binder and baked at different temperatures are shown in Fi-

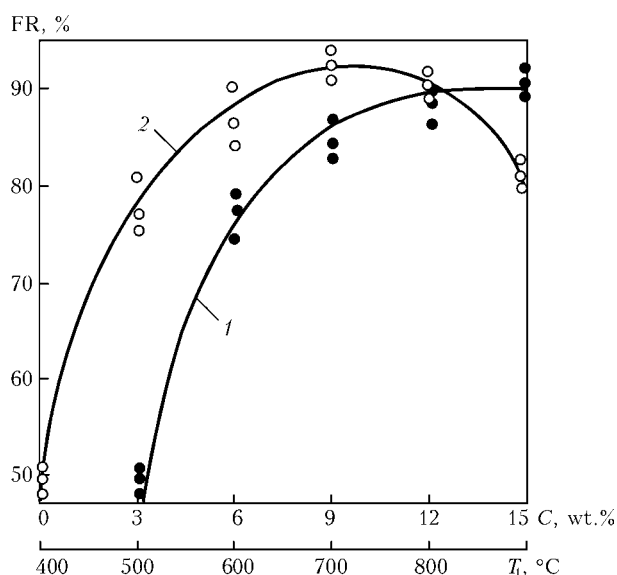


Figure 2. Influence of content C of liquid glass solid residue (1) added to composition of the agglomerated flux, and of temperature of heat treatment T_t (2) on resistance of its granules to fracture

gure 2. It is well known that the manufacturing technology of this flux type is based on irreversibility of the process of dehydration of the liquid-glass binder during heat treatment. The end product of liquid glass dehydration is a silicate frame, whose strength determines fracture resistance of the flux granules. Mass fraction C of solid residue of the liquid glass added to the flux charge, and temperature of heat treatment of the flux, other conditions being equal, are the key factors influencing fracture resistance of flux granules.

Curve 1 in Figure 2 was plotted from the results of the test according to developed method for the aluminate-basic type agglomerated flux, with a different content of solid residue of the liquid glass added to it as a binder for formation of the flux granules. After granulation, the flux was baked at a temperature of 650°C . Mass fraction of the liquid glass was controlled on the basis of content of its solid residue in the flux composition.

Curve 2 plotted for the flux of the same composition, but with 10 wt.% of the liquid glass contained in the solid residue, evidences the influence on FR of the flux granules by conditions of heat treatment, which it was subjected to after granulation.

The data obtained are in agreement with the information available in literature about the influence of the content of a liquid glass binder and temperature of heat treatment of agglomerated fluxes on FR of their granules, and show good consistency of the results of tests of the fluxes according to the described method.

Therefore, the developed method and device for its implementation can be successfully used for evaluation of FR of the flux granules, which is one of the most important factors of welding-operating characteristics of the fluxes.

1. Vegman, E.F., Bocharov, L.N., Matyukhin, B.P. (1971) *Machines and devices for testing of materials*. Moscow: Metallurgiya.
2. (1984) Method of quantitative evaluation of flux granules to wear resistance. *Inform. documents of countries-members of CMEA on problem of welding*, Issue 1(25), 76-77.



EFFECTIVENESS OF APPLICATION OF ALGORITHMS FOR IDENTIFICATION OF WELD REINFORCEMENT IN DIGITAL IMAGES

Ya.P. LAZORENKO, V.O. KOLYADA, E.V. SHAPOVALOV, N.F. LUTSENKO and T.G. SKUBA
E.O. Paton Electric Welding Institute, NASU, Kiev, Ukraine

The paper deals with two algorithms for identification of weld reinforcement in digital images obtained with an optical triangulation sensor — neuronet and probabilistic. Effectiveness of their application is confirmed experimentally.

Keywords: weld, reinforcing bead, edge, images identification, identification algorithm, determination of position, triangulation sensor, automation, digital image, artificial neuron network, neuronet algorithm

There is a range of tasks which necessitate for its solution a tool kit allowing automatically determining position of weld reinforcement. For example, an automatic correction of position of ultrasonic sensors relative to the weld reinforcing bead is necessary in the process of automated ultrasonic testing of longitudinal welds on large-size structures, or automatic centering of abrasive disk relative to the weld is required for realization of robotic grinding of the weld. These and similar tasks can be solved through embedding the weld position feedback into a system of working tool positioning.

At present, contactless optical sensors working on a principle of light section are most often used for automatic determination of coordinates of the weld reinforcement, which is described in detail in [1, 2]. According to the principle of light section, the light plane crosses an object (the weld in this case) to form a light band on its surface. The TV camera located at some triangulation angle to the light plane registers the light band and generates a digital image, in which the light band is represented by pixels with a higher intensity than the main background (Figure 1). Algorithms of identification of line of the light band in digital images are not characterized by any special complexity and are well-known [3].

A more complex task is to analyze and process the detected line of the light band for determination of coordinates of edges of the weld reinforcement. This task is complicated by range of factors: high probability of interferences in the weld zone in a form of irregularities and spatters of molten metal, and instability of the shape and fuzziness of edges of the weld reinforcing bead. Simple algorithms for processing the light band line, which are proposed, for example, by authors of study [1], do not always allow the weld coordinates to be determined with necessary accuracy.

Thus, the algorithms are required, which would allow improving reliability of identification of edges of the weld reinforcing bead. The present study sug-

gests the probabilistic and neuronet algorithms for processing the light band line.

The light band line can be represented in a digital image in a form of discrete function $K(x)$ (Figure 2). The function value determines the number of a line, in which a pixel of the light band line belonging to column x of the image, is situated. The task of determining coordinates of edges of the weld reinforcing bead consists in finding the numbers of columns x_l and x_r corresponding to points of the left and right bead edges (see Figure 2).

With the neuronet algorithm of identification of the reinforcing bead, points of discrete function $K(x)$ of the light band are scanned in sequence. The probability of its correspondence to a bead edge is evaluated for each point. Evaluation of the probability is carried out with the help of the direct-propagation artificial neuron network (ANN) [4]. Informative characteristics of the reinforcing bead edge, which are calculated for each point of the function $K(x)$ on the basis of properties of this point local neighborhood, are supplied to the ANN input. Output values of neuron network $P(x)$, which are estimates of the probability of correspondence of each x point to the bead edge, are formed at the ANN output, based on analysis of input values of the above characteristics. $P(x)$ takes on a value from 0 to 1. The higher the $P(x)$ value, the higher is the possibility that the bead edge is situated at point x . The points corresponding to two

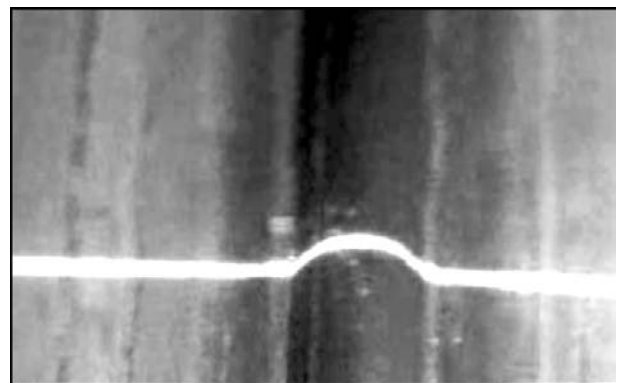


Figure 1. Light band in digital image of the weld

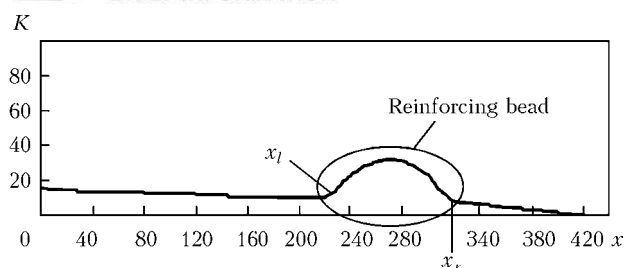


Figure 2. Discrete function $K(x)$ specifying line of the light band local maxima of function $P(x)$ are selected as found bead edges x_l (left edge) and x_r (right edge).

Three informative characteristics of the bead edges are used: module of second derivative $K''(x)$, deviation $\sigma(x)$, and inclination angle $\alpha(x)$. Two sets of characteristics are calculated for each point: $K_l''(x)$, $\sigma_l(x)$, $\alpha_l(x)$ and $K_r''(x)$, $\sigma_r(x)$, $\alpha_r(x)$. The first set includes characteristics of the left edge, and second – those of the right edge. Characteristic $\sigma_l(x)$ is a root-mean-square deviation of points of function $K(x)$ in local neighborhood $[x; x + R]$ of point x from a straight line approximating function $K(x)$ in region $[x - R; x]$, where R is the size of the local neighborhood. Inclination angle $\alpha_l(x)$ is an angle between the line approximating $K(x)$ in region $[x; x + R]$ and line approximating $K(x)$ in region $[x - R; x]$. Characteristics of the right edge, $K_r''(x)$, $\sigma_r(x)$, $\alpha_r(x)$, are calculated in the same way as those of the left edge, but all the intervals are selected to be mirror reflected relative to point x , for which the characteristics are calculated.

ANN consists of two layers of neurons (Figure 3): the first layer – of five neurons, and the second layer – of one neuron. The sigmoid function of activation is used as a non-linear function of neurons. Input signals, i.e. values of the informative characteristics, are fed to the first layer neurons. Output signals of the first layer neurons are fed to inputs of the second layer neuron. Output ANN signal $P(x)$ is formed at output of the second layer neuron.

Teaching of ANN, which consists in adjustment of weight coefficients of the network, is necessary to provide its correct operation. Teaching of ANN is carried out with the help of a special algorithm based on a set of the so-called teaching examples, which are

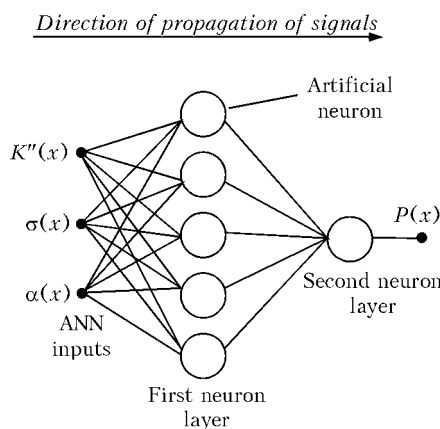


Figure 3. ANN structure

the examples of a correct response of ANN, i.e. the value of output $P(x)$, which is adequate to a specified set of values of inputs $K''(x)$, $\sigma(x)$, $\alpha(x)$. The teaching examples are formed on the basis of characteristics calculated for specific points of the light band lines obtained after processing a set of the weld images. An algorithm of error back-propagation is used as an ANN teaching algorithm [4].

With the probabilistic algorithm of identification of the reinforcing bead, like with the neuronet algorithm, the points of discrete function $K(x)$ of the light band are scanned in series. The probability of correspondence of each point to the edge bead is calculated on the basis of histograms of probability density distribution of informative characteristics of the bead edges. The same set of characteristics ($K''(x)$, $\sigma(x)$, $\alpha(x)$) as in the neuronet algorithm is used as characteristics. Histograms of the probability density distribution are calculated for a set of values of the characteristics determined for a set of images of the light bands at the points corresponding to edges of the weld reinforcing bead.

Estimates of the probability of correspondence of a specified point to the bead edge are calculated in the following way. Firstly, the values of characteristics $K''(x)$, $\sigma(x)$, $\alpha(x)$ are calculated for a given point. Then the corresponding values of the probability density are determined from histograms of each of these characteristics. The required estimate is calculated as an arithmetic mean of these probability densities.

Decision on which points of function $K(x)$ correspond to edges of the reinforcing bead is made on the basis of the estimates calculated from the histograms using the same scheme as that for the neuronet algorithm.

During investigation of the efficiency of algorithms for identification of the weld reinforcing bead, the algorithms were experimentally verified on test images of the welds with the light band. The present investigation was carried out by using a test set consisting of 650 images. Teaching of the neuronet algorithm and calculation of histograms for the probability algorithm were conducted on a set consisting of 110 images. As a result of the investigations, it was determined that coordinates of edges of the weld rein-

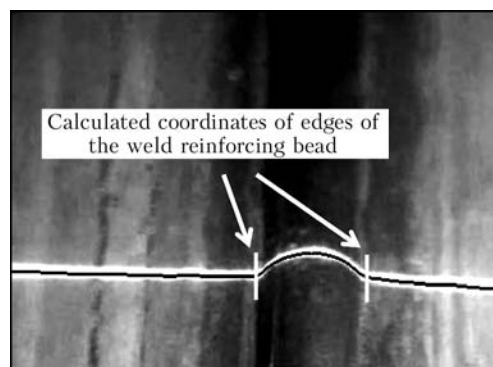


Figure 4. Result of determination of coordinates of the weld reinforcing bead edges using the neuronet algorithm



forcing bead were correctly determined for 98 % of the test images by using the developed algorithms. Relatively big (comparable in size with the bead) metal spatters, which were recognized mistakenly as the weld reinforcing bead, were the main cause of errors in determination of the coordinates. The coordinates of the bead edges were determined properly in the absence of metal spatters in the light band region.

Therefore, it can be concluded on the basis of the experimental investigation results that the developed algorithms are efficient for identification of weld re-

inforcing bead, and that the proposed algorithms can find practical application.

1. Whitney, D.E., Edsall, A.C., Todtenkopf, A.B. et al. (1990) Development and control of an automated robotic weld bead grinding system. *Dynamic Systems Measurement Control*, 2, 166–176.
2. Schilf, M., Horber, H. (2001) Sensoren zum Schweißen mit offenem Lichtbogen. *Schweißen und Schneiden*, 53, 455–458.
3. Haug, K., Pritschow, G. (1998) Robust laser-stripe sensor for automated weld-seam-tracking in the shipbuilding industry. In: *Proc. of 24th Annual Conf. of the Industrial Electronics Society*, 2, 1236–1241.
4. Kalan, R. (2003) *Main concepts of neuron networks*. Moscow: Dom Williams.

PRODUCTION OF TITANIUM INGOTS

International Company «Antares» (see also first page of cover) was founded in 1994 in Kiev, Ukraine. The last 10 years of the activity of the Company have been inseparably connected with advancement of high technologies in the field of electron beam metallurgy, including design and manufacture of specialised equipment, and development of environmentally clean energy-saving technologies.

Our company has developed and now applies the latest technologies for vacuum electron beam remelting of titanium, zirconium, and refractory and special alloys on their base. The Company achieved good results owing to the well organised and creative work of its highly skilled engineers and specialists. They use their deep knowledge and wide experience to address the most difficult problems related to building of equipment and its commercial application.

Based on the scientific potential and capabilities of the Company, we can offer to our customers:

- turnkey development and manufacture of vacuum electron beam furnaces for remelting of different metals and alloys, and machines for electron beam welding, evaporation and other vacuum processes
- production of ingots of titanium, zirconium, refractory metals and special alloys — round ingots with a diameter of 370 to 1100 mm and length of up to 4 m, and flat ingots (slabs) with a width of 1100 to 1350 mm, thickness of 180 to 425 mm and length of up to 4 m;
- wide range of services related to evaluation of chemical composition of metals and alloys, detection of the presence of carbon and sulphur in them, as well as the content of gases, such as nitrogen, oxygen and hydrogen, by using instruments and units produced by the world leading companies.

Technical characteristic of production

Production of the Company is based on two vacuum electron beam furnaces VT01, each with a set power of 2.5 MW and annual productivity of 2.5 t of titanium. At present, the Company is completing manufacture and assembly of a new generation of furnace VT02 with a set power of 3.2 MW. The furnace will use high-voltage inverter-type power units, and will have an annual productivity of up to 3 t of titanium. Design of the furnace will make it possible to produce round ingots and slabs of titanium and its alloys with a weight of up to 14 t and length of up to 5.5 m.

The remelting technology implemented by using the above electron beam furnaces provides:

- cold hearth melting process with a maximal refining effect;
- efficient melting process with counter-directional horizontal feeding and simultaneous melting of consumable billets;
- remelting of non-compacted (titanium sponge, scrap), briquetted or rod-type charge at minimal costs for its preliminary preparation;
- high-productivity process of melting of reactive and refractory metals due to the use of high-voltage glow-discharge electron beam guns characterised by stable operation at pressures of 1.33 – 0.133 Pa;
- simultaneous production of two or more ingots;
- controlled solidification process ensuring the specified structure of ingots.

The electron beam furnaces developed by the Company are superior to their foreign analogues in a number of indicators. Their design peculiarities and the technology employed provide high-quality titanium at low costs. This is achieved, among other factors, owing to the use of the resource-saving technologies (minimal amount of wastes, utilisation of low-grade titanium sponge without preliminary preparatory operations). New scientific and technical solutions underlying development of electron beam furnaces and technologies make it possible to reduce the cost of titanium, compared with the vacuum-arc remelting method.

